이학박사 학위논문

Gravitational N-body Simulations with Special Hardwares and Astrophysical Applications

특수 연산 장치를 이용한 중력 N체 수치계산과 천체물리학적 적용

2013년 8월

서울대학교 대학원

물리·천문학부 천문학 전공

홍 종 석

Gravitational N-body Simulations with Special Hardwares and Astrophysical Applications

by

Jongsuk Hong
(jshong@astro.snu.ac.kr)

A dissertation submitted in partial fulfillment of the requirements for the degree of

Doctor of Philosophy

in

Astronomy

in

Astronomy Program, Department of Physics and Astronomy
Seoul National University

Committee:

Professor	Woong-Tae Kim
Professor	Hyung Mok Lee
Professor	Jong-Hak Woo
Professor	Sungsoo Kim
Professor	Gungwon Kang

ABSTRACT

By using direct N-body simulations with the special hardwares such as GRAPE and GPU, I present the studies of the dynamical evolution of the stellar systems in special cases and the related astrophysical phenomena: rotation of the globular clusters and gravitational wave sources in the galactic nuclei.

In order to understand the effects of the initial rotation on the evolution of the tidally limited clusters with mass spectrum, I have performed N-body simulations of the clusters composed of two mass species with initial rotation and compared the results with those of the Fokker-Planck (FP) simulations. I confirmed that the cluster evolution is accelerated by not only the initial rotation but also the mass spectrum. For the slowly rotating models, the time evolutions of mass, energy and angular momentum show good agreements between N-body and FP simulations. On the other hand, for the rapidly rotating models, there are significant differences between these two approaches at the early stage of the evolutions because of the development of bar instability in N-body simulations. The shape of the cluster for N-body simulations becomes tri-axial or even prolate, which cannot be produced by the two-dimensional FP simulations. The total angular momentum and the total mass of the cluster decrease rapidly while bar-like structure persists. After the rotational energy becomes smaller than the critical value for the bar instability, the shape of the cluster becomes nearly axisymmetric again, and follows the evolutionary track predicted by the FP equation. I have confirmed again that the energy equipartition is not completely achieved when $M_2/M_1(m_2/m_1)^{3/2} > 0.16$. By examining the angular momentum at each mass component, I found that the exchange of angular momentum between different mass components occurs, similar to the energy exchange leading to the equipartition.

The direct detection of gravitational waves (GWs) is now expected for the next-generation GW detectors such as advanced LIGO and Virgo which are planned or under construction. Stellar black hole (BH) binaries are one of the most promising GW sources for GW detection by the ground-based detectors. To investigate the formation and evolution of the BH-BH binaries in the dense stellar systems like

the galactic nuclei, I have carried out the direct N-body simulations. Nuclear star clusters (NCs) located at the center of galaxies are known to have massive black holes (MBHs) and to be bounded by a deep gravitational potential from other galactic building blocks like the bulge. Such environment of NCs provides a good laboratory for the BH-BH binary formation by the gravitational radiation (GR) capture due to the high BH number density and velocity dispersion. I find that the overall formation rates for BH-BH binaries per NC is $\sim 10^{-10}\mathrm{yr}^{-1}$ for the Milky-Way-like galaxies and weakly dependent on the mass of MBH as $\Gamma \propto M_{\mathrm{MBH}}^{3/28}$. Because the merging time of these binaries is negligible compared to the cluster life time, the binary formation rates can be directly converted to the merger rates. The expected detection rates for the next-generation GW detectors can be obtained by the cosmological volume integration of the merger rates and MBH mass function up to the maximum horizon distance. I estimate the detection rate 0.2-2yr^{-1} for advanced LIGO/Virgo. However, several factors such as the dynamical evolution of the cluster, the variance of the number density of stars and the mass range of MBH give uncertainties by a factor of $\sim$100. By implementing the post-Newtonian approximation, I also investigated the motion and the waveform of coalescing BH-BH binaries. For the typical BH-BH binary in Milky-Way-like galaxies, the merging time is a few days and the merging frequency is $\sim$100Hz. The waveforms differ significantly from those of the usual circular binaries since the gravitationally captured binaries are expected to have large eccentricities until the final merge.

Keywords: numerical simulations; stellar dynamics; star clusters; rotation; gravitational wave

Student Number: 2006-20484

Contents

List of Figures

List of Tables

Chapter 1

Introduction

In the universe, there are many kinds of the stellar systems bounded by gravity from planetary systems to the large scale structures, and the study of their formation and evolution is one of the most important issues in astrophysics. Stellar dynamics, the study of the evolution of the stellar systems, can be simply summarized as follows (Binney & Tremaine 2008) what is the fate of the stellar systems whose dynamics is governed mostly by the Newtonian gravity. The notion of relaxation plays the most fundamental role in stellar dynamics. If a star with peculiar velocity comes into a stellar system in equilibrium, the star loses its initial character by the gravitational interactions with field stars and finally melts into the system. The time needed for such process is called the relaxation time $t_{\rm relax}$. For a particle coming into a self gravitating system with the number of particles N, the change of velocity of the particle per crossing is given by

$$\frac{\Delta v^2}{v^2} \approx \frac{8 \ln \Lambda}{N}, \tag{1.1}$$

where Λ is the Coulomb logarithm which is roughly $\approx N$ for self gravitating systems. Thus, for the particle to change the velocity as much as the order of itself, it takes

$$t_{\rm relax} \approx \frac{0.1N}{\ln N} t_{\rm cross}, \tag{1.2}$$

where $t_{\rm cross}$ is the crossing time expressed simply $\sim R/v$. R and v are typical size of the system and speed of particles, respectively. For the stellar systems like galaxies,

the relaxation time is much larger than their lifetimes. Thus, for these *collisionless systems*, the relaxation process is not important. Instead, particles move under the influence of the smoothed gravitational potential from all particles. On the other hand, stellar systems like star clusters and galactic nuclei with shorter relaxation time than their lifetimes are affected by the relaxation. The evolution of these *collisional systems* can be characterized by the relaxation time without N-dependence.

As an aspect of the relaxation, the energy equipartition is also one of the important processes in the stellar dynamics. Two-body encounters tend to make the kinetic energies of stars with different masses similar (Spitzer 1969), and thus, high mass stars become slower than low mass stars and sink to the center (e.g., Giersz & Heggie 1996). This is known to the mass segregation. However, the equipartition does not happen when the number of high mass stars is larger than a certain criterion. In that case, the core is mainly occupied by high mass stars due to the mass segregation, and velocity dispersion of high mass stars is determined by their self gravity rather than the interaction with low mass stars. This, so-called *equipartition instability*, is first suggested by Spitzer (1969).

Due to the two-body interactions, the velocity dispersion of the stellar systems tends to become the Maxwell distribution. Therefore, stars in the high-velocity tail of this distribution can become higher velocity than the escape velocity of the systems so that escape from the system (Ambartsumian 1934; Spitzer 1940). For the simple isolated systems, the evaporation time is $\sim 10^2$ half-mass relaxation times. However, the evaporation for realistic clusters is accelerated by the tidal field (e.g., Lee & Ostriker 1987), mass spectrum (e.g., Lee & Goodman 1995) and the rotation of cluster (e.g., Einsel & Spurzem 1999).

When a stellar system is supported by its own gravity, this self-gravitating system satisfies the virial theorem (i.e., $2K + W = 0$, where K and W are the kinetic and potential energy, respectively). In this case, from the thermodynamical point of view, the stellar system has the negative heat capacity. An isolated self-gravitating stellar system is composed of hot dense core and cold rarefied envelope, and heat is transferred from the core to the envelope. The core becomes hotter (i.e., denser) due to the negative heat capacity. Finally, the core density becomes infinity, which is

called *gravothermal catastrophe* (Lynden-Bell & Wood 1968). It usually takes ~ 10 half-mass relaxation times for an isolated equal-mass system.

Nevertheless, in reality, the core density doesn't go to the infinity. If the core becomes dense enough, binaries can be formed when three stars get together by chance. These binaries are usually *hard* binaries. In stellar systems, binaries can be characterized by the dimensionless hardness x, which is defined as a ratio of orbital kinetic energy in the binary to the average kinetic energy of individual satrs. Classical studies (Heggie 1975; Hut 1983; Hut & Bahcall 1983) show that hard binaries (i.e., $x \gg 1$) become harder while soft binaries (i.e., $x \ll 1$) become softer via binary-single encounters. The hard binaries formed in the dense core play a role as a heat source by converting their internal energy to the kinetic energies of themselves and opponents, and thus the core stops to collapse and expands (Lee 1987). These binaries become harder and faster during encounters and eventually escape from the system when they get faster than the escape velocity of the system. Thus, the system repeats collapsing and expanding through binary formation and escape, which is called *gravothermal oscillation* (Meylan & Heggie 1997).

The stellar dynamics is basically gravitational N-body problems. The best way for N-body problems is to trace the trajectories of all individual stars. However, it is very difficult to deal with realistic stellar systems such as globular clusters ($N \sim 10^6$) or galactic nuclei ($N \sim 10^8$) due to the limited resources for calculation. Instead, Cohn (1979) utilized a statistical approach by solving the Fokker-Planck equation that describes the time evolution of the distribution function (i.e., phase-space density) of stars. The computational cost for solving the Fokker-Planck equation is independent on the number of stars so one can probe the evolution of large N systems. So far, the Fokker-Planck approach has been used in a number of studies for detailed astrophysical applications: gravitational core collapse (Cohn 1980), stellar mass function (Spurzem & Takahashi 1995; Takahashi & Lee 2000), binary formation and merger (Lee 1987; Lee & Goodman 1995), tidal truncation (Takahashi et al. 1997; Takahashi & Portegies Zwart 1998), rotation of star clusters (Einsel & Spurzem 1999; Kim et al. 2002, 2004).

In the mean time, the effort for the direct integration of N-body problems is pioneered by Aarseth (1963). At that time, it was only possible to calculate $\sim$100 particles due to the lack of computational facilities. Since then, in addition to the computing power, many algorithmic improvements for direct N-body simulations also have been d (Aarseth 1999): individual time step (Aarseth 1963), two-body regularization (Kustaanheimo & Stiefel 1965), chain regularization (Mikkola & Aarseth 1990), algorithmic regularization (Mikkola & Merritt 2006), neighbor scheme (Ahmad & Cohen 1973) and Hermite integrator (Makino 1991). As the historical product of all these efforts, NBODY series is one of the widely-used direct N-body codes in the stellar dynamics. NBODY6, the most popular version of NBODY code, now has an advantage of dealing with realistic systems with various astrophysical processes (e.g., binaries or supermassive black holes) which cannot be precisely treated by the Fokker-Planck approaches.

The increase of computational speed for direct integrations is also achieved in hardwares. In direct N-body simulations, the calculation of mutual gravity forces spends most of time with order $O(N^2)$. Thus, it is important to carry out force calculations efficiently in order to reduce computational time. Because the ability for a single central processing unit (CPU) is growing but limited, parallel computing has been utilized to achieve high computational power. The basic concept of parallel computing is SIMD (Single Instruction, Multiple Data), which means the process of same operation for large data set. The first SIMD application was the vector processor by using many ALUs (Arithmetic and Logic Units) controlled by a master CPU. Modern CPUs have also adopted vector processing technology with MMX and SSE (Streaming SIMD Extension) instructions, and most of present supercomputers are composed of numerous CPUs connected by the network. Also there have been efforts for the acceleration of the computational speeds by developing special hardwares. GRAvity PipE (GRAPE, Makino 1991; Makino et al. 1997) is a special-purpose machine for gravitational force calculations. As shown in Fig. 1.1, there are 4 processor chips in GRAPE processor module, including 48 hard-wired pipelines (6 pipelines $\times$ 8 virtual pipelines) per chip, so it is possible to calculate the gravitational force for tens of particles simultaneously. Recently, graphics processing unit (GPU) has

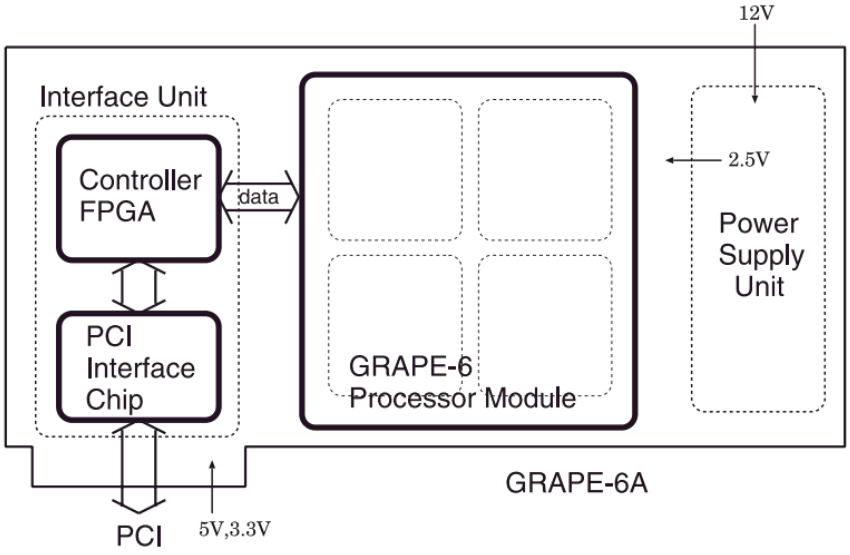

Figure 1.1 Structure of GRAPE-6A (Fukushige et al. 2005).

been massively parallelized in order to process extremely high resolution images, and used for wide fields of computational sciences with programming languages such as CUDA (Compute Unified Device Architecture) or OpenCL. While CPUs have a few processors with high performance, recent high end GPUs have thousands of stream processors, that enable us to perform massive parallel simulations (Fig. 1.2).

NBODY series has adapted to these hardwares. Basically, the force calculation with Hermite scheme by using these hardwares is accomplished in the following sequences (Aarseth 2010):

1. Set the next time for integration and determine active particles.
2. Predict all particles' positions and velocities.
3. Send data of all particles (mass, position and velocity) from *host* to *device*.
4. Estimate forces and first derivatives of active particles on *device* and send the results to *host*.
5. Obtain higher order derivatives of force.
6. Correct the positions and velocities of active particles.
7. Repeat steps from 1.

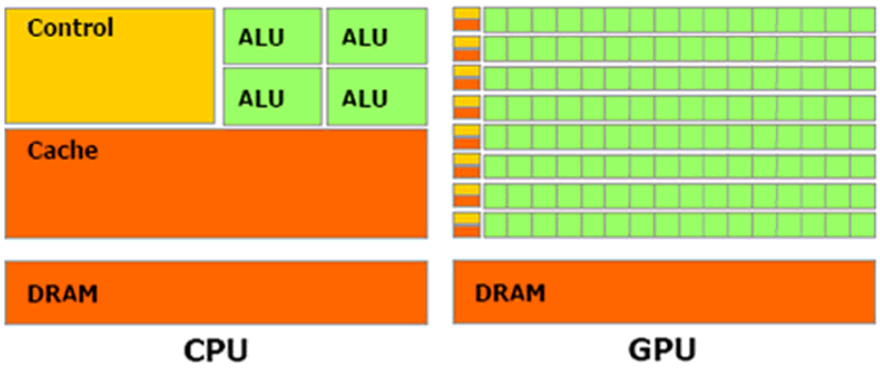

Figure 1.2 Schematic diagrams of CPU and GPU.

The *host* and *device* are connected by the network cable for CPU clusters or by PCI (Peripheral Component Interconnect) for GRAPEs and GPUs. The maximum number of parallel force calculations depends on the device characteristics: the number of processors (CPU clusters), the number of pipelines (fixed to 48, GRAPE) and the number of threads (GPU). There are several versions of NBODY codes with different hardware configurations. NBODY6++ has been developed by Spurzem (1999) for parallel supercomputers by using MPI (Message Passing Interface). NBODY4 (Aarseth 2010) and NBODY6-GPU (Nitadori & Aarseth 2012) also have been developed for GRAPE machines and for GPUs. The parallelization of N-body force calculations is achieved in two ways: i-parallelism (i.e., force calculation for the multiple i-particles which feel the gravitational force) and j-parallelism (i.e., force calculation for the multiple j-particles which serve the gravitational field). In NBODY4 code, all force calculations are performed up to 48 particles on the GRAPE board with i-parallelism via multiple pipelines without the neighbor scheme. On the other hand, in NBODY6, the force calculations separate the *regular* forces from distant particles whose gravitational potential changes slowly and the *irregular* forces from neighboring particles. In NBODY6-GPU, the regular forces are calculated on GPU devices by using multiple threads with both i-parallelism and j-pararellelism while the irregular forces are calculated on CPU with j-parallelism by using multiple cores in CPUs with AVX (Advanced Vector Extensions) or SSE (Nitadori & Aarseth 2012). Nowadays, a hy-

brid NBODY code for parallel supercomputers with many GPUs is being developed by Rainer Spurzem.

In reality, stellar systems do not evolve as simply as the idealized models. The main goal of this thesis is to investigate the dynamical evolution of the stellar systems in specific situations by using direct N-body simulations with high performance hardwares (e.g., GRAPE and GPU). Here, I consider two different astronomical applications as follows;

Dynamical evolution of rotating star clusters with two-component models

The effects of the initial rotation on the dynamical evolution of star clusters received substantial attention because the rotation is a natural consequence during the formation process. The direct measurement of the rotation is difficult and is done only for a couple of massive star clusters (e.g., ω Centauri and 47 Tucanae, Meylan & Mayor 1986) since it requires long integration with large aperture telescope. Rather indirect evidence for the rotation comes from the shape of globular clusters. Although most globular clusters show high degree of circular symmetry, one can infer that many clusters still have some degrees of rotation from ellipticity measured for a number of star clusters (e.g., White & Shawl 1987).

Since Goodman (1983) studied rotating star clusters using Fokker-Planck equations, many authors have revealed the dynamical evolution of rotating star clusters focusing on gravitational collapse (Einsel & Spurzem 1999), binary heating (Kim et al. 2002) and the effect of mass spectrum (Kim et al. 2004). More recently, Kim et al. (2008) compared two different approaches, Fokker-Planck and N-body simulations, and confirmed the validity of Fokker-Planck methods. However, they only consider equal mass cases and relatively slow initial rotations which ensure axisymmetric shape of clusters. Thus, I perform N-body simulations with mass spectrum and wider range of the initial rotation in order to know the effect of the rotation and mass spectrum and to confirm the validity of Fokker-Planck approaches.

Black hole binaries in galactic nuclei and gravitational wave sources

It is well-known that most of galaxies host massive black holes at the center. From the recent observational studies (Carollo et al. 1997; Böker et al. 2002; Côté et al. 2006), it is also revealed that many galaxies contain compact and massive star clusters called nuclear star clusters in their nuclei (e.g., $\bar{\rho} \sim 10^6 M_{\odot}\mathrm{pc}^{-3}$ for Milky Way; Schödel et al. 2007). Because nuclear star clusters have shorter relaxation time scales than a Hubble time, they are expected to be dynamically relaxed. A number of studies (Baumgardt et al. 2004b; Hopman & Alexander 2006; O'Leary et al. 2009; Preto & Amaro-Seoane 2010) suggested that there is a strong mass segregation among stellar components with different individual masses.

These nuclear star clusters can provide good environments for the formation of compact binaries composed of compact stars such as neutron stars or black holes: high stellar density, velocity dispersion and number fraction of compact stars. Such binaries could become important sources of gravitational waves. So far, a detailed study for gravitational wave sources in galactic nuclei has been done by O'Leary et al. (2009) by using a Fokker-Planck simulations. Here, for the second part of thesis, N-body simulations for nuclear star clusters are performed in order to investigate the dynamical evolution of nuclear star clusters and the aspects of gravitational wave sources in galactic nuclei.

This thesis consists of four chapters. In Chapter 2, the dynamical evolution of rotating star clusters with 2-component masses is presented. I also discuss the effect of the rotation and the mass spectrum on the dynamical evolution and compare the results of different approaches. In Chapter 3, I describe the models for nuclear star clusters located at the center of galaxies and estimate the merger rates for black hole binaries and detection rates for the next-generation gravitational wave detectors. The statistics of black hole binaries and sample waveforms are also presented in this chapter. Finally, I summarize the thesis in Chapter 4.

Chapter 2

Dynamical Evolution of Rotating Star Clusters with Two-component Models [1]

2.1 Introduction

The effects of initial rotation on the dynamical evolution of star clusters received substantial attention because the rotation is a natural consequence during the formation process. The current population of star clusters may not show significant amount of rotation, but it does not mean that the initial conditions inhibit the presence of rotation. The direct measurement of the rotation is difficult since it requires long integration with large aperture telescope. Rather indirect evidence for the rotation comes from the shape of globular clusters. Although most globular clusters show high degree of circular symmetry, the ellipticity has been measured for large number of star clusters (e.g., White & Shawl 1987; Chen & Chen 2010). If the ellipticity is due to the rotational flattening, many clusters still have some degrees of rotation. Even though the amount of rotation in current population of globular clusters is rather small, initial clusters could have been rotating much more rapidly since the rotation phases out as the clusters evolve dynamically.

[1] Hong, J., Kim, E., Lee, H. M., & Spurzem, R. 2013, MNRAS, 430, 2960

The effects of rotation on the dynamical evolution have been studied by a number of authors. Goodman (1983) has extended the Fokker-Planck (FP) equation for rotating systems, but his study was limited to slowly rotating systems by imposing the spherical symmetry for the shape of the clusters. The thermodynamical analyses have been pioneered by Hachisu (1979, 1982) and found that there exists an instability similar to gravothermal catastrophe and they named this phenomenon as 'gravo-gyro catastrophe'. Theses earlier studies provided the basis of the possible acceleration of dynamical evolution due to the initial rotation.

More careful studies for the rotating systems have been carried out by Kim et al. (2002, 2004, 2008) using 2-Dimensional FP code developed by Einsel & Spurzem (1999). These papers investigated both isolated and tidally limited clusters, and single and multi-component clusters. The general result emerged from these studies is that the rotating clusters undergo faster evolution than non-rotating ones for single component models. The acceleration is also expected in multi-mass models as well, but the degree of acceleration could be significantly reduced since the energy exchange between different mass components is another accelerating process and these two processes compete each other.

The suitability of the FP approach to the study of dynamical evolution of star clusters has been a matter of debate because the absence of the accurate knowledge on the third integral for rotating systems prohibits us to include all the possible integrals in constructing the FP equation. Comparison with N-body calculation should provide a clue to the validity of the current version of the FP approach (e.g., Giersz & Heggie 1994a,b; Giersz& Spurzem 1994). Such a comparison for rotating systems was done by Ernst et al. (2007) and Kim et al. (2008) for single component models and showed that the FP results are generally consistent with the N-body calculations.

We extend the comparison to the two-component models as an interim step to the full multi-mass models. Two-component models have the ingredients for the multi-mass models, but have smaller model parameters. The important difference between single and multi-mass models is the existence of energy exchange among different mass components. In rotating models, there is also a possibility of exchange of

the specific angular momentum through the dynamical process. It is much easier to investigate such processes in N-body. Another motivation for carrying out N-body simulations and comparing with FP results is to address the validity of the axisymmetric assumption which is inevitable for the FP approaches. If the cluster rotates rather rapidly, the bar-like structure can form even with the initial assumption of the axisymmetric shape. The evolution of the elongated cluster could be different from the perfectly axisymmetric one.

This paper is organized as follows: In §2.2, we describe the models and their parameters in detail. The effect of the initial rotation on the cluster shape will be presented in §2.3. In §2.4, we will compare N-body and FP results in various angles. We will discuss the effects of mass spectra on the dynamical evolution of star clusters in §2.5.

2.2 Method and models

Most of FP results for rotating stellar system with initial mass spectrum are based on the 2D FP solver, mFOPAX (Kim et al. 2004) which is the revised version of FOPAX (Einsel & Spurzem 1999; Kim et al. 2002) suitable for the rotating stellar system with initial mass spectrum. For the complete description of mFOPAX readers are referred §§2 and 3 of Kim et al. (2004).

The NBODY code which we used for this study is one of series of direct N-body programs developed by S. Aarseth since 1960s. Each version of the NBODY codes has been added some epochal schemes such as the Ahmad-Cohen neighbor scheme, the Kustaaheimo-Stiefel or chain regularization scheme (Aarseth 1999). More recently, the NBODY4 and the NBODY6 codes can perform more precise calculations thanks to the 4th-order Hermite integrator (Aarseth 1999). Specially, the NBODY4 code is designed for running on the GRAPE, which is a special-purpose machine for only direct N-body simulations by calculating gravity or coulomb interaction with high parallelization. We used the GRAPE6-BLX64 boards for the N-body calculations reported in this paper.

To prepare the initial models for the present N-body runs we have assigned the

positions and the velocities of the stars from the predefined density, potential and distribution function of initial models. These initial models also used in FP runs are obtained following Lupton & Gunn (1987) and also applied in previous studies (Einsel & Spurzem 1999; Kim et al. 2002, 2004, 2008). Globular clusters or open clusters which are typical stellar systems considered in the present study are tidally limited by their host galaxy. To investigate the time evolution of rotating stellar system under the influence of the tidal effect of the host galaxy and to compare the dynamical evolution of rotational stellar system using two different numerical methods (FP and N-body), we assume that the stellar systems are orbiting around the center of the Galaxy with circular orbit, which is already applied in previous FP runs (Kim et al. 2002, 2004). In order to directly compare N-body results with FP methods, we remove the stars whose total energy exceeding the tidal energy due to the host galaxy instantaneously (i.e., energy cut-off, Takahashi et al. 1997; Baumgardt 2001; Kim 2003; Ernst et al. 2007; Kim et al. 2008). According to the N-body computation, it takes at least a crossing time to escape from the clusters for stars with total energy larger than the tidal energy. Therefore, instantaneous removal of stars with energy greater than tidal energy is somewhat unrealistic. The problem becomes more serious for small-N systems since the fraction of stars to be unbounded at a given time is higher than large-N systems (Takahashi & Portegies Zwart 1998; Fukushige & Heggie 2000). However, since the main goal of the present study is to investigate the difference between N-body and FP methods for rotating stellar systems, we need to apply the same criteria with the FP approach. The tidal boundary (or tidal energy) is adjusted during evolution as described in the previous studies (Kim et al. 2002, 2004, 2008).

Table 2.1 shows the initial parameters used for the N-body simulations. For comparison, we also performed FP simulations of M2A models. There are several parameters that determine the cluster evolutions such as the concentration parameter W_0, the initial rotation ω_0 (Einsel & Spurzem 1999; Kim et al. 2002; Ernst et al. 2007), the mass spectrum (Kim et al. 2004; Khalisi et al. 2007) and tidal boundary (Baumgardt 2001; Kim 2003; Ernst et al. 2007). We fixed $W_0 = 6$, but varied ω_0 and mass spectrum to investigate the effect of the initial rotation and the mass spectrum

Table 2.1 Initial parameters for all models.

Model	W_0	ω_0	$\frac{r_{\rm tid}}{r_{\rm c}}$	$\frac{T_{\rm rot}}{\lvert W\rvert}$	N*runs	$\frac{m_2}{m_1}$	$\frac{M_1}{M_2}$	N_2	S	Λ
(1)	(2)	(3)	(4)	(5)	(6)	(7)	(8)	(9)	(10)	(11)
		0.0	18.0	0.000	20,000*3					
		0.3	14.5	0.035	20,000*3					
M2A†	6	0.6	9.9	0.101	20,000*3	2	5	1818	0.566	1.056
		0.9	7.1	0.156	20,000*3					
		1.2	5.4	0.196	20,000*3					
		1.5	4.4	0.222	20,000*3					
		0.0	18.0	0.000	20,000*1					
M2B	6	0.6	9.9	0.101	20,000*1	5	5	769	2.236	9.518
		1.2	5.4	0.196	20,000*1					
		0.0	18.0	0.000	20,000*1					
M2C	6	0.6	9.9	0.101	20,000*1	10	5	392	6.325	50.24
		1.2	5.4	0.196	20,000*1					
		0.0	18.0	0.000	20,000*1					
M2D	6	0.6	9.9	0.101	20,000*1	20	5	198	17.89	256.2
		1.2	5.4	0.196	20,000*1					
		0.0	18.0	0.000	20,000*1					
M2Ae	6	0.6	9.9	0.101	20,000*1	2	20	488	0.141	0.264
		1.2	5.4	0.196	20,000*1					

†Fokker-Planck simulations are performed for comparison.

Note. - (1): Model indexes indicating the mass spectrum. (2): Concentration parameter. (3): Dimensionless initial rotation parameter. (4): Tidal radius normalized by core radius. (5): Ratio of rotational kinetic energy to the potential energy. (6): Number of particles and number of simulations with different initial random seeds. (7): Individual mass ratio. (8): Total mass ratio. (9): Number of high mass stars. (10)-(11): Equipartition instability parameters from Spitzer (1969) and Watters et al. (2000)

on the cluster evolution. The initial rotation ω_0 are varied from 0.0 to 1.5. For the mass spectrum, we varied the individual mass ratio m_2/m_1 from 2 to 20 while the total mass ratio M_1/M_2 is fixed to 5 or 20. One of the most important processes of the stellar system with multiple mass components is the energy equipartition. The energy equipartition is a tendency for different mass components to have similar kinetic energies. However, in some cases, the equipartition is not completely achieved, which is called as the equipartition instability (Spitzer 1969). To determine whether the equipartition happens to be achieved or not in two-component mass systems, Spitzer (1969) derived an analytic equipartition stability parameter,

$$S = \frac{M_2}{M_1}\left(\frac{m_2}{m_1}\right)^{3/2}. \tag{2.1}$$

He suggested that the energy equipartition between low and high mass stars takes place when $S < S_{\rm crit} = 0.16$. After Spitzer's study, many authors have studied the energy equipartition process of two-component systems by theoretical approaches (e.g., Lightman & Fall 1978) and by several numerical methods such as Monte-Carlo approaches to solve the FP equation (Spitzer & Hart 1971), the direct integration of FP equation (Kim et al. 1998) and N-body simulations (Portegies Zwart & McMillan 2000). Watters et al. (2000) performed Monte-Carlo simulations with various two-component mass spectra and introduced an empirical equipartition stability parameter

$$\Lambda = \frac{M_2}{M_1}\left(\frac{m_2}{m_1}\right)^{2.4} \tag{2.2}$$

and found that the critical value for energy equipartition is $\Lambda_{\rm crit} = 0.32$. Most of our models have $S > S_{\rm crit}$ and $\Lambda > \Lambda_{\rm crit}$. The ratio of the rotational kinetic energy to the potential energy is known to be a measure of the 'temperature' of the rotating system with higher value being called cold system. If this parameter is greater than 0.14, the system is known to become dynamically unstable against the formation of the bar-like structure (Ostriker & Peebles 1973). Thus, models with ω_0 greater than 0.9 are expected to evolve to elongated shape. We designate these models as rapidly rotating models and the other models with $\omega_0 \leq 0.6$ as slowly rotating models in this study.

2.3 Slowly and rapidly rotating clusters

To investigate the effect of the initial rotation on the evolution of clusters, we focus on M2A models which have various amounts of the initial rotation. In Fig. 2.1, we show the time evolution of the ratio of the rotational kinetic energy to the potential energy, $T_{\rm rot}/|W|$. The dashed and solid lines represent FP and N-body results, respectively. The initial half-mass relaxation time is measured as follows suggested by Spitzer & Hart (1971),

$$\tau_{\rm rh,0} = 0.138 \frac{N^{1/2} r_{\rm h,0}^{3/2}}{G^{1/2} \overline{m}^{1/2} \ln \Lambda}, \tag{2.3}$$

where $N, r_{\rm h,0}, G, \overline{m}$ and $\ln \Lambda$ are total number of stars, initial half-mass radius, gravitational constant, mean mass of stars and Coulomb logarithm, respectively. It is well known that a system with rigid-body rotation suffers a secular instability when $T_{\rm rot}/|W|$ is larger than 0.14 (Ostriker & Peebles 1973). Later, from numerical simulations, Sellwood (1981) confirmed that the criterion is valid for more realistic rotation curves. Our models with initial value of $T_{\rm rot}/|W| < 0.14$ are shown in the upper panel and those with $T_{\rm rot}/|W| > 0.14$ are shown in the lower panel. The results of N-body and FP show similar behaviors for the models with initial $T_{\rm rot}/|W| < 0.14$. However, for the models with initial $T_{\rm rot}/|W| > 0.14$, the initial evolution depends on different numerical approaches. The N-body simulation represents more rapid decrease of $T_{\rm rot}/|W|$ with time than the FP simulation in the early phase. For the rapidly rotating models one can observe the construction of bar-like structure and the total rotational energy decreases very quickly. Therefore, the FP approach seems to be not appropriate in describing the evolution of rotating models with initial value of $T_{\rm rot}/|W| > 0.14$.

In order to investigate the evolution of the cluster shape, we calculate axis ratios of clusters by using the method suggested by Dubinski & Carlberg (1991). They defined a tensor,

$$M_{ij} = \Sigma \frac{x_j x_j}{q^2} \tag{2.4}$$

with an ellipsoidal radius,

$$q = \left(x^2 + \frac{y^2}{(b/a)^2} + \frac{z^2}{(c/a)^2} \right)^{1/2}, \tag{2.5}$$

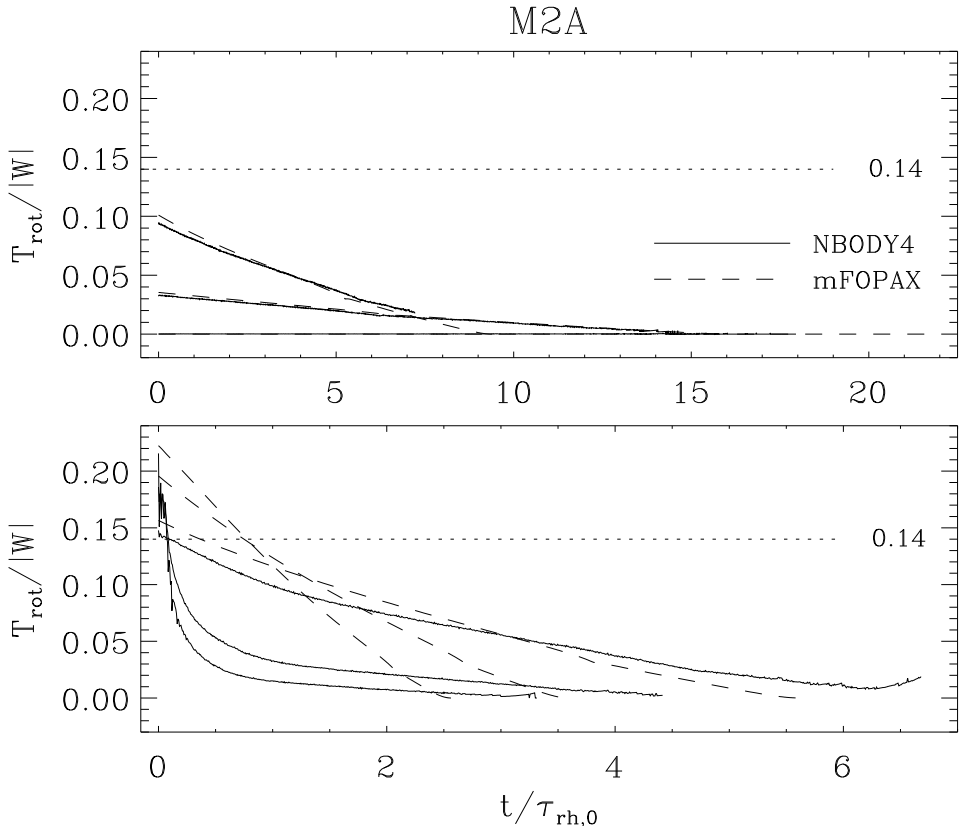

Figure 2.1 The ratio of rotational kinetic energy to potential energy. Solid and dashed lines represent N-body and FP results, respectively. Upper panel shows the ratios for slowly rotating models and lower for those of the rapidly rotating models. The dotted lines denote a criterion of bar instability (Ostriker & Peebles 1973). For rapidly rotating models the N-body and FP results show the significant difference due to the bar instability.

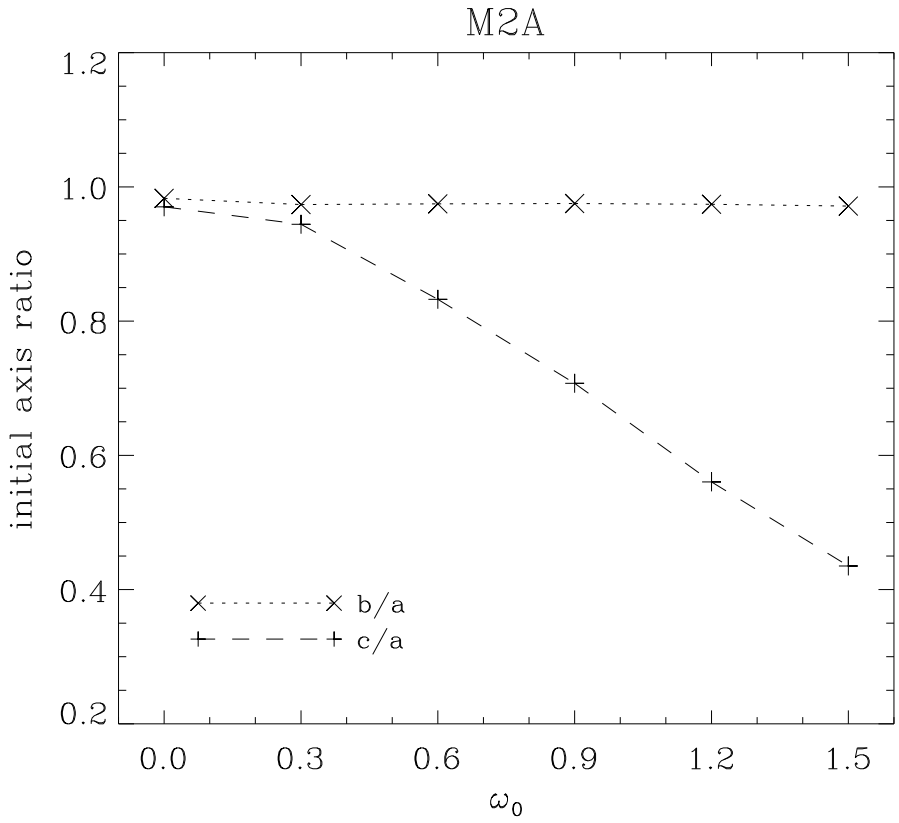

Figure 2.2 Initial axis ratio of clusters with different initial rotations. Cross and plus symbols show intermediate (b/a) and minor (c/a) axis ratios, respectively. We estimate axis ratios with stars in half-mass ellipsoidal radius. The clusters show more oblate shapes as the initial rotation increases.

where a, b and c are axis lengths with $a \geq b \geq c$. The axis ratios are derived from the tensor through

$$\frac{b}{a} = \left(\frac{M_{yy}}{M_{xx}}\right)^{1/2} \quad \text{and} \quad \frac{c}{a} = \left(\frac{M_{zz}}{M_{xx}}\right)^{1/2}, \tag{2.6}$$

where M_{xx}, M_{yy} and M_{zz} are the principal components of the tensor. In order to compute the tensor M_{ij}, we need to know the axis ratios. Therefore, for the simultaneous determination of the tensor and axis ratios, we need to perform an iterative calculation. We, first, assume certain set of axis ratios (e.g., $b/a = 1$ and $c/a = 1$) and compute M_{ij}, which gives another set of axis ratios. Obviously, the resulting axis ratios will be different from the assumed values, and therefore, can be used as an input for improved estimation of M_{ij}. We carry out the iteration until the relative difference of axis ratios becomes less than certain criterion (we include a value of 10^{-4} for this study). Fig. 2.2 shows the axis ratios as a function of initial rotation for M2A models. We calculate axis ratios with stars in the ellipsoidal radius including half-mass of the cluster. The shape of rotating cluster is oblate initially due to the initial rotation (i.e., $b/a = 1$ and $c/a < 1$). The minor axis ratio c/a decreases when the initial rotation increases from 0.3 to 1.5.

In Fig. 2.3, we show the evolution of the axis ratios, b/a and c/a for M2A models with different initial rotations. The left panels are the result of slowly rotating models and right panels are for the rapidly rotating models. The minor axis ratios c/a increases with time for slowly rotating models because the cluster loses angular momentum. For the rapidly rotating models, the intermediate axis ratio decreases at the beginning, because of the development of the bar instability. Due to this instability, cluster shapes become tri-axial or even prolate in a dynamical time scale which is much shorter than the relaxation time. The intermediate axis ratio also decreases during this phase. The decrease of both axis ratios is more rapid when the initial rotation becomes larger. When the ratio $T_{\rm rot}/|W|$ becomes smaller than 0.14 by the loss of the rotational energy as shown in Fig. 2.1, the bar instability disappears and the cluster becomes axisymmetric.

Density contour maps on xy plane of clusters with different initial rotation parameters are shown in Fig. 2.4. The top and bottom panels show the initial shapes

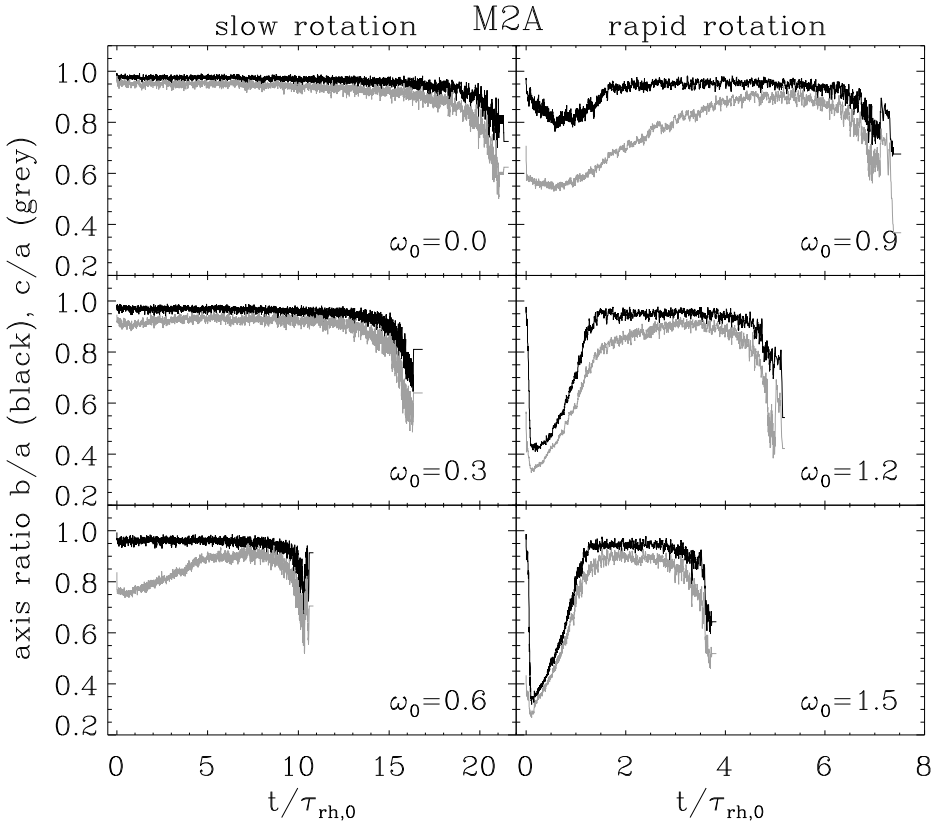

Figure 2.3 Time evolution of intermediate b/a (black) and minor c/a (grey) axis ratios for M2A models. In the early stage for rapidly rotating models, the intermediate axis ratios decrease rapidly due to the bar instability. The shapes of clusters tend to become spherical after a few $\tau_{\rm rh,0}$ due to the significant loss of angular momentum.

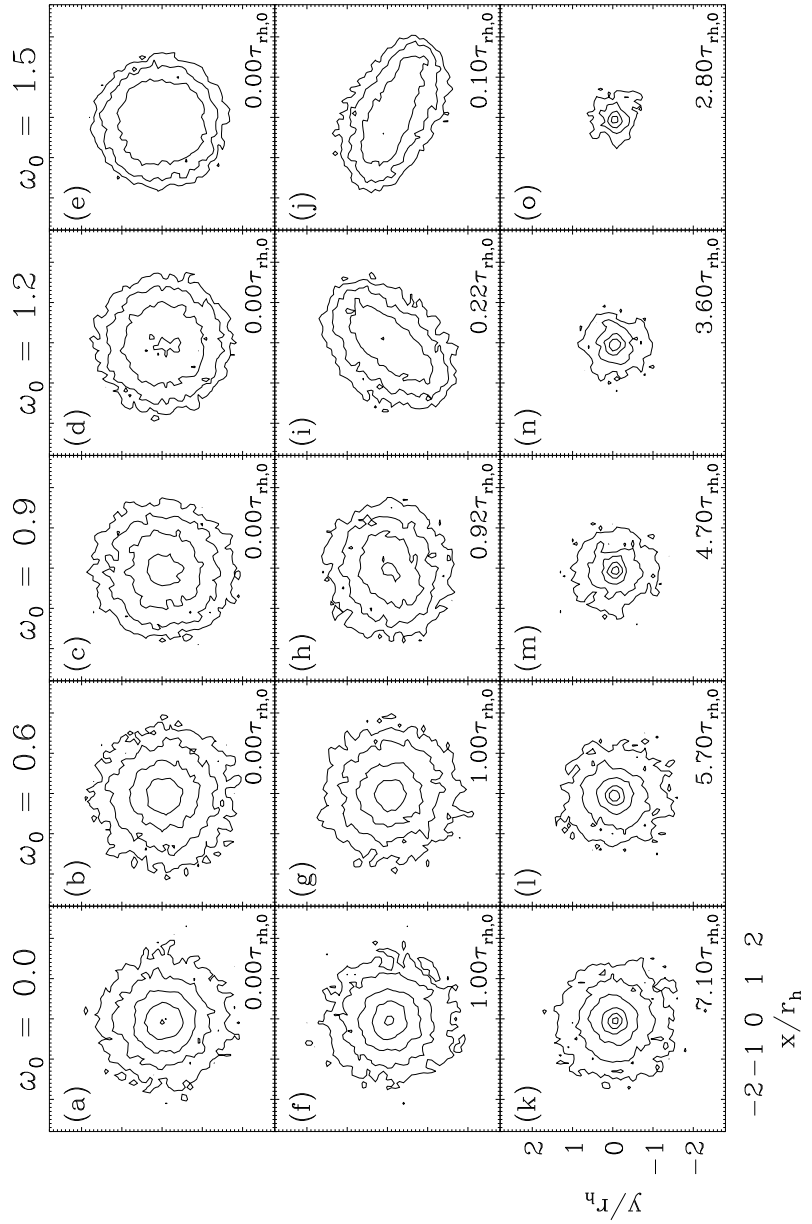

Figure 2.4 Projected density contour maps of M2A models with initial rotation $\omega_0 = 0.0, 0.6, 0.9, 1.2$ and 1.5 on xy plane. The top panels (a-e) show initial models and bottom panels (k-o) show density structures at the time of the core collapse. The middle panels of $\omega_0 = 0.9, 1.2, 1.5$ (h-j) are density structures at the time of maximum elongation.

and the shapes at the core collapse, respectively. In the bottom panels, the size of contours show that the remaining mass of cluster at the core collapse becomes smaller as the initial rotation increases. Density structures for models with $\omega_0 = 0.9, 1.2$ and 1.5 in middle panels represent shapes at the time of maximum elongation. One can clearly observe bar-like structures of rapidly rotating models. Shapes become to be those of the axisymmertic systems at the time of core collapse as shown in Fig 2.3 (i.e., $b/a = 1$ and $c/a < 1$).

2.4 Comparison between N-body and FP results

2.4.1 Mass and energy

In this section, we compare the evolution of N-body and FP simulations for M2A models with three different point of views: overall evolution (mass and energy), central evolution (central density and velocity dispersion) and rotational evolution. Fig. 2.5(a) shows the evolutions of total mass. For the slowly rotating models, the time evolutions of total cluster mass for N-body simulations agree well with those of FP results. However, there exist significant differences between FP and N-body results for the rapidly rotating models. For an instance, N-body calculations show significantly higher mass loss rate than FP results for rapidly rotating models with $\omega_0 = 1.2$ and 1.5, especially in the very early times. The significant amount of mass loss at the very early stage also induces the large amount of angular momentum loss. After this stage, clusters have smaller number of stars with slower rotation and therefore evolve slowly compared to FP results. The time evolutions of total mass of each component are shown in Fig. 2.5(b). Because the number of low mass stars is much larger than that of high mass stars, the evolution of total mass is similar to that of low mass stars.

The total energy of the tidally limited stellar system decreases monotonically with time due to the escaping stars carrying energies. Fig. 2.6(a) shows the time evolution of the normalized total energies. The results of N-body and FP simulations agree well for slowly rotating models. While the total energy decreases slowly in pre-collapse stage, after core collapse the total energy decreases more rapidly due

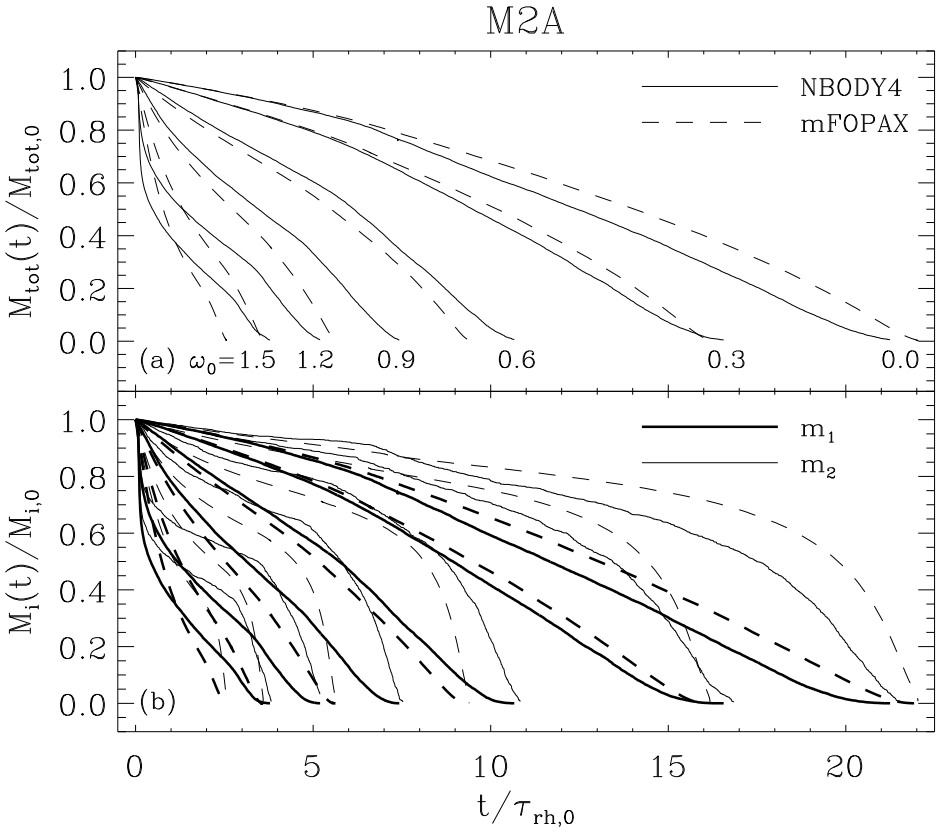

Figure 2.5 Evolution of mass for M2A models: (a) Evolution of total mass. Dashed lines represent FP results, and solid lines show N-body results. The total mass decreases due to escaping stars through the tidal energy threshold. For rapidly rotating models, there are steep mass losses at the early stages because of the bar instability. (b) Time evolution of the mass components m_1 (red) and m_2 (blue). Total mass of m_1 decreases faster than that of m_2.

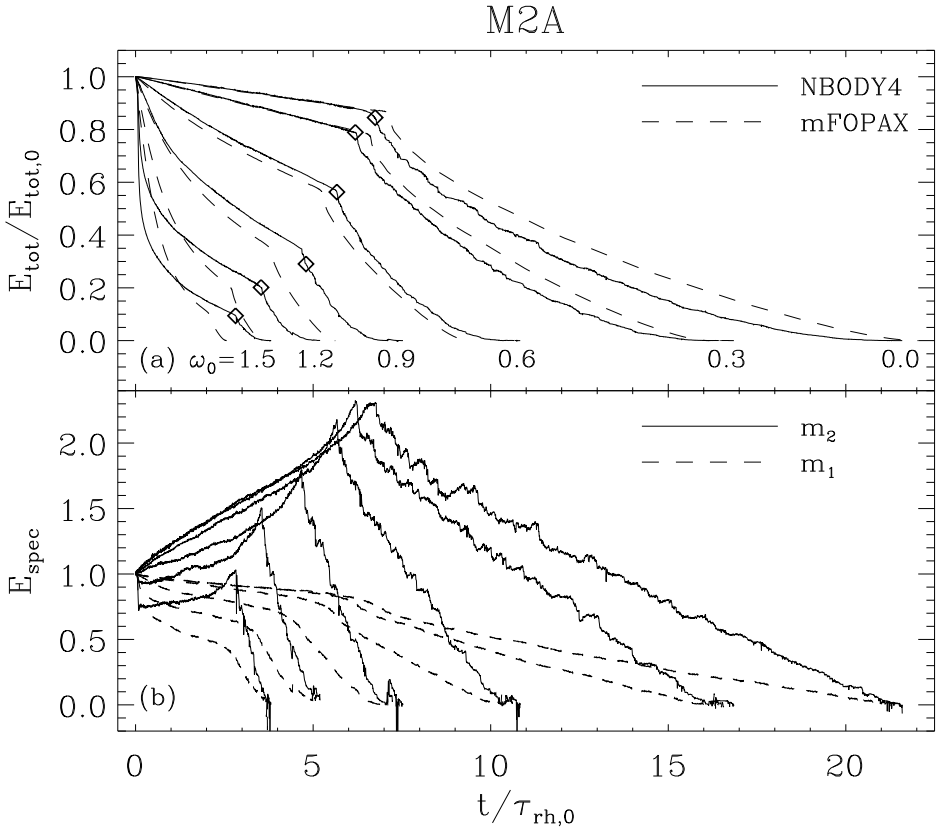

Figure 2.6 Upper panel shows the evolution of the total energy as a function of time. The diamond symbols represent the moment of the core collapse for N-body results. Total energies decrease with time due to escaping stars. After the core collapse, energies decrease more rapidly because of core bounce due to the binary heating. In lower panel, there are the evolutions of the specific energies for m_1 and m_2. The specific energy of m_2 increases quickly during the just prior of the core collapse because high mass stars move to the central region having deep potential due to the mass segregation.

to the core expansion. For the rapidly rotating models, however FP and N-body results show significant difference because of the large amount of energy loss during the early stages for N-body models. Fig. 2.6(b) represents the time evolution of normalized specific energy (i.e., energy per unit mass) for each mass component. In overall, the specific energies of m_1 continue to decrease. On the other hand, the specific energy of m_2 increases slowly till the core collapse as a result of equipartition and mass segregation. However, the specific energies of m_2 decrease after the core collapse due to the mass loss through the tidal boundary because the process of mass segregation stops at the core collapse (i.e. the mean mass of a star in the central region increases until the core collapse and remains as a constant value after the core collapse; see §2.5.3). Note that the mean energies for both low mass and high mass stars immediately decrease for the model of $\omega_0 = 1.2$ and 1.5. Again, this is caused by the bar instability in the early phase of the evolution.

2.4.2 Central density, velocity dispersion and core collapse

Fig. 2.7 shows time evolution of the central density, $\rho_{\rm c}$ and the central velocity dispersion, $\sigma_{\rm c}$ obtained by using stars inside the core radius. The dashed and solid lines represent FP and N-body results, respectively, and different contrasts represent models with different initial rotation. We confirm that the rotation accelerates both the core collapse and cluster disruption (e.g., Kim et al. 2008). In addition, FP and N-body results agree well for slowly rotating models. However, as the initial rotation increases the difference between FP and N-body results becomes large due to the bar instability. Table 2.2 lists the core collapse times and the disruption times of M2A models. For example, the model with $\omega_0 = 1.5$ reaches the core collapse at $2.1\tau_{\rm rh,0}$ and $3.7\tau_{\rm rh,0}$ for FP and N-body calculations, respectively. As the initial rotation ω_0 increases, the cluster spends more time of its whole life in the pre-core collapse phase (i.e., $t_{\rm cc}/t_{\rm dis}$ increases). For N-body simulations, the ratio of the core collapse time to the disruption time $t_{\rm cc}/t_{\rm dis}$ of the model with $\omega_0 = 1.5$ is $\sim$3/4 while that of the model with $\omega_0 = 0$ is $\sim$1/3. We observe that the core collapse and disruption times of N-body results are significantly longer than those of FP results for rapidly rotating models because these models are redefined as small and slowly rotating

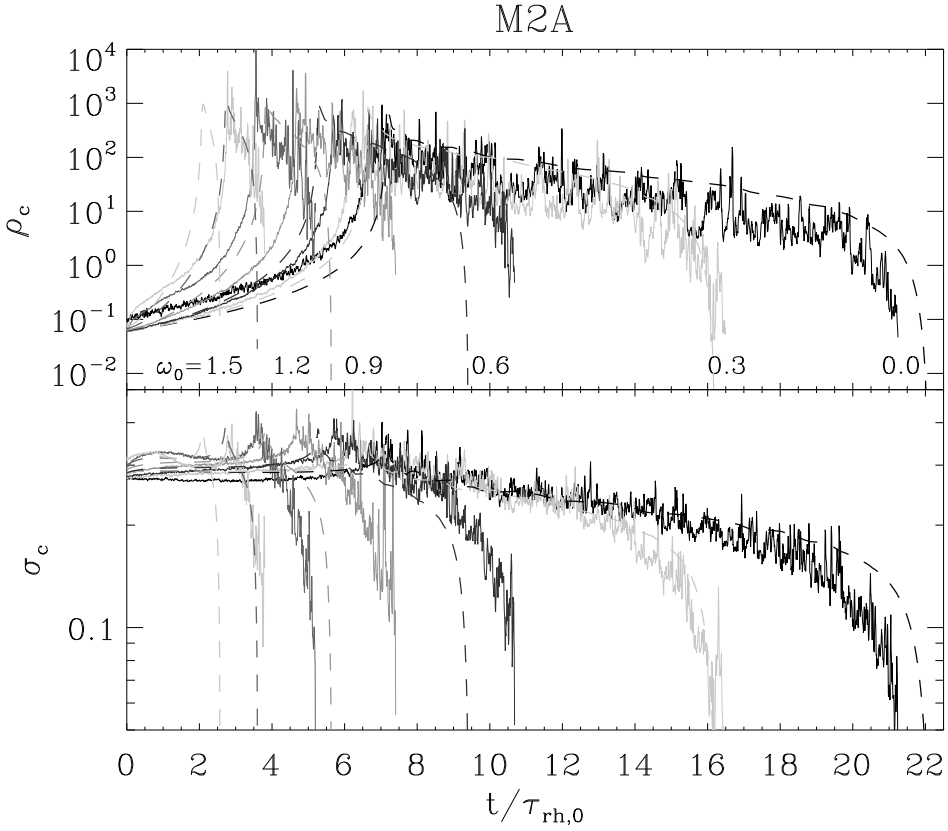

Figure 2.7 Evolution of central density ρ_c and velocity dispersion σ_c for M2A models. Dashed lines represent the FP results and the solid lines for the N-body results. Different contrasts mean models with different initial rotations. ρ_c and σ_c of rapidly rotating models show significant differences between two approaches.

systems after the bar instability. Although there are significant differences between N-body and FP time scales, the total mass at the time of core collapse (designated as $M_{\rm cc}$) of N-body and FP results show a good agreement. The presence of the mass spectrum also accelerates the evolution of cluster (Kim et al. 2004). We found that the core collapse times of M2A models are $20-40\%$ smaller than those of single mass systems considered by Kim et al. (2008). On the other hand, the disruption times are only 10% smaller. We also look into the evolution of clusters with various mass spectra. Table 2.3 shows the collapse and disruption time scales for other N-body models. As m_2/m_1 increases, the evolution of clusters is accelerated. From M2A to M2D models, the core collapse time decreases when m_2/m_1 increases, but is less affected by the initial rotation. The disruption time, however, depends on both the mass spectrum and the initial rotation.

Fig. 2.8 shows the evolution of the central velocity dispersion ($\sigma_{\rm c}$) of each mass component as a function of $\rho_{\rm c}$. $\sigma_{\rm c}$ of m_1 and m_2 are divided into two parts and increase gradually until the core collapse. The total $\sigma_{\rm c}$ approaches that of m_2 because the fraction of high mass stars in the core increases with time and the core is finally filled with high mass starts due to the mass segregation. We can clearly see the equipartition as two distinct branches of $\sigma_{\rm c}$ versus $\rho_{\rm c}$. As a result of equipartition, $\sigma_{\rm c}$ of m_1 becomes about $\sqrt{2}$-times greater than that of m_2 because we use individual mass ratio of $m_2/m_1 = 2$. Once the establishment of energy equipartition, the evolutions of $\sigma_{\rm c}$ of m_1 and m_2 are represented by simple power-law. During the post-core collapse stage, however, FP and N-body results show some differences. N-body results are more dispersive than FP results, unlike the early evolution. This is because there is the large fluctuation of $\rho_{\rm c}$ as shown in Fig. 2.7, which is from the lack of stars within the core radius after core collapse. On the other hand, rapidly rotating models that lead to the bar instability have different evolutionary behaviors between FP and N-body for the very early phase. Because the bar instability delays the relaxation processes, the mass segregation in N-body takes place later compared to FP models. The gap between $\sigma_{\rm c}$ of m_1 and m_2 for N-body results is slightly smaller than that of FP results. This means that the bar instability also affects the equipartition process (see §2.5.2 and Table 2.4 for more details).

Table 2.2 Global evolution of M2A models for NBODY4 and mFOPAX results.

Simul.	ω_0	$t_{\rm cc}/\tau_{\rm rh,0}$	$t_{\rm dis}/\tau_{\rm rh,0}$	$t_{\rm cc}/t_{\rm dis}$	$M_{\rm cc}$
(1)	(2)	(3)	(4)	(5)	(6)
	0.0	7.1	22.0	0.32	0.80
	0.3	6.7	15.9	0.42	0.70
mFOPAX	0.6	5.3	9.2	0.58	0.52
	0.9	3.8	5.7	0.67	0.36
	1.2	2.7	3.7	0.73	0.23
	1.5	2.1	2.5	0.84	0.14
	0.0	6.8	21.2	0.32	0.80
	0.3	6.2	16.3	0.38	0.72
NBODY4	0.6	5.7	10.4	0.55	0.54
	0.9	4.8	7.1	0.68	0.35
	1.2	3.6	5.2	0.69	0.23
	1.5	2.8	3.7	0.76	0.15

Note. - (1): Simulation methods. (2): Initial rotation parameter. (3): Core collapse time divided by the half-mass relaxation time. (4): Disruption time divided by the half-mass relaxation time. (5): Ratio of core collapse time to disruption time. (6): Remaining mass fraction at the moment of core collapse.

Table 2.3 Global evolution of other NBODY4 models.

Model	ω_0	$t_{\rm cc}/\tau_{\rm rh,0}$	$t_{\rm dis}/\tau_{\rm rh,0}$	$t_{\rm cc}/t_{\rm dis}$	$M_{\rm cc}$
(1)	(2)	(3)	(4)	(5)	(6)
	0.0	1.61	10.18	0.16	0.94
M2B	0.6	1.64	5.01	0.33	0.79
	1.2	1.38	2.16	0.64	0.34
	0.0	0.59	5.92	0.10	0.97
M2C	0.6	0.62	2.79	0.22	0.89
	1.2	0.70	1.36	0.51	0.44
	0.0	0.42	3.59	0.12	0.96
M2D	0.6	0.34	1.65	0.21	0.91
	1.2	0.36	0.72	0.5	0.55
	0.0	9.37	27.56	0.34	0.73
M2Ae	0.6	6.72	12.86	0.52	0.49
	1.2	4.05	5.89	0.69	0.22

Note. - (1): Simulation models. (2)-(6): Same as the Table 2.2

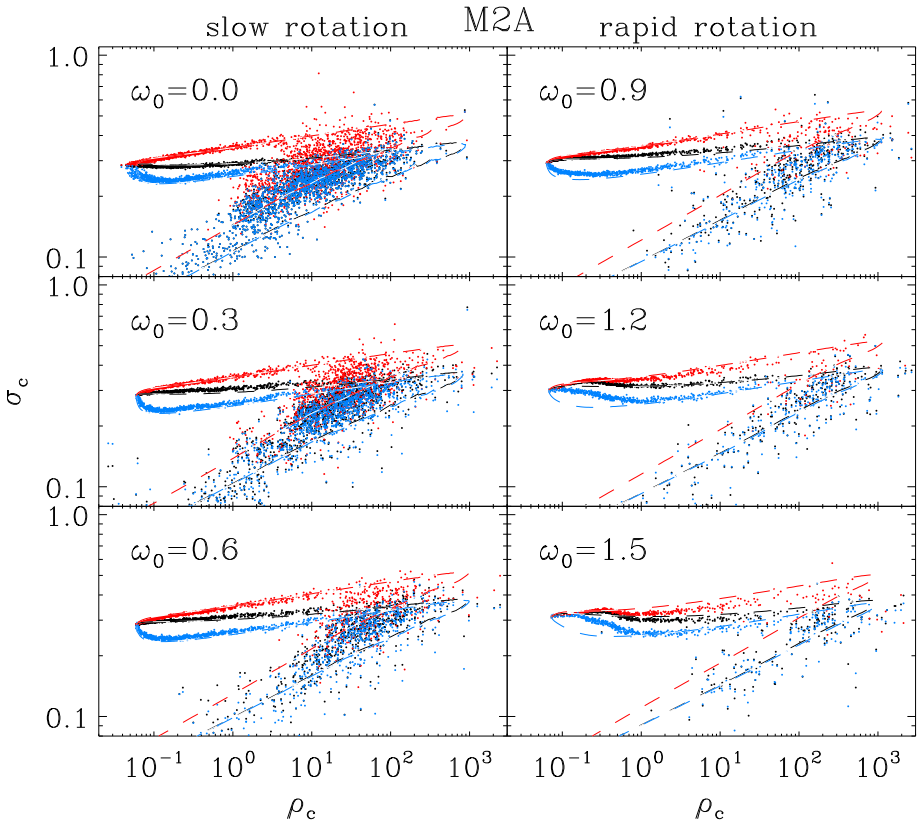

Figure 2.8 Central velocity dispersion σ_c for m_1 (red), m_2 (blue) and all stars (black) as a function of central density ρ_c. Dots show N-body results, and dashed lines mean FP results. Initially, σ_c for both mass components are the same. They evolve into the different ways due to the equipartition. σ_c for low mass becomes about $\sqrt{2}$-times larger than that for high mass because of equipartition.

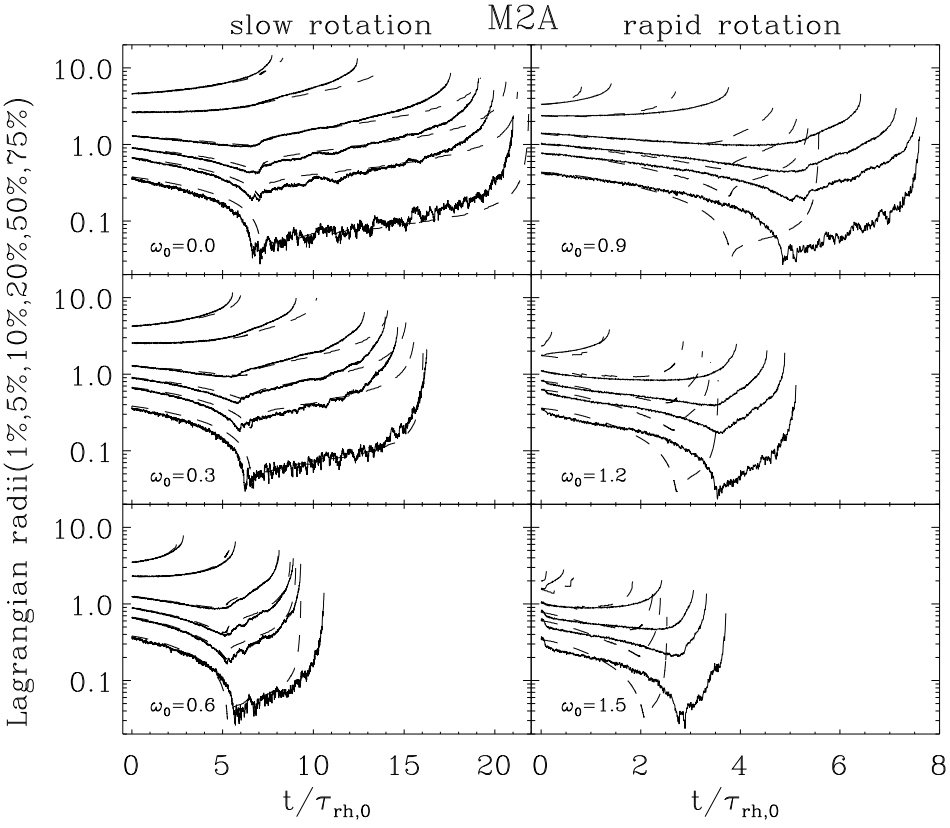

Figure 2.9 Lagrangian radii including 1, 5, 10, 20, 50, 75 per cent of initial cluster mass for M2A models. For rapidly rotating models, the results of N-body and FP shows significant differences while those for slowly rotating models are similar.

In Fig. 2.9, we show the time evolution of the Lagrangian radii for M2A models. We estimate Lagrangian radii containing 1, 5, 10, 20, 50 and 75 per cent of initial cluster mass. The dashed lines and the solid lines represent the FP and N-body results, respectively. Although our models are flattened due to the initial rotation and become triaxial by the bar instability, we use the spherical radius to estimate these Lagrangian radii for the simplicity of comparison between N-body and FP simulations. We found that, for the slowly rotating models, the results of FP and N-body show an excellent agreement except for the final stages when there are only small number of stars in the clusters. However, for the rapidly rotating models, the results of FP and N-body are significantly different. Again, the bar instability and induced mass loss are the main reason for these differences.

2.4.3 Rotational properties

To understand the effects of initial rotations on the cluster dynamics, we investigate the evolution of angular momentum. Because we assume that stars escape through the tidal energy threshold, clusters lose their angular momentum continuously. Also, we expect exchange of angular momentum between different mass components, similar to energy exchange. After encounters, stars that lose their energy spiral into the central parts while stars that gain the energy move outward. Also, loss of angular momentum makes the orbits of stars be eccentric but gaining angular momentum does the orbits be less eccentric. Fig. 2.10 shows the time evolution of specific angular momentum which is defined as

$$\mathbf{L}_{\rm spec} = \frac{\sum_i m_i \mathbf{r}_i \times \mathbf{v}_i}{\sum_i m_i} \tag{2.7}$$

where $\mathbf{r}_i$, $\mathbf{v}_i$ are relative positions and velocities of stars to the center of mass, respectively, and we integrate all stars in the cluster to compare N-body and FP results. $L_{z,\rm spec}$ is z-direction component of $\mathbf{L}_{\rm spec}$. Solid lines are the results of N-body and dashed lines represent the results of FP. Red and blue colors show low and high mass stars, respectively. For slowly rotating models, the results of N-body and FP are similar. The specific angular momenta decrease monotonically. Due to the mass segregation, high mass stars that encounter with many low mass stars migrate

to the inner part where rotational velocity is smaller than that of the outer part of the cluster (see rotation curves in Fig. 2.12a and Fig. 2.15a). This is also related to the angular momentum exchange between different mass components (see §2.5.4 for more details). Thus, the specific angular momentum of m_2 becomes smaller than that of m_1 during the evolution. The difference of angular momentum between two mass components is most prominent at the core collapse, where the core collapse time is marked as diamond symbols in Fig. 2.10. For the models with $\omega_0 = 1.2$ and 1.5, the angular momentum decreases rapidly during the early stage. In addition, there is no clear split of the specific angular momentum of low and high mass stars due to the rapid evolution induced by the bar instability. Interestingly, the model with $\omega_0 = 0.9$ shows the transitional evolution. While the model still has a triaxial shape ($T < 1.5\tau_{\rm rh,0}$, see Fig. 2.3), the evolution is similar to that of the models with $\omega_0 = 1.2$ and 1.5. However, after the shape becomes the axisymmetric again, the evolution is similar to that of the models with $\omega_0 = 0.3$ and 0.6.

Slow rotation ($\omega_0 = 0.6$)

To investigate the evolution of rotational properties of our cluster models, we focus on rotational velocities, V_ϕ of two models in detail. As a representative of slowly rotating models, we chose a rotating model with $\omega_0 = 0.6$ of M2A. Fig. 2.11 shows the distribution of V_ϕ at four different epochs $T = 0, 3, 5.7$ and $8\tau_{\rm rh,0}$. The core collapse time is $T = 5.7\tau_{\rm rh,0}$. We combined results of three runs with N =20,000. At $T = 0$, the distribution is asymmetric to the positive direction due to the initial rotation. The dispersion of V_ϕ is large at the center and becomes smaller along the cylindrical radius, $R \equiv (x^2 + y^2)^{1/2}$. As the cluster loses its mass and angular momentum, the size of cluster and the degree of asymmetry in V_ϕ decrease with time. Finally, the distribution of V_ϕ becomes symmetric compared to the initial distribution. The rotation curves of both mass components are shown in Fig. 2.12(a). The rotation curves of m_1 and m_2 are identical at $T = 0$ because we assume that the distribution of positions and velocities for both mass components are the same initially. At $T = 3\tau_{\rm rh,0}$, the rotation velocity of m_1 becomes smaller at all radii because low mass stars with large angular momenta escape from the system. On the

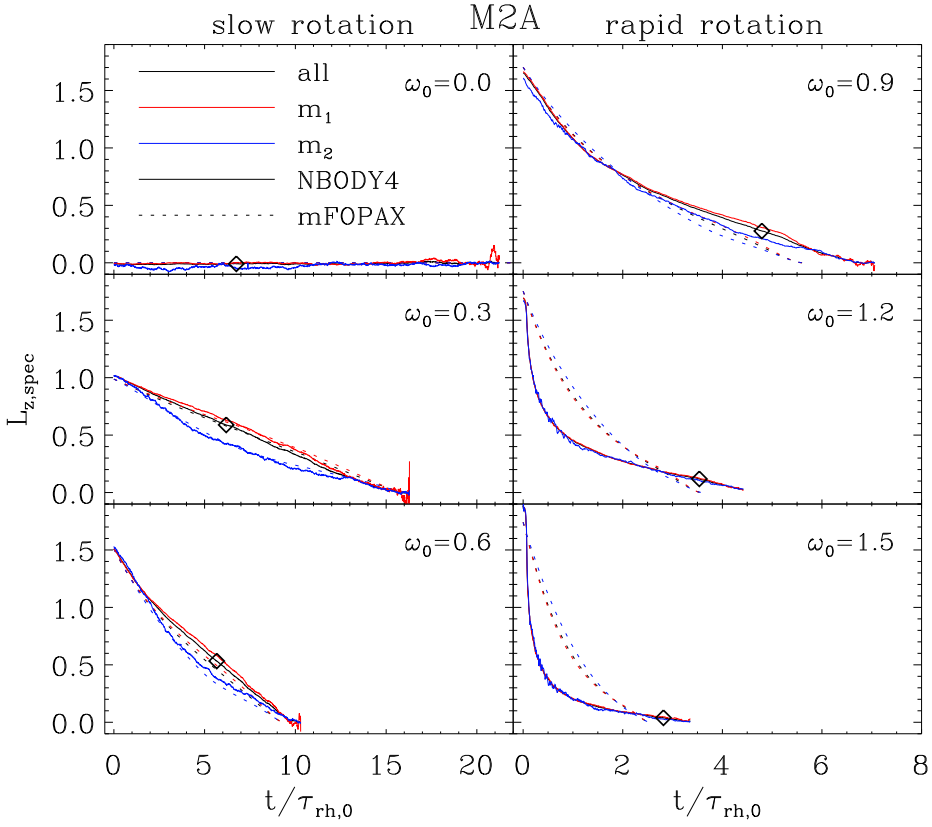

Figure 2.10 Time evolution of the specific angular momentum $L_{z,\mathrm{spec}}$. Solid lines are the results of FP and dashed lines are the results of N-body. Red and blue colors mean low mass and high mass stars, respectively. Diamond symbols represent the moment of the core collapse. For slowly rotating models (left panels), $L_{z,\mathrm{spec}}$ of m_1 and m_2 are divided. However, $L_{z,\mathrm{spec}}$ of m_1 and m_2 decrease quickly compared to the results of FP for rapidly rotating models (right panels).

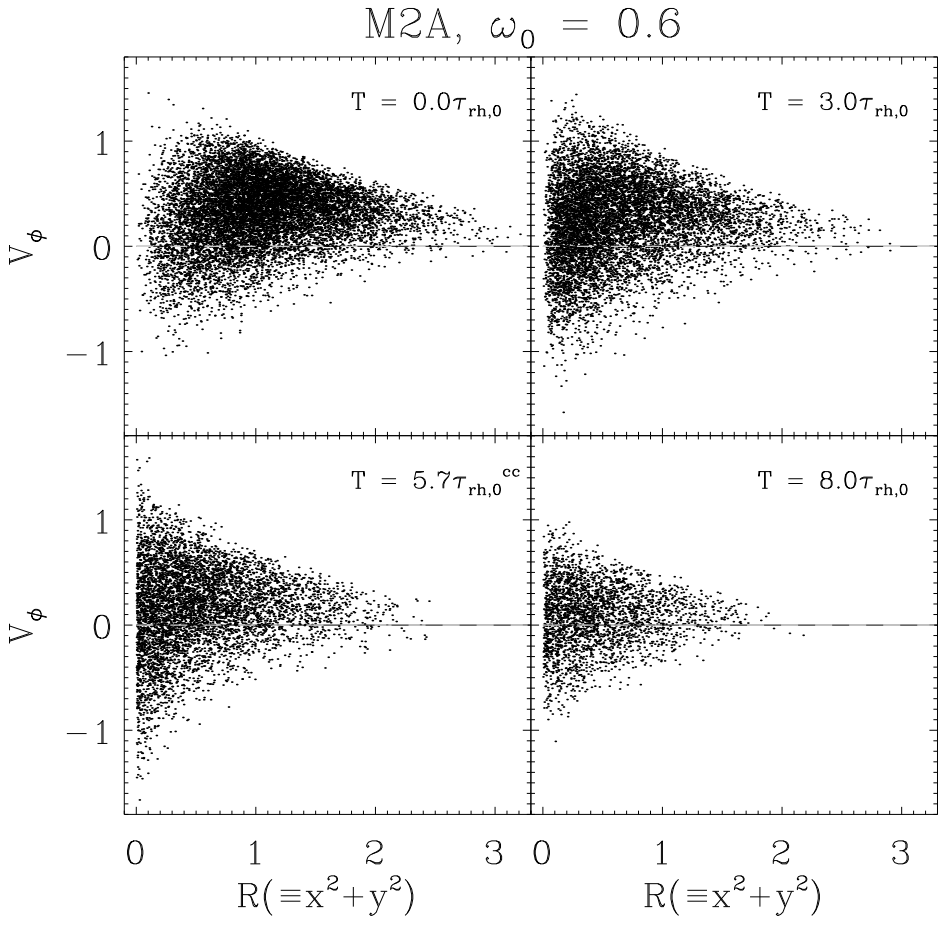

Figure 2.11 Distribution of the rotational velocities of stars as a function of cylindrical radius. The cluster's size and degree of the anisotropy decrease with time.

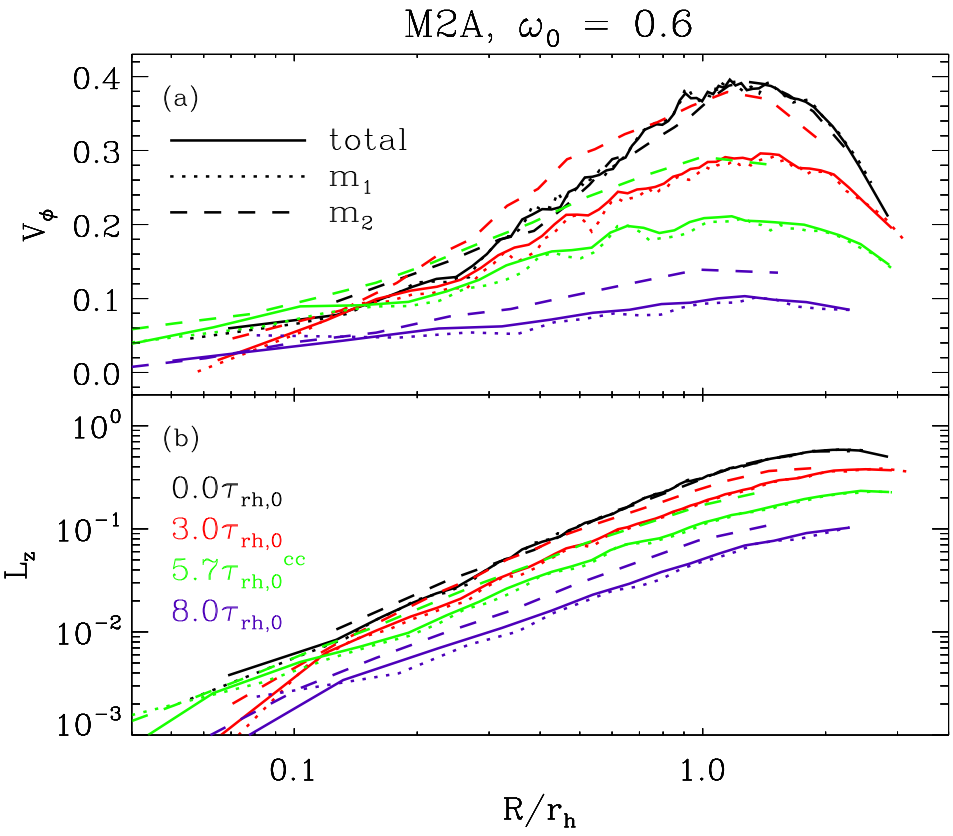

Figure 2.12 Upper panel shows rotation curves at time $T = 0, 3, 5.7$ (core collapse) and $8\tau_{\rm rh,0}$. Solid, dotted and dashed lines mean the rotation curves of all stars, high mass stars and low mass stars, respectively. At time $T = 0$, rotation curves are similar between low and high mass components. However, after few $\tau_{\rm rh,0}$, the rotation curve of m_1 drops while that of m_2 remains. The curve of z-direction angular momentum is shown in lower panel. Angular momenta also decrease with time.

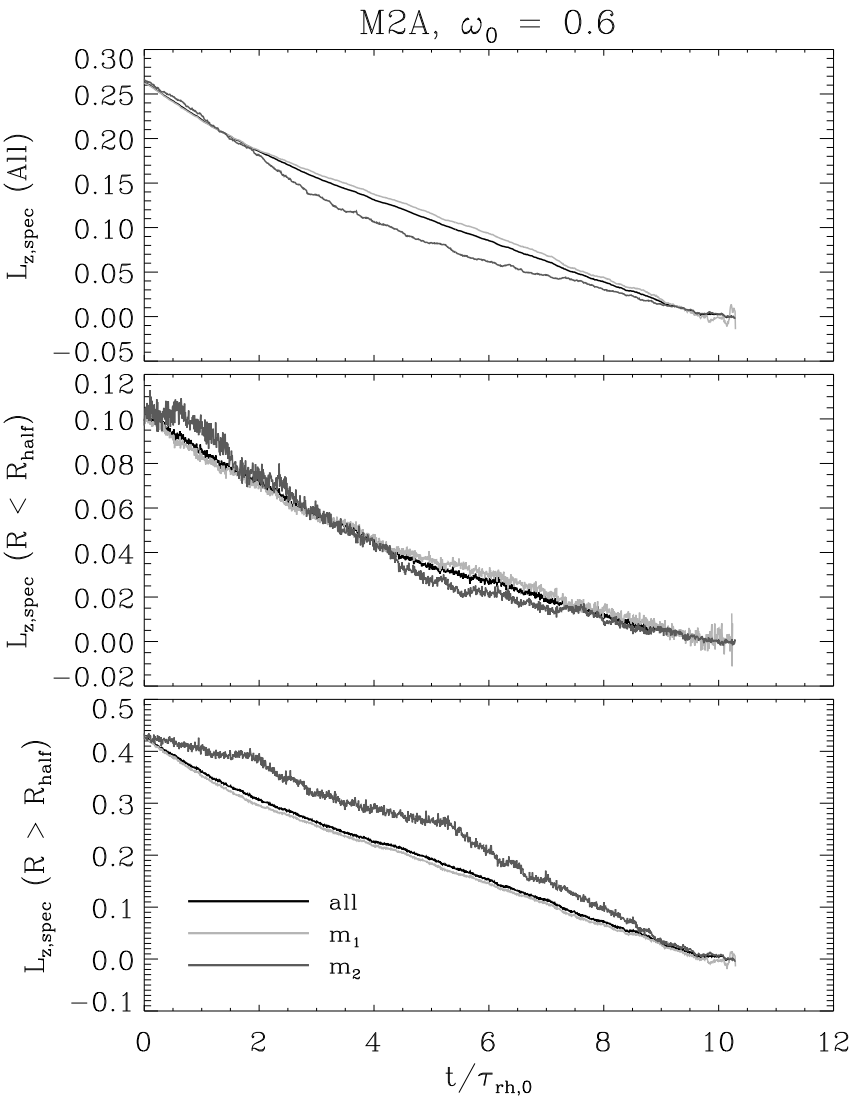

Figure 2.13 Time evolution of z-direction specific angular momentum $L_{z,\mathrm{spec}}$ (upper), $L_{z,\mathrm{spec}}$ of inner half-mass (middle) and $L_{z,\mathrm{spec}}$ of outer half-mass (lower). Though the angular momentum curve of high mass components is larger than low mass components at all radii, $L_{z,\mathrm{spec}}$ of high mass components in whole cluster becomes smaller than low mass components after few $\tau_{\mathrm{rh},0}$. This is because most of high mass components are located in central region which rotates slowly due to the mass segregation. The evolution of the inner region shows similar behavior with that of whole cluster. On the other hand, for the outer region, $L_{z,\mathrm{spec}}$ of high mass components is higher than that of low mass components always.

other hand, the rotation curve of m_2 remains as that of the initial curve for longer time. At $T = T_{\rm cc}$, the rotation velocity of m_2 also decreases but is still higher than that of m_1. The cluster rotates very slowly at $T = 8\tau_{\rm rh,0}$. At this time, the rotation curves of m_1 and m_2 are flattened compared to other epochs. It is interesting to note that the peak position remains at a constant value measured in the units of half-mass radius while the peak rotation velocity decreases.

Fig. 2.12(b) shows the radial profiles of mean angular momentum for m_1 and m_2. The angular momentum curves of m_1 and m_2 are identical at $T = 0$ and L_z of m_1 decreases more rapidly compared to that of m_2. Initially, the curve is a power-law with index of 1.5 within $r_{\rm h}$ (e.g., the power law index is 2 for a rigid body rotation.). The power law index becomes smaller and goes to one at $T = 8\tau_{\rm rh,0}$ because the rotation curve becomes flatter. In Fig. 2.13, we show evolutions of specific angular momentum $L_{z,\rm spec}$ in different radial ranges: in the whole cluster, within half-mass radius and outside of half-mass radius. $L_{z,\rm spec}$ decreases with time due to the escaping stars with angular momenta. In the entire cluster, $L_{z,\rm spec}$ of m_1 and m_2 decrease together until $T = 2\tau_{\rm rh,0}$. Although L_z of m_2 is larger than that of m_1 at the all radii as shown in Fig. 2.12(b), $L_{z,\rm spec}$ of m_2 becomes smaller than that of m_1 because high mass component tends to be more concentrated in the central region than low mass stars due to mass segregation (see §2.5.3 for more details). Within the half-mass radius, $L_{z,\rm spec}$ of m_1 decreases continuously while that of m_2 remains at a constant value until $T \approx 0.5\tau_{\rm rh,0}$ because the rotation curve of high mass stars remains as the initial curve for a while as shown in Fig. 2.12(a) and Fig. 2.12(b). After a few $\tau_{\rm rh,0}$, the evolution of inner region follows that of entire cluster due to the mass segregation. For the outer region, $L_{z,\rm spec}$ of m_2 is higher than that of m_1 throughout the whole evolutionary phase. Even for the mass segregation, the mean mass of outer region (see Fig 2.19) does not change significantly. It means that the mass fraction of the outer region is less affected than that of inner region. Thus, the mean rotation of m_2 is still faster than the rotation of m_1 beyond half-mass radius. Finally, the cluster loses most of its mass and angular momentum at the end of evolution.

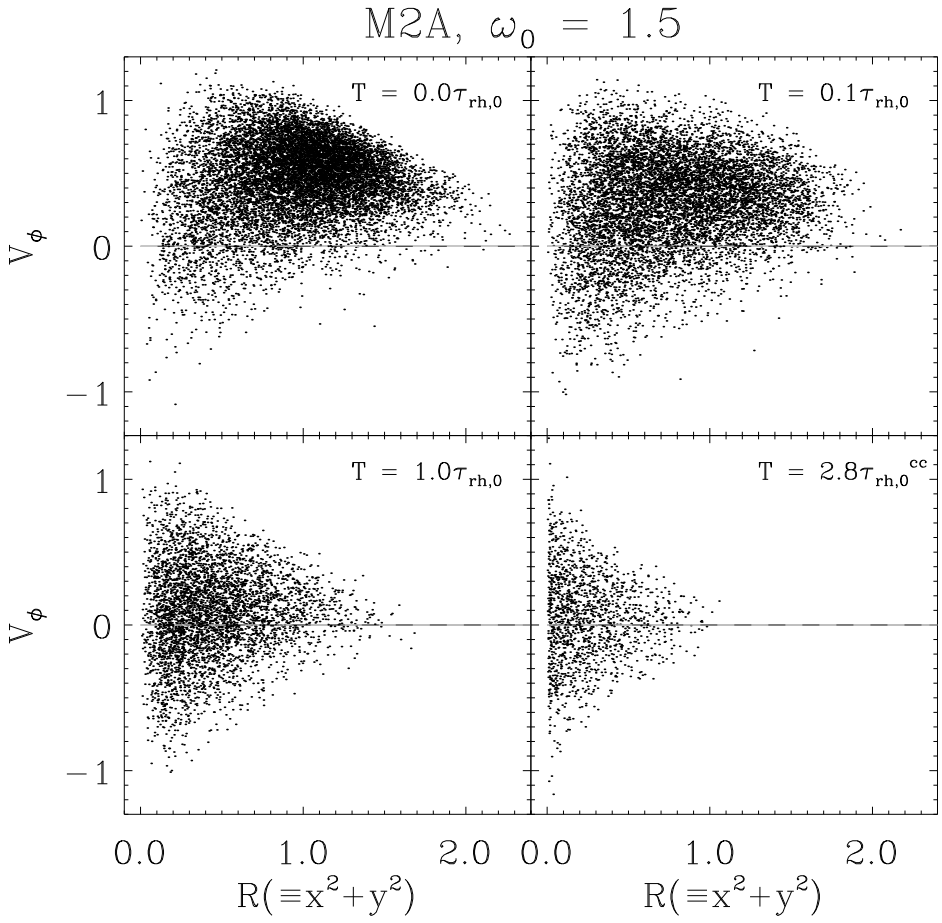

Figure 2.14 Distribution of the rotational velocities of stars as a function of cylindrical radius for the model with $\omega_0 = 1.5$. Initially, most of stars have positive rotational velocities. However, the asymmetry rapidly decreases within a $\tau_{\rm rh,0}$.

Fast rotation ($\omega_0 = 1.5$)

We also investigate the evolution of rotational properties for the model with $\omega_0 = 1.5$. As we mentioned earlier, this model is unstable against bar instability and the shape of cluster quickly becomes a prolate with the largest elongation at $T \sim 0.1\tau_{\rm rh,0}$. In Fig. 2.14, we show the distribution of tangential velocities V_ϕ of stars at $T = 0, 0.1, 1$ and $2.8\tau_{\rm rh,0}$ (core collapse). Initially, the distribution is more skewed toward the positive direction than the model with $\omega_0 = 0.6$ as shown in Fig. 2.11. Only less than 10% of stars have negative value at $T = 0$. The distribution becomes symmetric and also the size of cluster becomes smaller as similar to the model with $\omega_0 = 0.6$. At core collapse, only about 10% of stars remain in the cluster and the cluster rotate slowly. Fig. 2.15(a) shows the rotation curve at $T = 0, 0.1, 1$ and $2.8\tau_{\rm rh,0}$. The rotation curves of m_1 and m_2 decrease together, indicating that the bar instability (i.e., large mass, energy and angular momentum loss) disturbs the relaxation processes. The peak of rotational velocity decreases rapidly with time. However, the peak position at $T = 0.1\tau_{\rm rh,0}$ is slightly larger than the other epochs due to the effect of bar from the instability. At core collapse, the rotation curve is nearly flat but still remains, though the cluster lose most of the mass and the angular momentum. The mean angular momentum along the radius is shown in Fig. 2.15(b). Similar to the result of model with $\omega_0 = 0.6$, it shows a power-law distribution. Initially, the power law index is $\sim$2 within $r_{\rm h}$ like a rigid body rotation but it becomes close to 1 at core collapse.

2.5 Discussion

2.5.1 Mass evaporation

To investigate the evolution of mass in detail, we first define the dimensionless mass evaporation rate such as

$$\xi_{\rm e} \equiv -\frac{\tau_{\rm rh}}{M}\frac{dM}{dt} \tag{2.8}$$

where $\tau_{\rm rh}$ and M are the half-mass relaxation time and total mass of a cluster at time T, respectively. Fig. 2.16 shows the behavior of $\xi_{\rm e}$ of N-body and FP simulations

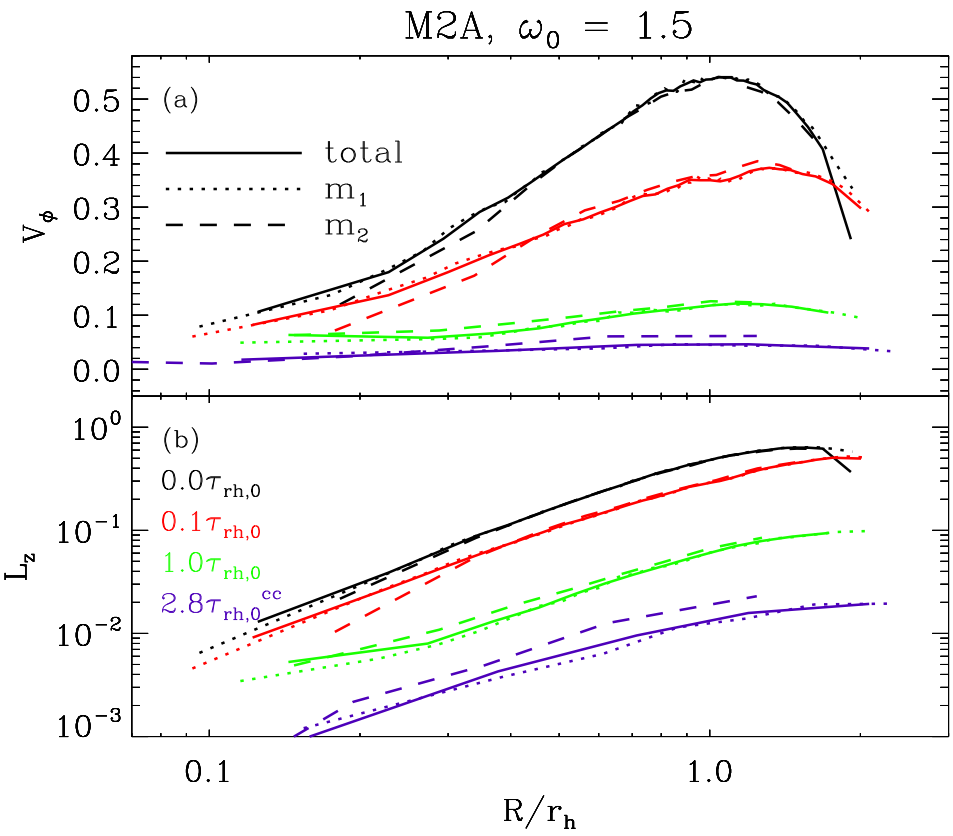

Figure 2.15 Rotation curves at time $T = 0, 0.1, 1$ and 2.8 (core collapse) $\tau_{\rm rh,0}$ with $\omega_0 = 1.5$ (upper). Lines have same meaning to those of Fig. 2.12. At time $T = 0$, rotation curves are similar between low and high mass components. Unlike rotation curves of in Fig 2.12, those of low and high mass components are not divided much. Curves of z-direction angular momentum are shown in lower panel.

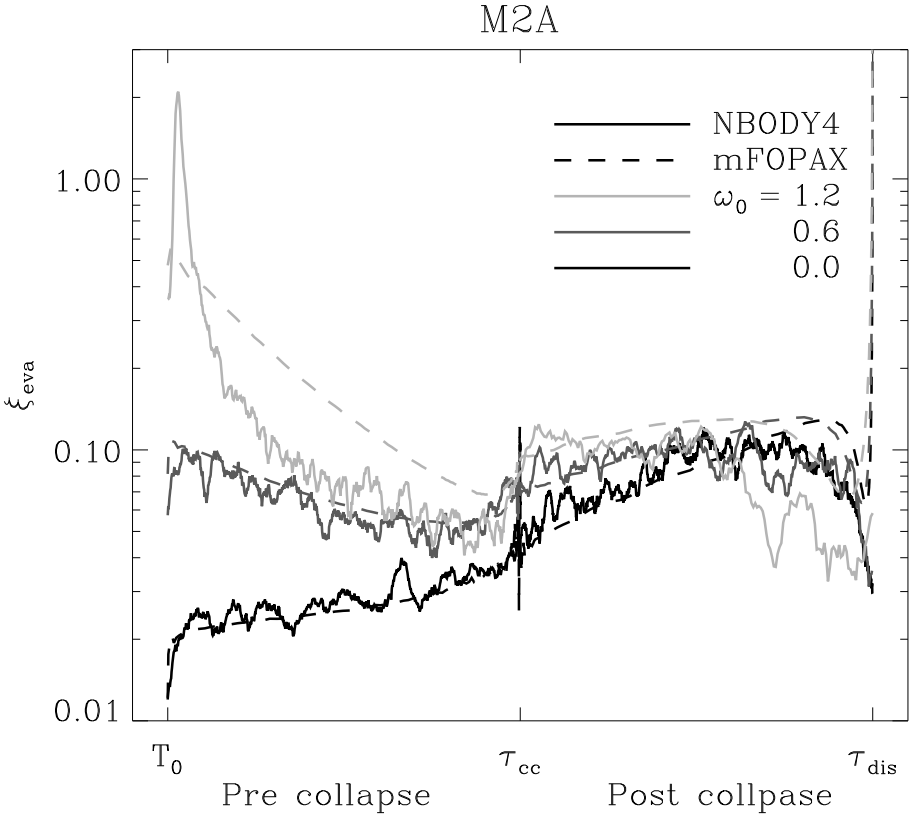

Figure 2.16 Dimensionless mass evaporation rate. X-axis means the evolutionary phase (i.e.; pre- or post-core collapse). For $\omega_0 = 0.0$ and 0.6, the result of N-body and FP are well agreed. On the other hand, for $\omega_0 = 1.2$, there is a spike meaning large mass loss induced by the bar instability in N-body result.

for M2A models with ω_0 =0.0, 0.6 and 1.2. We divide the evolution into pre- and post-core collapse phases to investigate the evolution of ξ_e more clearly. The mass evaporation rates are known to be constant for self-similar case (e.g., Hénon 1961; Lee & Ostriker 1987). However, the rate changes with time because our models are not self-similar. In early phase, ξ_e increases with the initial rotation. For slowly rotating models, we see a very good agreement between N-body and FP results in pre-core collapse phase. On the other hand, for model with $\omega_0 = 1.2$, there is a significant difference between results of N-body and FP. The N-body results show a spike at the early time while FP results decrease monotonically. This spike is related to the rapid mass loss induced by the bar instability. After the spike, ξ_e of N-body suddenly decreases below ξ_e of FP result. It is interesting that $\xi_{e,cc}$, the mass evaporation rate at the core collapse, of N-body and FP show similar results even though there is a big difference before core collapse. After core collapse, ξ_e of N-body and FP increase toward a peak value and decrease afterward. The large differences of ξ_e between N-body and FP results at the end of the evolution is due to small number of remaining stars and thus do not have statistical significance. Kim et al. (2002) carried out FP simulations for rotating clusters with single mass system. They also calculated ξ_e with different initial rotation ω_0 =0.0, 0.3 and 0.6. We notice that the evolutionary shapes are similar between single mass and the 2-component mass systems. However, ξ_e for 2-component mass systems show about 30% enhancement compared to ξ_e for single mass systems in pre-core collapse phase. This enhancement could have been induced by the energy exchange process in multi-component models, as noticed by Lee & Goodman (1995). They calculated ξ_e with various initial mass functions and found that ξ_e increases when the cut-off mass ratio (i.e., m_f/m_i if the mass ranges from m_i to m_f) increases. To confirm the relationship between the mass evaporation rate and the mass ratio, we compute the maximum evaporation rate after the core collapse $\xi_{e,post}$ for N-body results with various mass spectra. Fig. 2.17 shows $\xi_{e,post}$ as a function of the individual mass ratio m_2/m_1. As shown in Fig. 2.16, the peak ξ_e in post-core collapse phase are very similar with different initial rotations, so we average the results of each mass spectrum for different initial rotations. $\xi_{e,post}$ of M2A-D models increases with increasing m_2/m_1 and follows a simple power-law.

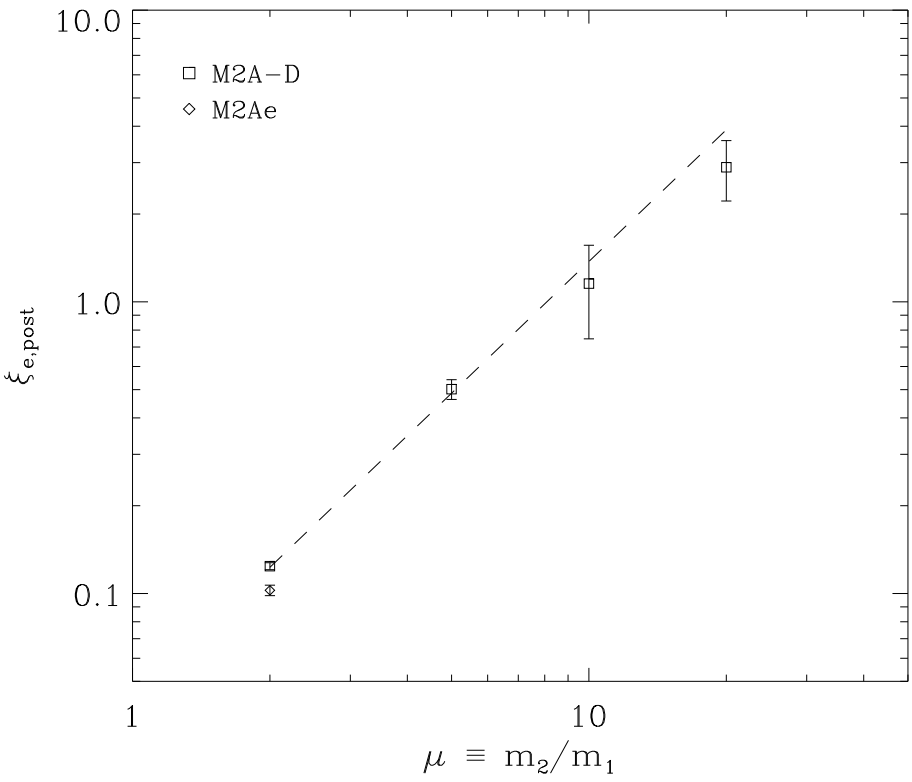

Figure 2.17 Maximum mass evaporation rate $\xi_{e,post}$ after core collapse as a function of the individual mass ratio. Error bars show standard deviations of data of $\xi_{e,post}$ for different mass spectra.

For M2Ae model, $\xi_{\rm e,post}$ is slightly smaller than that of M2A model because the fraction of high mass stars for M2Ae model is small.

2.5.2 Energy equipartition

As presented in §2.4.2, high and low mass stars in the core approach to the 'thermal' equilibrium state by the two body relaxation. To investigate the energy equipartition in detail, we adopt the equipartition parameter

$$\xi_{\rm eq} = \frac{m_2 {\sigma_2}^2}{m_1 {\sigma_1}^2} \tag{2.9}$$

like previous studies (Watters et al. 2000; Khalisi et al. 2007). We calculated $\xi_{\rm eq}$ for stars inside the core radius. Fig. 2.18 shows the evolution of $\xi_{\rm eq}$ for models M2Ae and M2D without initial rotation for examples. Dotted lines represent the core collapse time. For the M2Ae model, $\xi_{\rm eq}$ approaches to unity and becomes less than unity at some moments. However, for the M2D model, $\xi_{\rm eq}$ never approaches to unity. The data is very noisy after the core collapse because only a few low mass stars remain in the core. To determine the minimum value $\xi_{\rm eq,min}$, we find the best polynomial fitting function by varying the order from 5 to 15.

Table 2.4 lists $\xi_{\rm eq,min}$ of all models. Only M2Ae models with $\omega_0 = 0.0$ and 1.2 have lower $\xi_{\rm eq,min}$ than 1.05 which is the value used in Khalisi et al. (2007) for the energy equipartition. On the other hand, $\xi_{\rm eq,min}$ increases when the equipartition instability parameters S or Λ become larger. $\xi_{\rm eq,min}$ for slowly rotating models (i.e., $\omega_0 \leq 0.6$) are similar to each other. There are, however, significant differences of $\xi_{\rm eq,min}$ between slowly rotating models and rapidly rotating models. For M2A models with $\omega_0 \geq 0.9$, $\xi_{\rm eq,min}$ increases gradually with initial rotation. This is another phenomenon of the bar instability obstructing the relaxation process.

2.5.3 Mass segregation

A simple method measuring the degree of the mass segregation is suggested by Giersz & Heggie (1996). They calculated the mean mass in a space between different Lagrangian radii (i.e., Lagrangian shells) to see the change of mass distribution in un-equal mass systems. More recently, Khalisi et al. (2007) carried out N-body

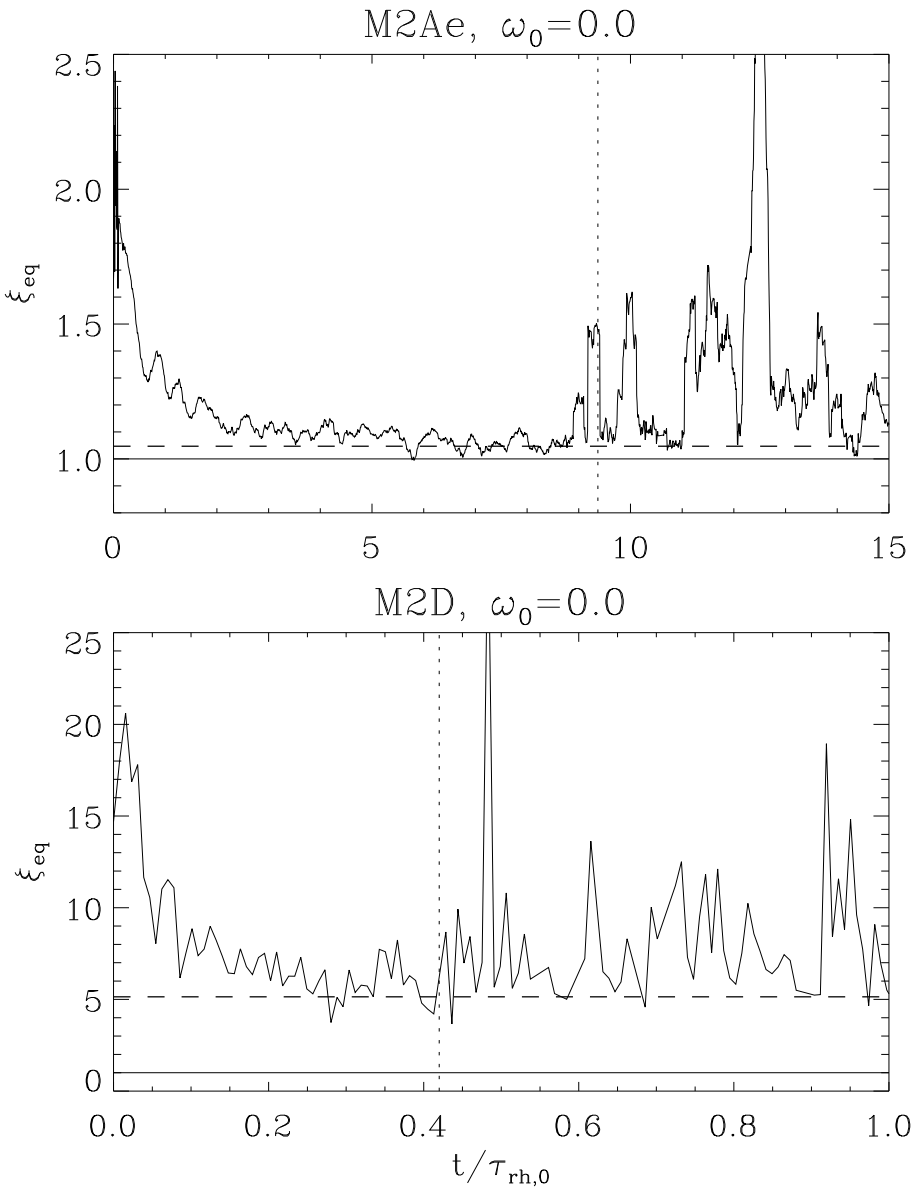

Figure 2.18 Examples for the evolution of the equipartition parameter $\xi_{\rm eq}$. Dashed lines mean the minimum values $\xi_{\rm eq,min}$, and dotted lines show the core collapse time. The determination of $\xi_{\rm eq,min}$ is mentioned in text.

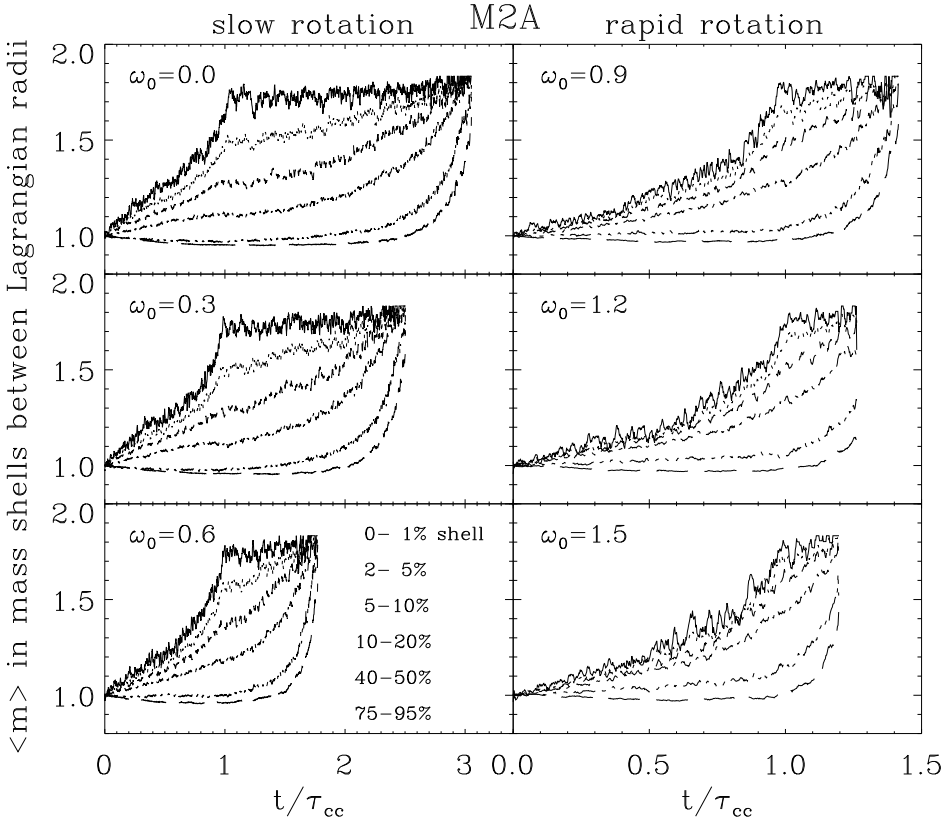

Figure 2.19 Mean mass in mass shells between different Lagrangian radii with different initial rotations. Mean masses of inner shells increase with time before the core collapse while mean masses of outer shells decrease. This shows the process of the mass segregation. After the core collapse, mean masses of other shells also increase with somewhat time gaps but this is not from the mass segregation but because low mass stars escape more frequently than high mass stars.

Table 2.4 $\xi_{\rm eq,min}$ of all models.

Model	S	Λ	ω_0	$\xi^a_{\rm eq,min}$	Model	S	Λ	ω_0	$\xi^a_{\rm eq,min}$
M2A	0.566	1.056	0.0	1.105	M2C	6.325	50.24	0.0	3.017
	-	-	0.3	1.091		-	-	0.6	2.923
	-	-	0.6	1.107		-	-	1.2	3.314
	-	-	0.9	1.123	M2D	17.89	256.2	0.0	5.141
	-	-	1.2	1.158		-	-	0.6	5.224
	-	-	1.5	1.201		-	-	1.2	6.672
M2B	2.236	9.518	0.0	1.664	M2Ae	0.141	0.264	0.0	1.047
	-	-	0.6	1.630		-	-	0.6	1.071
	-	-	1.2	1.860		-	-	1.2	1.000

[a]Minimum equipartition parameter from the best polynomial fitting function.

simulations with different mass spectra and found that the mass segregation occurs inward direction (i.e., the mean mass of each shell is decoupled stepwise from outside, see models A and B in Fig. 6 of Khalisi et al. (2007)). Fig. 2.19 shows the evolution of mean mass in different Lagrangian shells as a function of time. In pre-core collapse phase, due to the mass segregation, the mean mass of the innermost shell increases while mean masses decrease in outer shells. Note that the maximum mean mass of the innermost shell does not depend on the initial rotation and also the innermost shell is nearly fully-occupied by high mass stars (i.e., $\langle m\rangle \approx m_2 = 1.833$) at the time of core collapse. The mean mass of the innermost shell stays at a constant value after the core collapse. According to Giersz & Heggie (1996), after the core collapse, mean masses of inner shells with $r < r_{20\%}$ slightly decrease because high mass stars are removed by binary formation and the mass distribution finally reaches a steady state in Lagrangian coordinate although the system expands with time. Our simulations, however, show significant differences from the previous studies (Giersz & Heggie 1996; Khalisi et al. 2007) in post-core collapse phase. In Fig. 2.19, mean masses of inner shells continue to increase even after the core collapse. This is because our

models are tidally-limited. Low mass stars escape from the cluster more rapidly than high mass stars as shown in Fig. 2.5. As most of low mass stars escape, mean masses of outer shells increase at the end of evolution.

2.5.4 Angular momentum exchange

Because our N-body model includes two different mass components, we are able to investigate the angular momentum exchange between different mass components. This has not been studied carefully yet and is an important subject to understand the evolution of rotating star clusters. However, it is not easy to analyze the angular momentum transfer with the tidal boundary because total angular momentum of cluster decreases continuously by escaping stars. To distinguish the loss of angular momentum of a cluster between escaping and exchange, we register the positions and velocities of each escaping stars at the moment of escape. Fig. 2.20 shows the time evolution of the total angular momentum for a model with $\omega_0 = 0.6$. Thin lines mean the total angular momentum of stars within the cluster and thick lines mean those of stars including escapers. From the thick solid line, we observe that the total angular momentum including escapers is conserved as expected. Interestingly, the angular momentum of m_2 including escapers decreases while that of m_1 increases. Therefore, we conclude that there is a transfer of angular momentum from m_2 to m_1.

If the exchange of angular momentum is due to the two-body relaxation, we can define the angular momentum exchange rate as follows

$$\xi_{\rm exc} \equiv -\frac{\tau_{\rm rh}(t)}{L_{z,m_2\to m_1}}\frac{dL_{z,m_2\to m_1}}{dt}, \tag{2.10}$$

where $L_{z,m_2\to m_1}$ is the amount of remaining angular momentum expected to be transferred from m_2 to m_1. If the angular momentum transfer rate is a constant, the above equation can be integrated to give,

$$L_{z,m_2\to m_1} = L_{z,m_2\to m_1}(0)e^{-\xi_{\rm exc}t_{\rm norm}} \tag{2.11}$$

when we use a new time unit normalized by half-mass relaxation time $t_{\rm norm} = \int \tau_{\rm rh}(t)^{-1}dt$. This rate can be a good parameter to measure the efficiency of the

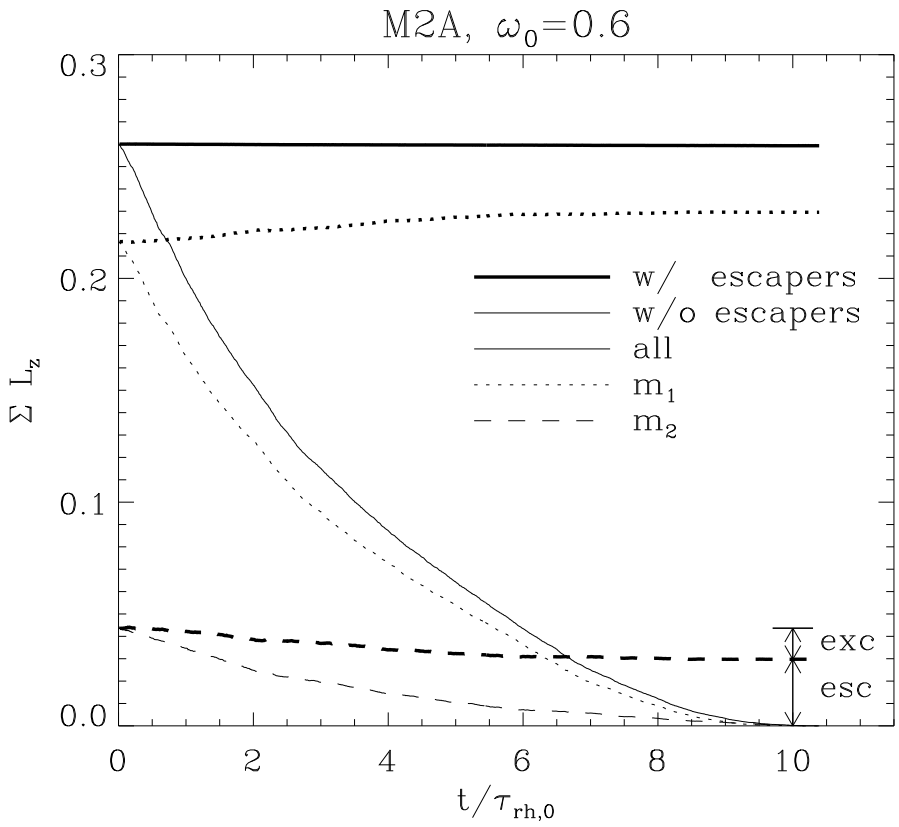

Figure 2.20 Evolution of the angular momentum for the model with $\omega_0 = 0.6$. When we consider the angular momentum of escapers, the total angular momentum is conserved (thick solid line). The total angular momentum of m_1 slightly increases (thick dotted line), while that of m_2 decreases (thick dashed line). This shows the existence of the angular momentum exchange from m_2 to m_1. The words 'esc' and 'exc' mean the degree of the angular momentum loss by escape and exchange, respectively.

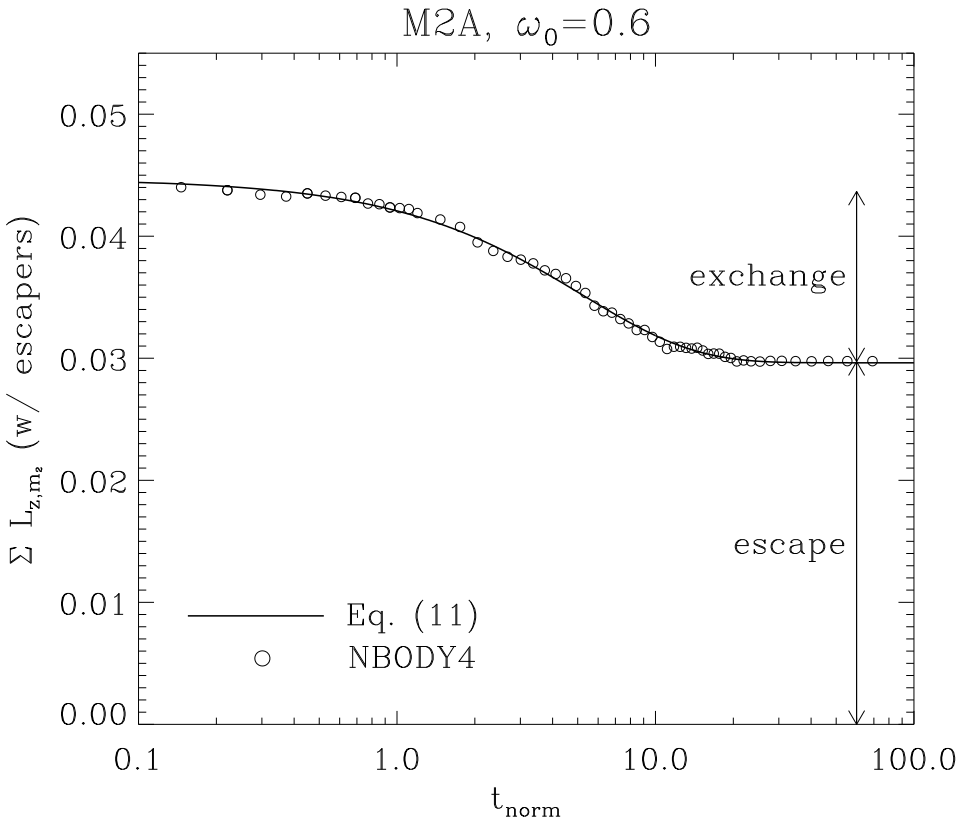

Figure 2.21 Detailed evolution of the angular momentum of m_2 including those of escapers (i.e., thick dashed line in Fig. 2.20) as a function of $t_{\rm norm}$. $t_{\rm norm}$ is a time unit normalized by half-mass relaxation time (see the text). Open circles represent the N-body results. At the end of evolution, one can distinguish the amount of angular momentum loss by exchange and escape. The solid line shows the equation (2.11) with $\xi_{\rm exc}$ in Table 2.5. Note that the line is shifted as much as the amount of angular momentum loss by escape.

angular momentum transfer between different mass components. The angular momentum of clusters goes to 0 when clusters are disrupted. So we divide the loss of angular momentum of m_2 into two contributions: through escaping and through transferring to m_1. We also estimate the fractional angular momentum loss by two different processes. In Fig. 2.21, the detailed evolution of the angular momentum of m_2 including those of escapers is represented by open circles. At the end of evolution, whole amount of angular momentum of m_2 disappears by escape or exchange. The solid line which is from equation (2.11) with suitable value of $\xi_{\rm exc}$ and shifted as much as the amount of angular momentum loss by escape agrees well with the N-body result. Table 2.5 shows the initial total angular momentum of m_2, the fraction of angular momentum loss by escaping and exchanging and the angular momentum exchange rate. Although the angular momentum exchange rate increases with the initial rotation, the fraction of angular momentum loss by exchange decreases. For the model with $\omega_0 = 1.5$, the fraction is less than 10%. Rapidly rotating models have larger angular momentum exchange rate than slowly rotating models, but their lifetimes are very short compared to slowly rotating models. Therefore, these rapidly rotating models do not have enough time to exchange angular momentum from m_2 to m_1.

Table 2.5 Angular momentum loss by escape and exchange for M2A models.

ω_0	$L_{z,0}(m_2)$	escape (%)	exchange (%)	$\xi_{\rm exc}$
(1)	(2)	(3)	(4)	(5)
0.3	0.0283	57.8	42.2	0.17
0.6	0.0448	66.2	33.8	0.19
0.9	0.0555	70.4	29.6	0.23
1.2	0.0571	88.1	11.9	0.34
1.5	0.0635	91.3	8.7	0.71

Note. - (1): Initial rotation parameter. (2): Total angular momentum of high mass stars. (3): Fraction of angular momentum loss by escaping. (4): Fraction of angular momentum loss by transferring to low mass stars. (5): Angular momentum exchange rate.

Chapter 3

Black Hole Binaries in Galactic Nuclei and Gravitational Wave Sources

3.1 Introduction

According to general theory of relativity, the gravity can be expressed as a curvature of space-time. The gravitational wave (GW) is the propagation of ripples of this curvature with speed of light. GW doesn't interact with ordinary matter, so the detection of GW will be a good way to explore the vicinity of neutron stars (NS), black holes (BH), supernovae and active galactic nuclei that are too difficult to observed with electromagnetic (EM) waves. Since Einstein (1916) predicted the existence of gravitational radiation (GR), search for GW has been done by many groups. However, there are only *indirect* evidences so far for the existence of GWs. From 30 years observations, Weisberg & Taylor (2005) found that the binary pulsar PSR 1913+16, discovered by Hulse & Taylor (1974), exhibited the decrease of the orbital period and the amount of decrease exactly coincides with the prediction of general relativity.

In order to detect GWs *directly*, it is necessary to measure the distortion of space-time as GWs pass through. The first practical instruments, so-called bar de-

tectors, were constructed by Weber (1960), in order to measure the vibration of the metal bar due to the GWs. However, it became clear that the bar detectors are not sensitive enough to detect astrophysical signals. More sensitive detectors based on laser interferometry have been constructed subsequently (e.g., LIGO, Virgo, GEO 600 and TAMA 300). If GW passes through the interferometer, the wave can be detected by measuring the variation of the relative arm lengths as a function of time. The strain amplitudes of astronomical GWs are typically very small, $h \lesssim 10^{-22}$. The sensitivity of ground-based GW detectors depends on the length of baselines and is limited by various noises: shot, seismic, thermal noises. For the initial LIGO and Virgo, the theoretical sensitivity is comparable to $h \sim 10^{-22}$ at frequency around $f \sim 100$ Hz. It is expected that the sensitivity will be enhanced by a factor of 10 for second generation GW detectors such as advanced LIGO and Virgo.

There are several astronomical GW sources in the universe: core-collapse supernovae (e.g., Mueller & Janka 1997; Yakunin et al. 2010), spinning neutron stars (e.g., Andersson et al. 2011), compact binary coalescences (e.g., Kalogera et al. 2004), supermassive black holes (SMBH) (e.g., binary SMBH merger, Berentzen et al. 2009) (extreme mass ratio inspirals, EMRI, Hopman & Alexander 2006; Merritt et al. 2011) and cosmological density fluctuations (e.g., Ananda et al. 2007). Among those, the compact binary coalescence (CBC) involving NS and stellar mass BH is the primary targets for the first GW detection. Only seven NS-NS binary pulsars, however, have been discovered in our Galaxy including PSR 1913+16, and a half of them will merge within a Hubble time (O'Shaughnessy et al. 2005). These NS-NS binaries are known to be evolved from primordial binaries. Compact binaries can also be formed dynamically in stellar systems: dynamical three-body processes and dissipative two-body processes by tidal effect (Lee & Ostriker 1986) and GW emission (hereafter GR capture, Hansen 1972; Quinlan & Shapiro 1987).

Stellar systems such as globular clusters (GC) and nuclear star clusters (NC) at the galactic nuclei provide good environments for the formation of compact binaries through the massive star formation and stellar encounters. In GCs, when the core is dense enough, compact binaries can be formed by three-body encounters. These binaries become more compact through close encounters with other stars and is

eventually kicked out from GCs when their orbital separations become very small. Some of the ejected binaries merge within a Hubble time in galactic field (Downing et al. 2011; Bae et al. 2013). On the other hand, binary formation by three-body processes is suppressed by the existence of massive BH (MBH) in galactic nuclei (Baumgardt et al. 2004a). Instead, coalescences of primordial compact binaries can be driven by the orbit coupling with central MBH, as known as the Kozai effect (Kozai 1962), and occur within Hubble time (Antonini & Perets 2012). Compact binaries, especially BH-BH binaries, also can be formed by GR capture in NCs due to the high stellar density and velocity dispersion at the vicinity of MBH (O'Leary et al. 2009). These captured compact binaries usually have large eccentricities with small pericenter distance, and thus, they will merge within a few orbits, while keeping the high eccentricity until the moment of merger.

Numerous authors made estimates of the detection rates of GWs from CBCs with present- and planned- GW detectors using various methods: population synthesis models for primordial binaries (Kalogera et al. 2004; Belczynski et al. 2007), Monte-Carlo simulations for GCs (Downing et al. 2011) and Fokker-Planck simulations for NCs (O'Leary et al. 2009), and estimated that few tens of events will be detected by new generation GW detectors (see, Abadie et al. 2010). However, most of these studies are based on simplified models and assumptions on the evolution of the stellar systems and the binaries. Realistic models are difficult because of lack of observational data, as well as difficulties in accurately modeling of the systems with the large number of stars. Direct N-body approach is difficult for realistic systems, and therefore, statistical approaches such as Fokker-Planck models and Monte-Carlo simulations have been used, so far. However, statistical methods are restricted to certain simplified configurations. In this study, we focus on the binary formation of BHs by GR capture in NCs by using direct N-body simulations. Although, we cannot use realistic number of stars, we try to deduce important information regarding the binary formation and evolution based on scaled-down and simplified version of N-body simulations.

This chapter is organized as follows. In §§3.2 and 3.3, we introduce the numerical method and the model for star clusters in galactic nuclei with a central MBH. The

dynamical evolution of our model is presented in §3.4. In §3.5, we describe binary formation in NCs and estimate the merger rate per galaxy. In §3.6, the expected detection rate for new generation GW detectors is estimated. To give the interpretation for binary coalescences and their waveforms, we implement post-Newtonian approximations on the two-body motions. An example waveform of a binary BH coalescence in Milky-Way-like galaxies is provided in §3.6.2.

3.2 Generation of initial models

NCs are very dense star clusters located at the nuclei of galaxies, regardless of the type (e.g., Carollo et al. 1997; Böker et al. 2002; Côté et al. 2006). Their typical mass is $10^{6-7} M_{\odot}$ (Walcher et al. 2005), the size of NCs is comparable to that of galactic GCs (Böker et al. 2004; Côté et al. 2006), thus the density of NCs is much higher than GCs. It is also well known that most of galaxies host MBHs at the center (e.g., Kormendy & Richstone 1995; Ferrarese & Ford 2005). The coexistence and correlation of MBHs and NCs at the central region of galaxies have been studied by Graham & Spitler (2009).

Observational (e.g., Schödel et al. 2009) and theoretical (e.g., Bahcall & Wolf 1976) studies for star clusters with the central MBH showed that the density and velocity dispersion diverge at the vicinity of the MBH. The modeling of stellar systems with a central black hole has been done by numerous authors (Young 1980; Goodman & Binney 1984; Quinlan et al. 1995; Sigurdsson et al. 1995). In order to generate N-body realizations for NCs with MBH, we adopt 'adiabatic growth' of the MBH as suggested by the previous studies. The MBH is assumed to grow with time following Sigurdsson et al. (1995)

$$M_{\rm MBH}(t) = \begin{cases} M_{\rm MBH}\left[3(t/t_{\rm MBH})^2 - 2(t/t_{\rm MBH})^3\right], & t \le t_{\rm MBH} \\ M_{\rm MBH}, & t > t_{\rm MBH} \end{cases} \tag{3.1}$$

where $M_{\rm MBH}$ and $t_{\rm MBH}$ are the final mass of MBH and the black hole growth time scale, respectively. During the growth of the MBH, the stellar system is adjusted against the potential of the MBH. The MBH is fully grown after $t_{\rm MBH}$, and the

gravitational potential of the MBH is assumed to follow that of the Plummer model

$$\phi_{\rm MBH} = -\frac{GM_{\rm MBH}}{\sqrt{r^2+\varepsilon_{\rm MBH}^2}}, \tag{3.2}$$

where $\varepsilon_{\rm MBH}$ is the softening parameter for avoiding unexpected effect at the singularity. Holley-Bockelmann et al. (2002) noted that $t_{\rm MBH}$ should be larger than the half-mass dynamical time to ensure the adiabatic growth of the MBH. While they used the Hernquist model as the initial density distribution, we used Plummer model with half-mass dynamical time $t_{\rm dyn,1/2} \sim 2.46$ for standard N-body scaling (i.e., $G = M_{\rm cl} = -4E = 1$).

According to recent observations (e.g., Schödel et al. 2009) of the center of the Milky Way (i.e., the vicinity of Sgr A*), the velocity dispersion of stars at about 1 parsec scale is nearly flat. This implies that the NC is almost in the isothermal state. However, it is not possible for the isolated stellar systems to become fully isothermal. Yoon et al. (2011) have investigated a self-gravitating stellar systems embedded in an external potential well. They considered a Plummer external potential,

$$\phi_{\rm pl} = -\frac{GM_{\rm pl}}{\sqrt{a_{\rm pl}^2+r^2}}, \tag{3.3}$$

where $M_{\rm pl}$ and $a_{\rm pl}$ are the mass and scale length of the Plummer potential, respectively. When the external potential well is deep enough, the velocity dispersion of the embedded stellar system becomes isothermal and there is a quasi-equilibrium solution of a potential-density pair for the isothermal stellar system.

In the case of NCs, the surrounding bulge can provide such a potential well. The bulge is one of galactic building blocks, extending over few kpc scales. NC and bulge are independent components of galaxies with different surface brightness profiles (e.g., Balcells et al. 2003). In the Milky way, the effective radius (i.e., half-light radius) of the bulge is about 0.1 kpc, and the mass is estimated to be roughly $10^{10} M_\odot$. According to a dynamical model of Galactic bulge suggested by Kent (1992), the kinematics of the bulge is affected by the MBH, Sgr A$_*$, at inner parsec scale, and the velocity dispersion is nearly flat from 1 to 10 parsec and increases gradually at the large radii due to the effect of galactic rotation. Although bulges

are thought to be oblate spheroids or triaxial, we consider the bulge as a sphere in this study for the simplicity. This may not cause a serious effects on the dynamics of the nuclear cluster we are considering since the role of the bulge in our model is to confine the nuclear cluster within a few parsec.

3.3 Computational methods

In this study, we used the GPU accelerated version of NBODY6 (Nitadori & Aarseth 2012). NBODY6 code is one of the several versions of direct N-body code which has been developed by S. J. Aarseth for many years. This code includes many efficient and accurate algorithms such as the Hermite integrator, the individual and block time steps, the Ahmad-Cohen neighbor scheme, the Kustaaheimo-Stiefel (KS) and chain regularization scheme (Aarseth 1999). Recently, by using numerous stream processors of GPU devices, calculations of gravitational interactions among stars have been significantly accelerated through massive parallelism. All the calculations in NBODY6 code use dimensionless time, length and mass units. From given unit of length $\bar{r}$ in parsec and mean stellar mass $\bar{M}$ in $M_{\odot}$, the physical unit of velocity and time can be expressed as (Aarseth 2010)

$$\text{velocity} : 6.557 \times 10^{-2}\left(\frac{N\bar{M}}{\bar{r}}\right)^{1/2}\text{km/s}, \qquad \text{time} : 14.94\left(\frac{\bar{r}^3}{N\bar{M}}\right)^{1/2}\text{Myr}, \tag{3.4}$$

where N is total number of stars.

As we mentioned above, the external potential is composed of two parts,

$$\phi_{\text{ext}} = \phi_{\text{MBH}} + \phi_{\text{pl}}, \tag{3.5}$$

where ϕ_{MBH} is the Keplerian potential due to the central MBH. Since the Plummer external potential has already been implemented in NBODY6 code, we added the potential of MBH in the code in a similar manner with the Plummer potential. Table 3.1 shows model parameters of our simulations. Although galactic nuclei contain $\sim 10^6$ stars in a cubic parsec, it is hard to treat such a large number of particles for NBODY6 code with a single GPU machine. We, therefore, used different number of particles from 10,000 to 100,000 in order to build a scaling relation. We aslo made

several simulations with different random seeds in order to reduce the statistical errors. The masses of MBH are chosen to be 0.1 and 0.2 in our units of 1 for the entire mass of cluster stars $M_{\rm cl}$ (but excluding the mass of the Plummer potential). Because these masses are relatively larger than those of Holley-Bockelmann et al. (2002), we also used longer black hole growth time scale $t_{\rm MBH} = 50$. The softening parameter of the MBH is fixed to 10^{-4}, which is much smaller than the radius of influence of the MBH (c.f., $r_{\rm inf} \equiv M_{\rm MBH}/\sigma_*^2 \sim 0.1$ for $M_{\rm MBH} = 0.1$). We assumed that all stars have same masses (i.e., $m = 1/N$) of stellar mass BHs with the mass of $10M_{\odot}$. Thus, the total mass of the cluster in physical unit becomes $M_{\rm tot} = N \cdot 10M_{\odot}$. It is well known that there is a correlation between the mass of MBHs and the kinematics of bulges. Recently, McConnell & Ma (2013) updated the $M_{\rm MBH} - M_{\rm bulge}$ relation and found that the mass of MBH is roughly 0.2% of the bulge mass for $10^7 < M_{\rm MBH}/M_{\odot} < 10^{10}$. For the external potential of a bulge, we fixed the mass and scale length of the Plummer potential to 100 and 5, respectively, which corresponds to $M_{\rm MBH}/M_{\rm bulge} = 0.001$ and 0.002 for our models. Under this potential well, the embedded stellar system is expected to become isothermal in a few half-mass relaxation time (Yoon et al. 2011). The Model 0 without the external Plummer potential well is also carried out for comparison.

3.4 Dynamical evolution of star clusters

3.4.1 Cluster expansion

In order to investigate the effect of the MBH and the surrounding bulge, the dynamical evolution of the star cluster is presented in this section. Here, we focus on the Model 4 with $N = 100,000$ and $M_{\rm MBH}/M_{\rm cl} = 0.2$. Fig. 3.1 shows the time evolution of Lagrangian radii including 1, 5, 10, 20, 50 and 75 % of total cluster mass. Before $T = t_{\rm MBH} = 50$, all Lagrangian radii decrease with growing mass of the central MBH to adjust the strong potential of the MBH. After $T = t_{\rm MBH}$, Lagrangian radii increase gradually as reported in previous studies (e.g., Baumgardt et al. 2004a), because of the strong gravitational field of the MBH. The basic mechanism of the expansion is similar to that of post core collapse expansion of star clusters. However,

Table 3.1 Initial parameters for all models.

Model	$N_{\rm cl}$	$N_{\rm run}$	$M_{\rm MBH}/M_{\rm cl}$	$M_{\rm MBH}/m_*$	$t_{\rm MBH}$	$\varepsilon_{\rm MBH}$	$M_{\rm pl}$	$a_{\rm pl}$
	(1)	(2)	(3)	(4)	(5)	(6)	(7)	(8)
0	100,000	1	0.2	10,000	50	10^{-4}	-	-
1	10,000	10	0.2	2,000				
2	20,000	5	0.2	4,000				
3	50,000	2	0.2	10,000				
4	100,000	1	0.2	20,000	50	10^{-4}	100	5
5	20,000	5	0.1	2,000				
6	50,000	2	0.1	5,000				
7	100,000	1	0.1	10,000				

Note. - (1): Number of stars in the nuclear star cluster. (2): Number of simulations with different initial random seeds. (3): MBH mass compared to the total mass of cluster. (4) Mass ratio of MBH to the stellar mass. (5): MBH growth time scale. (6): Softening parameter of MBH potential. (7): Mass of external Plummer potential. (8): Scale length of external Plummer potential.

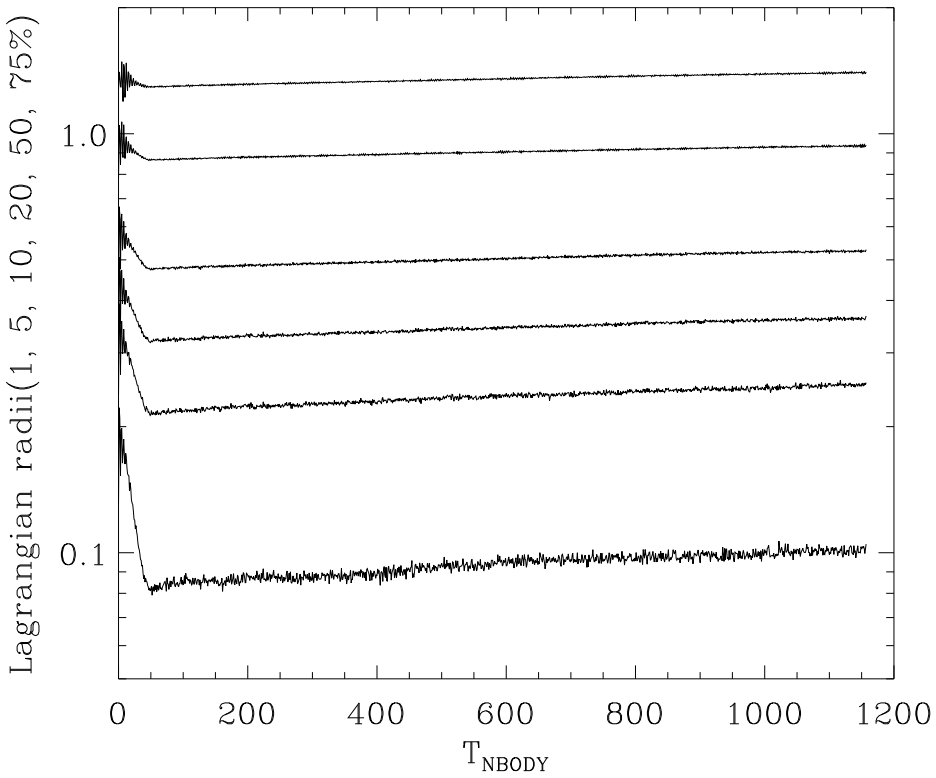

Figure 3.1 Time evolution of Lagrangian radii for the star cluster with a growing central MBH and an external Plummer potential well. By the growth of MBH, the Lagrangian radii decrease with time until $T = t_{\rm MBH} = 50$. After full growth of the MBH, the cluster expands due to the heating from the MBH and stars in the cusp.

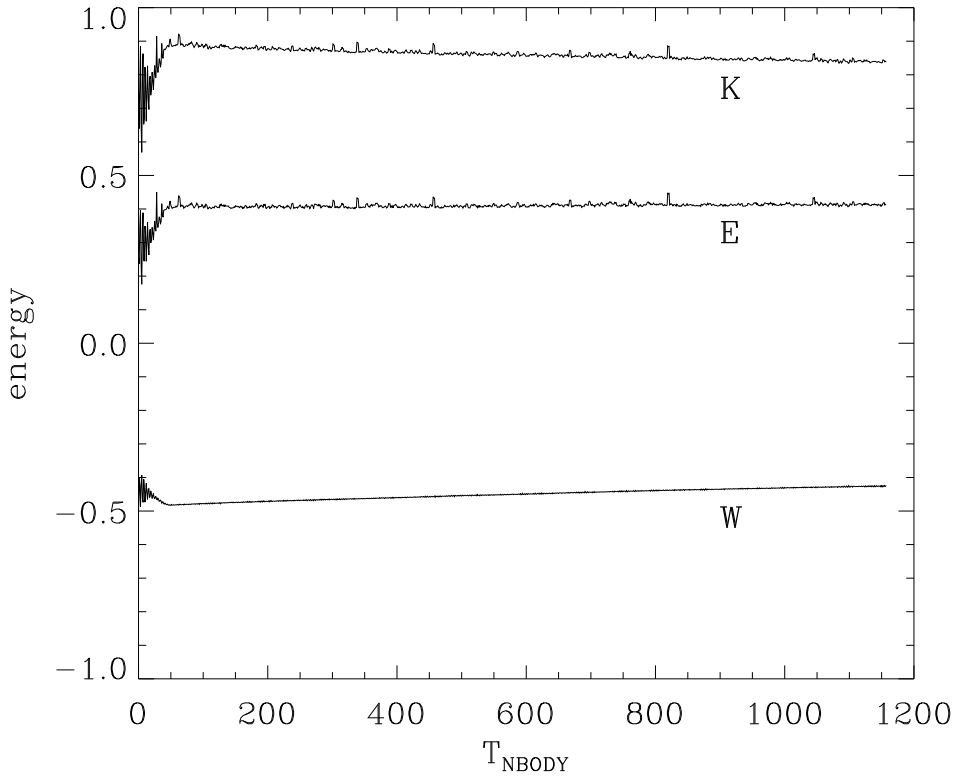

Figure 3.2 Time evolution of energies for stellar particle only. To be virialized against the external potential, the kinetic energy becomes much larger than the isolated systems. The kinetic energy decreases with time because of the cluster expansion while the total energy is nearly conserved.

there is no gravothermal oscillation because of the steady heating by MBH (Heggie & Hut 2003; Baumgardt et al. 2004a). With the MBH, kinetic energy can be generated by stars in the cusp (Shapiro 1977). The MBH and the innermost star can behave like hard binaries in the core of star clusters. Encountering other single stars in the cusp, they tend to be bounded stronger and convert their internal energy to the kinetic energies of stars in the cusp. The kinetic energies are transferred to the whole cluster via relaxation.

While the kinetic, potential and total energies of an isolated self gravitating system are 1/4, -1/2 and -1/4 in NBODY units, respectively, the system embedded in a potential well has lager kinetic energy than the isolated system through the virialization (Yoon et al. 2011). Also, when the kinetic energy is even lager than the magnitude of the potential energy (i.e., the total energy becomes positive.), the system will not reach the core collapse. Fig. 3.2 shows the time evolution of the energies. Our models are designed to have positive total energy. Initially, the kinetic energy, potential energy of self-gravity and total energy are 0.7, -0.45 and 0.25, respectively. However, as the black hole grows, the potential energy decreases because the cluster becomes more centrally concentrated as shown in Fig. 3.1 while the kinetic energy increases in response. At $T = t_{\rm MBH}$, the energies become -0.5 (potential), 0.9 (kinetic) and 0.4 (total), respectively. The potential energy increases after $T = t_{\rm MBH}$ due to the cluster expansion although we designed a quasi-equilibrium model by using the external Plummer potential.

3.4.2 Radial profiles

In Fig. 3.3, we show the density profile of the the star cluster of the Model 4 for $t = 0$ and $1000T_{\rm NBODY}$. We see in Figs. 3.1 and 3.2 that the cluster is not in equilibrium but expanding. However, as reported in Baumgardt et al. (2004a), the equilibrium profile is expected to be established from inner to outer regions after a few local half-mass relaxation times (c.f., $\tau_{rh,0} \sim 1600T_{\rm NBODY}$ for Model 4). The radius of influence $r_{\rm inf}$ is marked as the downward arrow. The slope of density cusp at $r < r_{\rm inf}$ is not exactly -1.75, the Bahcall-Wolf cusp for equal-mass systems, but about -1.6. There is an upturn of the density near $r = 5$. This radius is the scale length of the external

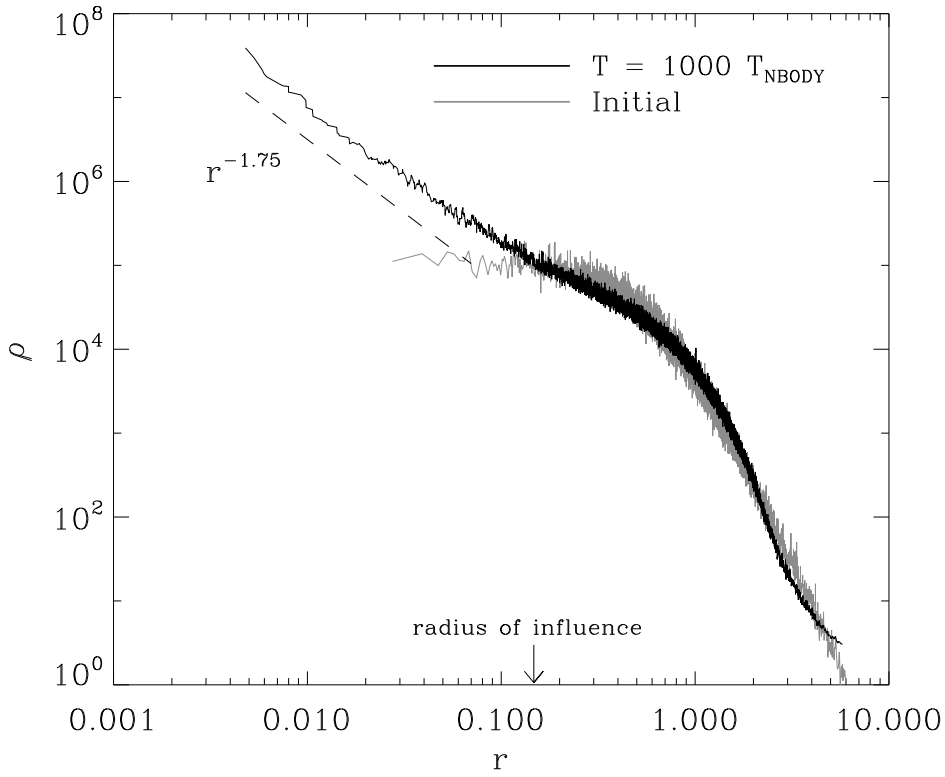

Figure 3.3 Density profiles at $T = 0$ and $T = 1000T_{\rm NBODY}$. Grey line shows the initial condition. Because of the existence of MBH, the stellar cusp, so-called Bahcall-Wolf cusp, is formed inside the radius of influence. Our cusp has $r^{-1.6}$ which is less steep than the theoretical expectation.

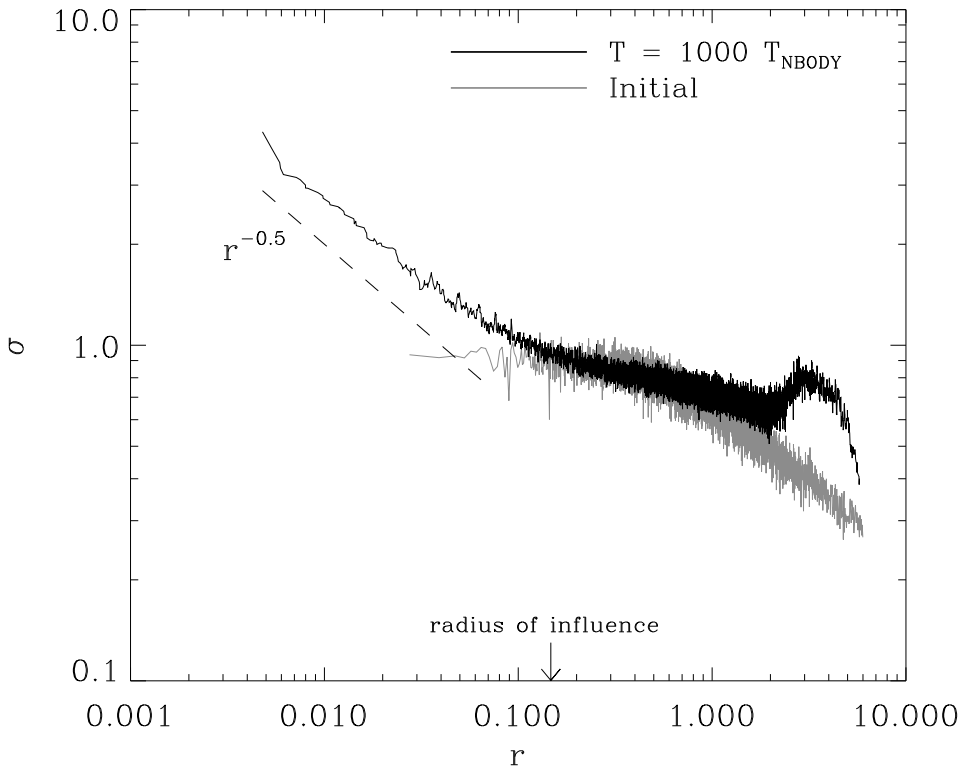

Figure 3.4 Velocity dispersion profiles at two epochs: $T = 0$ and 1000. The existence of MBH makes stars within radius of influence follow the Keplerian profile. For the outer parts, the velocity dispersion is flatter than the initial condition due to the external potential well.

Plummer potential, so stars have piled up at this radius against the external force from the potential.

The radial profile of velocity dispersion is presented in Fig. 3.4. The black line shows the profile at $T = 1000$, and the grey line is the initial one. For the outer part in Fig. 3.4, the velocity dispersion is not completely flat unlike the observations. When a star is ejected from the vicinity of the MBH, the star has very large kinetic energy and transfers its kinetic energy to other stars through the interactions. Nevertheless, the velocity dispersion is flatter than the initial dispersion. There is a bump of velocity dispersion at $r \sim 5$, the scale length of the external Plummer potential. This is because the ejected stars from the center are decelerated against the external potential. When the MBH exists, stars inside $r_{\rm inf}$ are strongly affected by the MBH, and their velocity dispersion follows the Keplerian profile (i.e., $\sigma(r) \sim r^{-0.5}$). One can see the slope of the velocity dispersion profile at $r < r_{\rm inf}$. However, the slope is a little shallower than the expectation as similar to the density profile in Fig. 3.3. The most plausible explanation for this effect is the wandering of the MBH. A MBH in a stellar system can move randomly, like a Brownian motion, by the interaction with stars which are bounded and un-bounded to the potential of the MBH. In addition, the MBH and the innermost star can play a role as binaries in the core-collapsed star cluster. They kick a star interacting with them with high kinetic energy, and this causes the recoil motion of the MBH. Lin & Tremaine (1980) investigated the motion of the MBH in the stellar system such as a globular cluster. They concluded that the interaction with unbound stars is the most important effect causing the motion of the MBH. Bahcall & Wolf (1976) estimated the uncertainty of the position of the MBH by the wandering of the MBH as

$$r_{\rm wand} \approx 0.92 r_{\rm c} \sqrt{m_*/M_{\rm MBH}}, \tag{3.6}$$

where $r_{\rm c}$ is the core radius. It is difficult to define the wandering radius in our simulations because there is not a well-defined core. Nevertheless, from the simulations with different number of stars, we confirmed the number dependence of the wandering radius. Fig 3.5 shows the wandering radius estimated by the radial distance of the MBH fixed at the origin to the center of mass of the stellar particles. The solid lines are the wandering radius in the simulations for the simulations with different

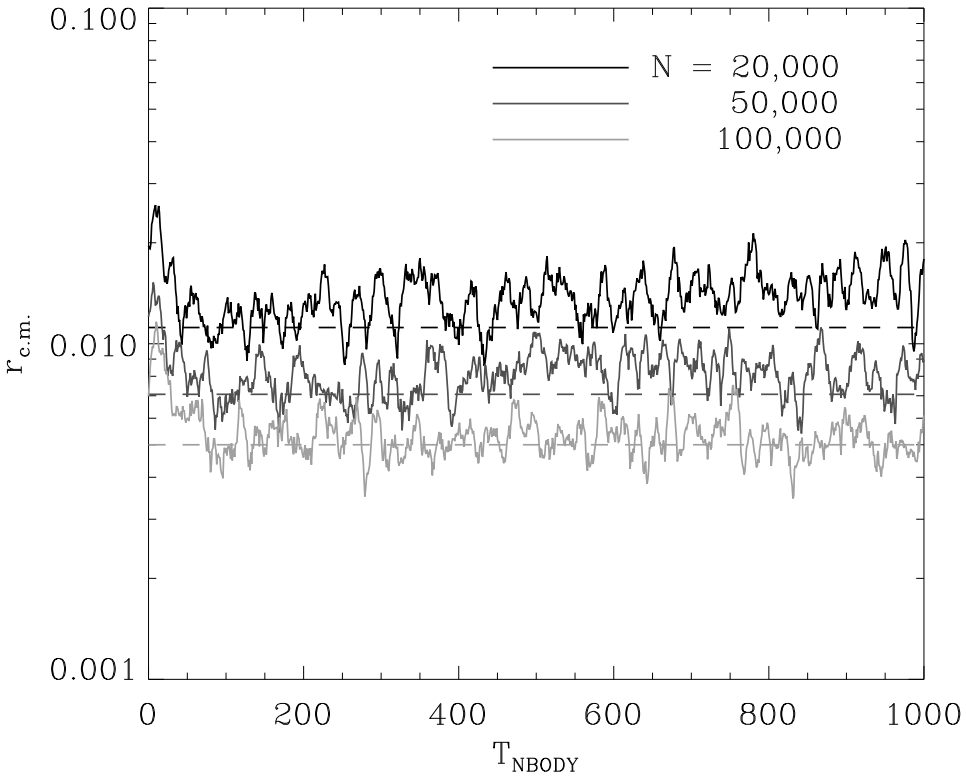

Figure 3.5 Separation between the MBH and the center of mass of stars as a function of time for simulations with different N. Contrasts show different numbers of stars. With less number of stars, the MBH wanders more. Dashed lines represent the expected wondering radius based on the equation (3.6) when normalized by the average value of N=100,000.

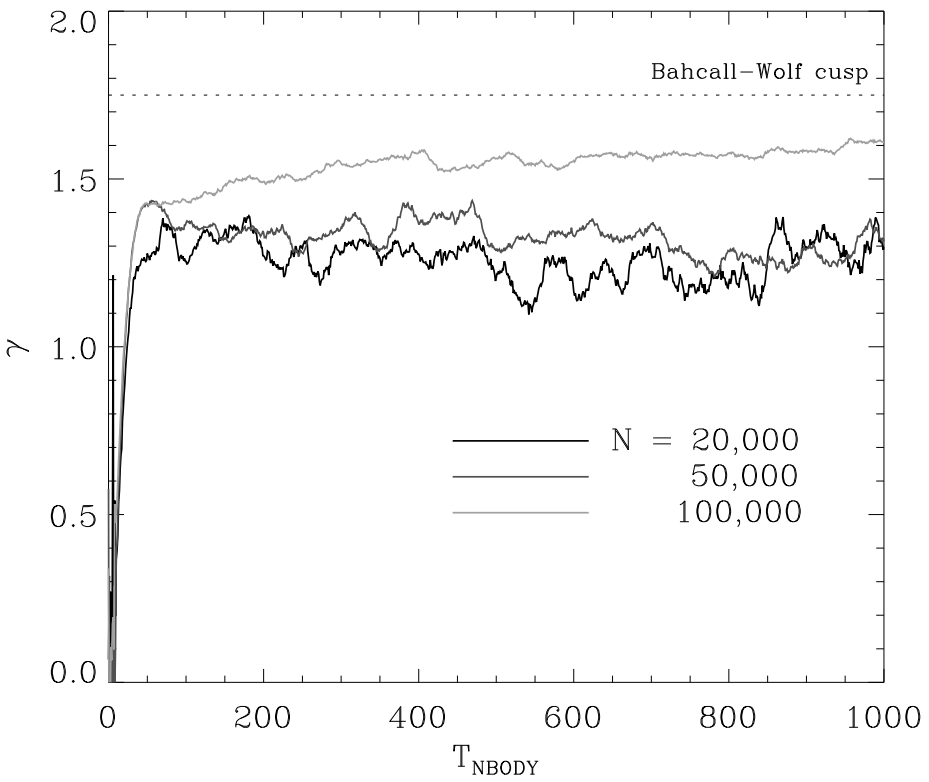

Figure 3.6 Time evolution of the slope of stellar cusp within the radius of influence. Different contrasts show different numbers of stars. At the end of MBH growth, the slope is much less than 1.75, Bahcall-Wolf cusp. For larger number of stars, however, the slope increases with time gradually while those for models with smaller number of stars do not get close to the Bahcall-Wolf cusp.

number of stars ranging from 20,000 (top) to 100,000 (bottom) with the MBH mass of 0.2. As the number of stars becomes larger, the wandering radius becomes smaller. The dashed lines are the values obtained with the equation (3.6), normalized by the mean wandering radius of the model with $N = 100,000$. Thus the wondering radius follows the scaling relation of the equation (3.6) with N very well. The time evolution of the slope of the central stellar cusp γ is shown in Fig. 3.6. Different contrasts mean different number of stars. During the growth of the MBH, the slope increases with time. When the growth of the MBH is completed, the slope is still not same as the Bahcall-Wolf cusp. For larger N, the slope increases with time slowly while those for models with smaller number of stars do not get close to the Bahcall-Wolf cusp. This may be related to the wandering of the MBH and will affect the merger rate of stellar mass BHs near the MBH which is going to be discussed in the next sections.

3.4.3 Velocity anisotropy

It is well known that the radial anisotropy in the velocity dispersion increases at the outer part of isolated stellar systems as a result of two-body relaxation (Giersz & Heggie 1996; Spitzer 1987). The anisotropy parameter can be defined by (Binney & Tremaine 2008)

$$\beta \equiv 1 - \frac{\sigma_t^2}{2\sigma_r^2}, \tag{3.7}$$

where σ_t and σ_t are the tangential and radial velocity dispersions, respectively. This anisotropy parameter becomes $-\infty$ for purely circular orbits and $+1$ for purely radial orbits. Also, in a tidal field, the radial anisotropy decreases during post core-collapse expansion due to the loss of radial orbits (Takahashi et al. 1997). However, in the case of stellar systems with a growing central massive object, the tangential anisotropy is developed (i.e., $\beta < 0$, Young 1980; Goodman & Binney 1984; Quinlan et al. 1995; Sigurdsson et al. 1995; Holley-Bockelmann et al. 2002). Quinlan et al. (1995) have revealed that the aspect of anisotropy is affected by the initial models. For models with a core such as isothermal sphere and isochrone model, the velocity distribution becomes isotropic in the limit $r \to 0$ (Young 1980; Quinlan et al. 1995). On the other hand, for 'two-power' models for galaxies like Dehnen's models (Dehnen 1993),

the velocity distribution is still tangentially biased at $r \to 0$ (Quinlan et al. 1995; Sigurdsson et al. 1995; Holley-Bockelmann et al. 2002). The tangential anisotropy becomes the largest at $r \approx r_{\rm inf}$, and the velocity distribution becomes isotropic at $r \gg r_{\rm inf}$ again (see Figs. 2-5 of Quinlan et al. 1995).

The radial and tangential velocity dispersions and the velocity anisotropy parameter after the growth of MBH are shown in Fig. 3.7 for the Model 0 without the external Plummer potential and Fig 3.8 for the Model 4 with the potential, respectively. For the Model 0, the velocity dispersions decrease rapidly with radius unlike those of the model with the potential well. Although we use the Plummer model as the initial model, the anisotropy parameter is likely to be similar to that of the isochrone model as shown in Quinlan et al. (1995). However, the maximum anisotropy is located at the larger radius than $r_{\rm inf}$. On the other hand, for the Model 4, the radial velocity dispersion is enhanced due to the radial acceleration from the external potential as mentioned in the previous section. Therefore, the anisotropy parameter becomes almost 1 at $r \approx a_{\rm pl}$. For the inner region, the velocity dispersion is tangentially biased as the same as isolated models.

3.5 Black hole binaries

3.5.1 Close encounters and GR capture

In order to estimate the merger and detection rates of BH-BH binary coalescences, we need to know binary formation rates as well as the orbital parameter distribution just after the capture. There are several binary formation mechanisms known: primordial, dynamical three-body process, dissipative two-body processes. Antonini & Perets (2012) have discussed how primordial BH-BH binaries can evolve to GW sources in galactic nuclei by the secular Kozai effect and estimated the merger fraction. In addition, previous studies (e.g., Baumgardt et al. 2004a) noted that binary formation by three-body process is suppressed by the strong gravitational field at the vicinity of MBH. There are two of dissipative processes for two-body encounters, tidal force and GR. The tidal interaction is not our interest because this process is only valid for objects with finite sizes such as main-sequence (MS) or giant stars.

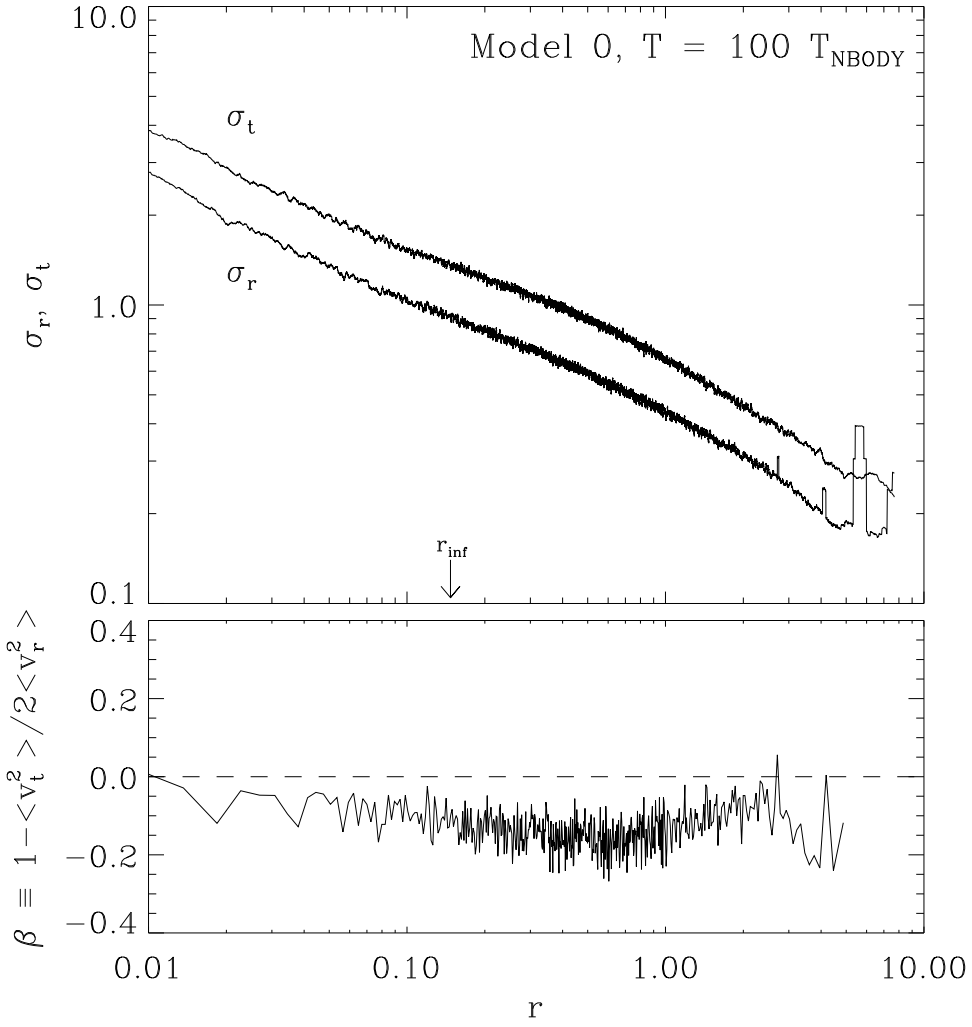

Figure 3.7 Profiles of Radial and tangential velocity dispersion (upper) and the anisotropy parameter (lower) for Model 0 without the external Plummer potential. The velocity distribution is tangentially biased, and the profile is similar to that of the isochrone model in Quinlan et al. (1995) except for the position of maximum anisotropy.

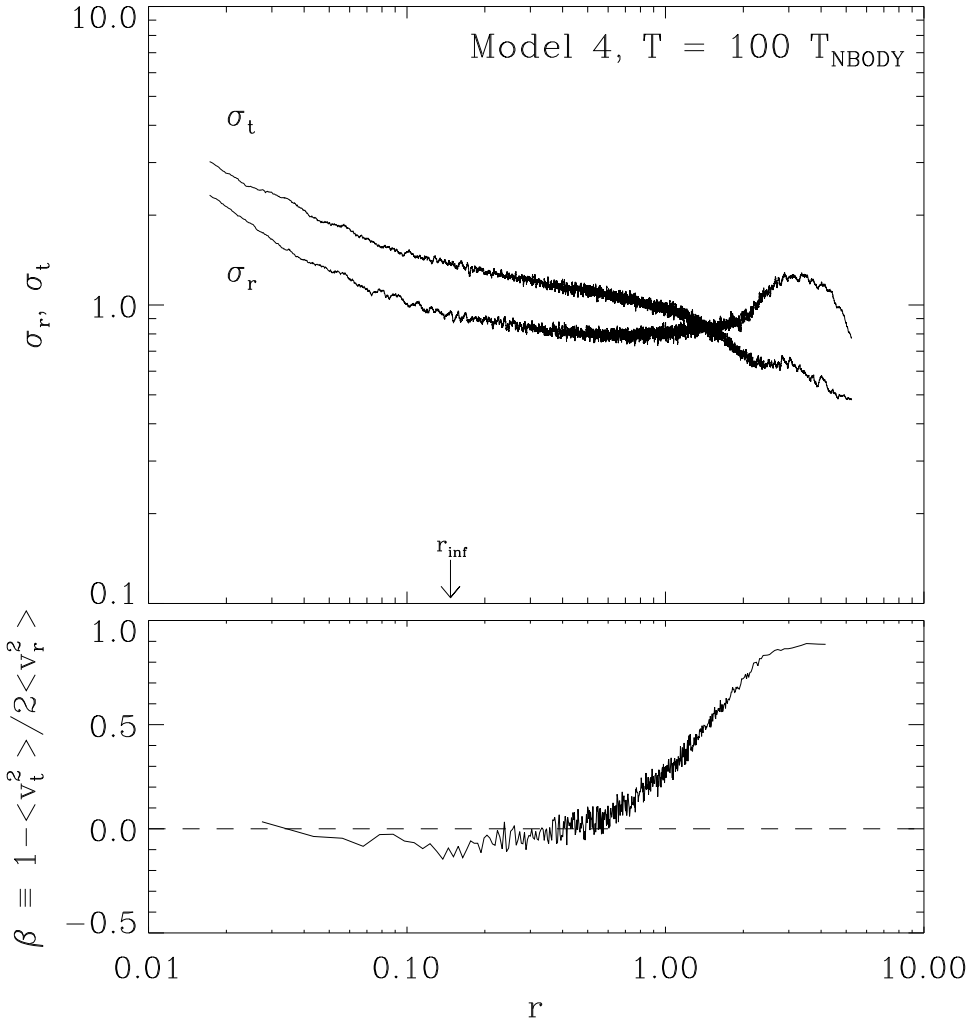

Figure 3.8 Profiles of Radial and tangential velocity dispersion (upper) and the anisotropy parameter (lower) for Model 4 with the external Plummer potential. For the inner region, the velocity distribution is similar to that of isolated models. However, the tangential anisotropy is driven by the external potential well at the outer region.

The energy loss and changes of orbits by GW for binary systems were first studied by Peters & Mathews (1963) based on the post-Newtonian (PN) approximation. Later, Hansen (1972) extended the study of Peters & Mathews (1963) to the hyperbolic encounters. With given masses m_1, m_2, a semi-major axis a (defined as $a = Gm_1m_2/2E_0$ where E_0 is the initial orbital energy) and an eccentricity e, the energy and orbital angular momentum losses by GR are given by

$$\begin{aligned}\Delta E &= -\frac{2}{15}\frac{G^{7/2}}{c^5}\frac{m_1^2 m_2^2 (m_1+m_2)^{1/2}}{a^{7/2}(e^2-1)^{7/2}} \\ &\quad \times\left[(\pi-\theta_0)(96+292e^2+37e^4)+\frac{1}{3}e\sin\theta_0(602+457e^2)\right], \qquad (3.8)\\ \Delta L_z &= -\frac{8}{5}\frac{G^3}{c^5}\frac{m_1^2 m_2^2}{a^2(e^2-1)^2}\left[(\pi-\theta_0)(8+7e^2)+e\sin\theta_0(13+e^2)\right], \qquad (3.9)\end{aligned}$$

where G, c and θ_0 are gravitational constant, speed of light and the incidence angle at infinity defined as $\theta_0 = \cos^{-1}(1/e)$, respectively. Two encountering but unbound stars, therefore, become a binary if the energy loss by GR is larger than the orbital energy E_0. From equations (3.8) and (3.9), one can obtain the semi-major axis and the eccentricity of the captured binary as

$$a' = -\frac{Gm_1m_2}{2(E_0+\Delta E)} \quad \text{and} \quad e' = \sqrt{1-\frac{(m_1+m_2)(L_{z,0}+\Delta L_z)}{Gm_1^2m_2^2a'}}, \qquad (3.10)$$

where the subscript 0 indicates the initial value.

Many previous studies have discussed the GR captures of compact stars in dense stellar systems (e.g., Quinlan & Shapiro 1987, 1989; O'Leary et al. 2009). The starting point is the cross section for GR capture. Quinlan & Shapiro (1987) deduced the capture cross section under the parabolic approximation. This approximation is valid because trajectories of the stars near the pericenter, where most of the GWs are radiated, are almost identical to parabolic with the same pericenter distance. The equation (3.8) is rewritten with parabolic approximation as

$$\Delta E = -\frac{85\pi}{12\sqrt{2}}\frac{G^{7/2}}{c^5}\frac{m_1^2m_2^2(m_1+m_2)^{1/2}}{r_{\rm p}^{7/2}}, \qquad (3.11)$$

where $r_{\rm p}$ is the pericenter distance. Again, the GR capture will happen when the energy loss is lager than the orbital energy. By the requirement of $|\Delta E| > m_1m_2v_\infty^2/2(m_1+$

m_2), Quinlan & Shapiro (1989) obtained the maximum pericenter distance for GR capture:

$$r_{\rm p,max} = \left[\frac{85\pi\sqrt{2}}{12}\frac{G^{7/2}}{c^5}\frac{m_1 m_2 (m_1+m_2)^{3/2}}{v_\infty^2}\right]^{2/7} \tag{3.12}$$

where v_∞ is the relative velocity at infinity. Therefore, the capture cross section is given as

$$\Sigma_{\rm cap} = \pi r_{\rm p,max}^2\left[1+\frac{2G(m_1+m_2)}{r_{\rm p,max}v_\infty^2}\right] \simeq 17\frac{G^2 m_1 m_2 \eta^{-5/7}}{c^{10/7}v_\infty^{18/7}} \tag{3.13}$$

where η is the symmetric mass ratio defined as $\eta \equiv m_1 m_2/(m_1+m_2)^2$. We assumed that gravitational focusing is dominant compared to the geometrical cross section for the last equality in the above equation.

Here, we are going to introduce a statistical interpretation of GR captures to understand the situations and predict the BH-BH binary coalescences in realistic regime. We can assume that the motions of stars follow the one-dimensional normal distribution with a given velocity dispersion σ. From the equation (3.13), the distribution of the pericenter distance of encountering stars also becomes uniform (i.e., $dS = d(\pi b^2) \simeq 2\pi G(m_1+m_2)v_\infty^{-2}\cdot dr_{\rm p}$) if the gravitational focusing dominates. Therefore, for unbound close encounters that lead to the formation of binaries by GR, $r_{\rm p}/r_{\rm p,max}$ follows uniform distribution in the range [0, 1]. Under the parabolic approximation, the semi-major axis and the eccentricity can be rewritten with σ and $r_{\rm p}/r_{\rm p,max}$ from the equations (3.11) and (3.12) as

$$a = \frac{GM}{2\sigma^2} \approx 1.58{\rm AU}\left(\frac{M}{20M_\odot}\right)\left(\frac{\sigma}{75{\rm km/s}}\right)^{-2} \tag{3.14}$$

$$e = 1+\left(\frac{170\pi\eta}{3}\right)^{2/7}\left(\frac{\sigma}{c}\right)^{10/7}\left(\frac{r_{\rm p}}{r_{\rm p,max}}\right) \approx 1+1.57\times10^{-5}\eta^{2/7}\left(\frac{\sigma}{75{\rm km/s}}\right)^{10/7} \tag{3.15}$$

where M is the sum of masses, and we set $v_{\rm inf} = \sqrt{2}\sigma$. By assuming $r_{\rm p}/r_{\rm p,max} = 1/2$, typical pericenter distance for GR capture of encountering two $10M_\odot$ BHs is 2514km in Milky-Way-like galaxies (i.e., $\sigma = 75$km/s). Because the pericenter distance is nearly the same before and after capture, the semi-major axis and eccentricity of

the binary formed by GR capture are given by

$$a' = a\left[\left(\frac{r_{\rm p}}{r_{\rm p,max}}\right)^{-7/2} - 1\right]^{-1} \approx 0.153{\rm AU}\left(\frac{M}{20M_\odot}\right)\left(\frac{\sigma}{75{\rm km/s}}\right)^{-2}, \tag{3.16}$$

$$e' = 1 - \frac{a}{a'}(e-1) \approx 1 - 1.62\times10^{-4}\eta^{2/7}\left(\frac{\sigma}{75{\rm km/s}}\right)^{10/7}. \tag{3.17}$$

For an example of the velocity dispersion of $\sigma \sim 400$ km/s, the eccentricity of a typical binary formed by GR capture is $1 - e' \sim 10^{-3}$, which can show us the validity of the parabolic approximation again. From the distribution of semi-major axis and eccentricity, we can determine the distribution of merging time for such binaries. The merging time is given by (Peters 1964)

$$T_{\rm mer} = \frac{5}{64}\frac{c^5 a_0^4(1-e_0^2)^{7/2}}{G^3 m_1 m_2(m_1+m_2)}\left\{1 + \frac{73}{24}e_0^2 + \frac{37}{96}e_0^4\right\}^{-1}, \tag{3.18}$$

where a_0 and e_0 are the initial semi-major axis and eccentricity, respectively. Since the orbits of binaries in our consideration are nearly parabolic, the merging time has a strong dependence on the velocity dispersion as $T_{\rm mer} \approx a_0^4(1-e_0)^{7/2} \approx \sigma^{-3}$. Note that this merging time is not corrected for other PN terms (see §3.6.2 and Appendix A for other PN corrections). In Fig. 3.9, there are the distribution of semi-major axis, eccentricity and merging time of BH-BH binaries from equations (3.16), (3.17) and (3.18). As mentioned, we assume that the velocity of star follows one-dimensional normal distribution with σ= 75 km/s (i.e., the velocity dispersion for the Milky Way) and the pericenter distance $r_{\rm p}/r_{\rm p,max}$ follows uniform distribution. The peak position of each distribution is equivalent to the typical value in equations (3.16) and (3.17). For merging time, the mode is $\sim 10^6$ second. Although the distribution is quite wide, almost all binaries will merge within a Myr.

3.5.2 Event rates

We collect the parameters of all close encounter events in our simulations in order to investigate the GR capture and the compact binary coalescences. In the NBODY6 code, the regularization algorithm helps the calculation of very close orbits with high

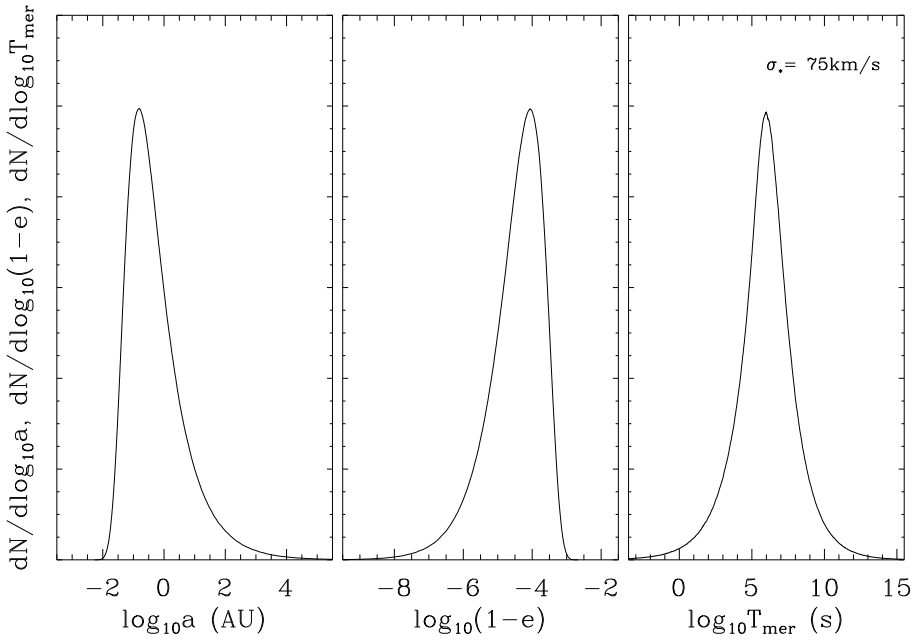

Figure 3.9 Distribution of semi-major axis (left panel), eccentricity (middle panel) and merging time (right panel) for $10M_{\odot}$ BH-BH binaries in the Milky-Way-like galaxies (i.e., $\sigma = 75$ km/s).

precision. If the separation or the time step of stars becomes smaller than certain criteria, the stars are separated from the main loop, and their motions are calculated with time smoothing. We turn on the KS regularization, the two-body regularization scheme, and extract the semi-major axis and the eccentricity of close encounters at the pericenter passage to avoid the effect of perturbation by nearby stars. Fig 3.10 shows the distribution of semi-major axis and the eccentricity of close hyperbolic encounters for the Model 4 after $T > t_{\rm MBH}$. Each filled dot represents each encounter and the dashed line shows the limit of KS regularization (i.e., $r_{\rm peri} \sim 10^{-4}$), so orbits lying above this line are not considered in our investigation. In order to determine whether a certain encounter results in a binary, we therefore need to convert our dimensionless results to physical quantities according to the equation (3.4). In Fig. 3.10, there are some orbits with rainbow colors. These colored orbits will become binaries when the overall velocity dispersion of stellar system is larger than that velocity (e.g., the orbit colored red at the left-end will become a binary when the velocity dispersion is ∼400 km/s.). By counting the number of capture events, we estimate the binary formation rates in our simulations.

For a single BH passing through stars with a speed v, the time scale for GR capture is

$$t_{\rm cap} \equiv (\Sigma_{\rm cap} n v)^{-1}, \tag{3.19}$$

where n is the number density of background stars. The binary formation rate between stars with different mass m_1 and m_2 in the shell with the range $[r,\, r + dr]$ can be expressed as

$$\frac{d\Gamma_{\rm cap}}{dr} = 4\pi r^2 n_1(r) n_2(r) \langle \Sigma_{\rm cap} v \rangle, \tag{3.20}$$

where $\langle \Sigma_{\rm cap} v \rangle$ is the velocity averaged value. Thus, assuming $v_\infty = \sqrt{2} v$ in equation (3.13) and replacing v by $\sigma(r)$, the velocity dispersion, we have

$$\frac{d\Gamma_{\rm cap}}{dr} \simeq 87 \frac{G^2 m_1 m_2 \eta^{-5/7}}{c^{10/7}} r^2 n_1(r) n_2(r) \sigma(r)^{-11/7}. \tag{3.21}$$

For the case of systems composed identical stars, $m = m_1 = m_2$, this equation becomes

$$\frac{d\Gamma_{\rm cap}}{dr} \simeq \frac{1}{2} 87 \frac{G^2 m^2 (1/4)^{-5/7}}{c^{10/7}} r^2 n^2(r) \sigma(r)^{-11/7}, \tag{3.22}$$

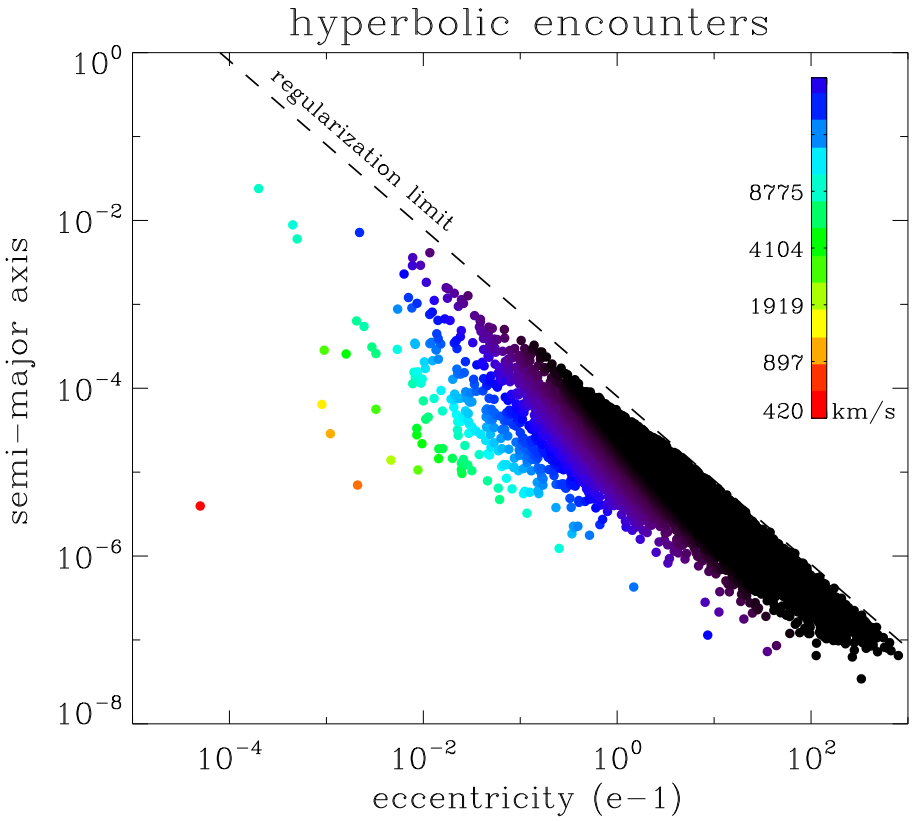

Figure 3.10 Distribution of semi-major axis and eccentricity of GR captured binaries for the Model 4. Different colors mean the velocity dispersion at the radius of influence in physical units as indicated by the color bar. These encountering stars become binaries by GR capture.

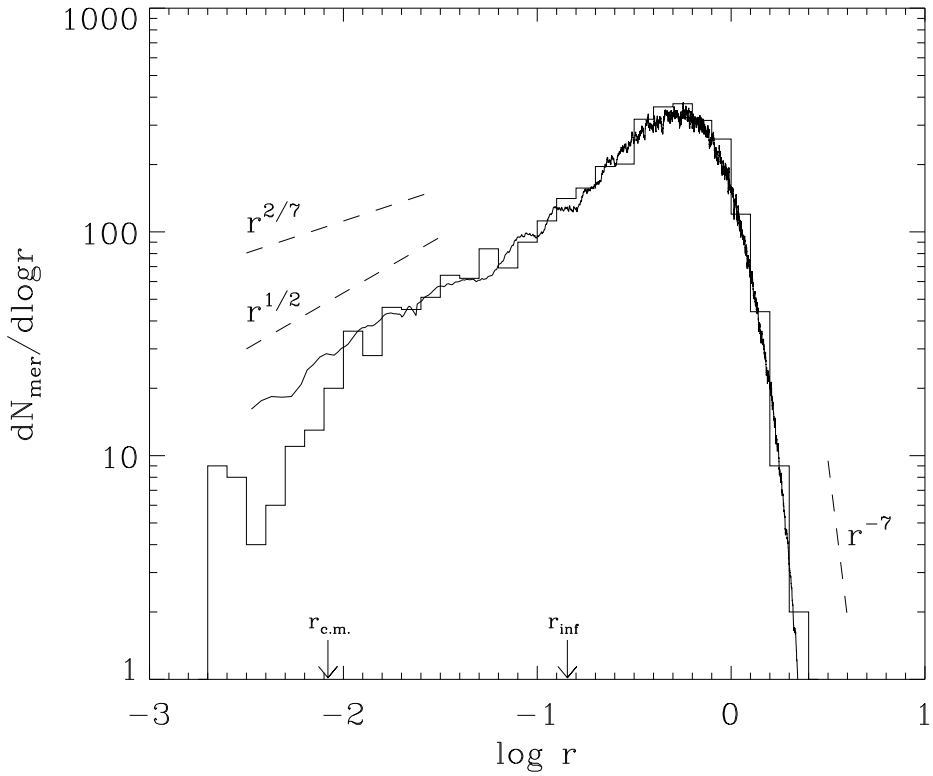

Figure 3.11 Radial distribution of GR binary capture rates. The noisy line is from the equation (3.22). This equation agrees well with events in the simulation except for the the inner region. From the theory, the slope of distribution inside the radius of influence is expected to be 2/7. However, it is $\sim 1/2$ because of discrepancy of profiles as shown in Figs. 3.3 and 3.4.

where the half is to avoid double counting and $\eta = 1/4$ for $m_1 = m_2$. Fig. 3.11 shows the radial distribution of cumulative capture events $dN_{\rm cap}/d\log r$ during $\Delta t = 1000 T_{\rm NBODY}$. Histogram is from N-body simulations of Model 4, and the noisy line is from the equation (3.22) (i.e., $dN_{\rm cap}/d\log r = r d\Gamma_{\rm cap}/dr \cdot \Delta t$) with the density and the velocity dispersion profiles from Figs. 3.3 and 3.4, respectively. In order to get large sample size, we set the unit of velocity to the half of the speed of light ($0.5c$). Although this velocity is unrealistically high, it is possible to guess what happens in realistic situations because there is no relativistic effect on the simulations. The simulation results and the formula show good agreement at the radius larger than $r_{\rm inf}$. However, at $r < r_{\rm inf}$, there is some discrepancy between them: the binary formation rate obtained with simulation is smaller than that with the equation (3.22). One possible reason is the time variation of density structure within the radius of influence as shown in Fig. 3.6. From the theoretical model of star distribution within the radius of influence (e.g., $\rho(r) \sim r^{-7/4}$ and $\sigma(r) \sim r^{-1/2}$), we obtain the slope of $dN_{\rm cap}/d\log r$ as

$$\frac{dN_{\rm cap}}{d\log r} \propto r^{2/7}. \tag{3.23}$$

However, the slopes inside $r_{\rm inf}$ in Fig. 3.11 are $\sim \frac{1}{2}$ rather than $\frac{2}{7}$ because the density cusp is not the same as the Bahcall-Wolf cusp (see Fig. 3.6). Incidentally, more than 80 per cent of events occur outside $r_{\rm inf}$, and the peak of $dN_{\rm cap}/d\log r$ is located at $r_{\rm half}$. The small discrepancy of analytical estimation at small radii thus does not affect the estimation of the total capture rates.

In order to obtain the overall merger rate for NC, we need to integrate the equation (3.22) over the volume. We can assume that the merger rate is equivalent to the capture rate because the merging time of BH-BH binary in our simulations is negligible compared to the cluster time scales as discussed before. It is difficult to estimate the merger rate because $n(r)$ and $\sigma(r)$ are not simple function of r. Instead, we can infer that the merger rate will be related to these variables:

$$\begin{aligned} \Gamma_{\rm mer} &\approx m^2 \cdot N \cdot \widetilde{n} \cdot \sigma_*^{-11/7} \\ &\approx M^{-1} \cdot \sigma_*^{31/7}, \end{aligned} \tag{3.24}$$

where $\widetilde{n}, \sigma_*$ and M are mean number density, the velocity dispersion of the system and total mass of the cluster, respectively. We see that the event rate is inversely proportional to the total mass of the cluster with rather steep dependence on the velocity dispersion of the cluster. To convert our results to physical units, it is necessary to determine the representing value of velocity dispersion of N-body simulations. We estimate the density-weighted velocity dispersion as similar to the observational estimation of velocity dispersion of bulge as (McConnell & Ma 2013)

$$\sigma_*^2 \equiv \frac{\int_{r_{\rm inf}}^{r_{\rm half}} 4\pi\sigma^2(r)\rho(r)r^2dr}{\int_{r_{\rm inf}}^{r_{\rm half}} 4\pi\rho(r)r^2dr}, \tag{3.25}$$

where $r_{\rm half}$ is half-mass radius. Note that the effective radius of bulge that is the upper limit of the integration for the systemic velocity dispersion in observations is much larger than the half-mass radius of NCs. According to recent observation for the calibration of velocity dispersion of nearby galaxies (Kang et al. 2013), however, the velocity dispersion does not change much with the aperture size. Thus, the velocity dispersion of NCs is enough to represent the velocity dispersion of bulges.

Figs. 3.12 and 3.13 show the merger rates as a function of the velocity dispersion in the physical unit. The mass ratio of MBH to the cluster is fixed at 0.2 for Fig. 3.12 ($\sigma_* \sim 0.79$) and 0.1 for Fig. 3.13 ($\sigma_* \sim 0.75$), respectively. Different symbols represent the different number of stars and dashed lines are from the time averaged result of numerical integration of the equation (3.24). Because of the limitations in the number of particles and the integration time, we only consider the unrealistic range of the velocity dispersion (1,000km/s $< \sigma_* <$ 20,000km/s). Nevertheless, because the results show very good scaling relation with the velocity dispersion and the total mass of the cluster, it is possible to extrapolate our results to realistic parameters for NC. As a result, the merger rate can be expressed by an equation with the mass of MBH and the velocity dispersion:

$$\Gamma_{\rm mer} \approx 2.06\times10^{-4}{\rm Myr}^{-1}\left(\frac{M_{\rm MBH}}{3.5\times10^6 M_\odot}\right)^{-1}\left(\frac{\sigma_*}{75{\rm km/s}}\right)^{31/7}, \text{ for } M_{\rm MBH}=0.2M_{\rm tot}, \tag{3.26}$$

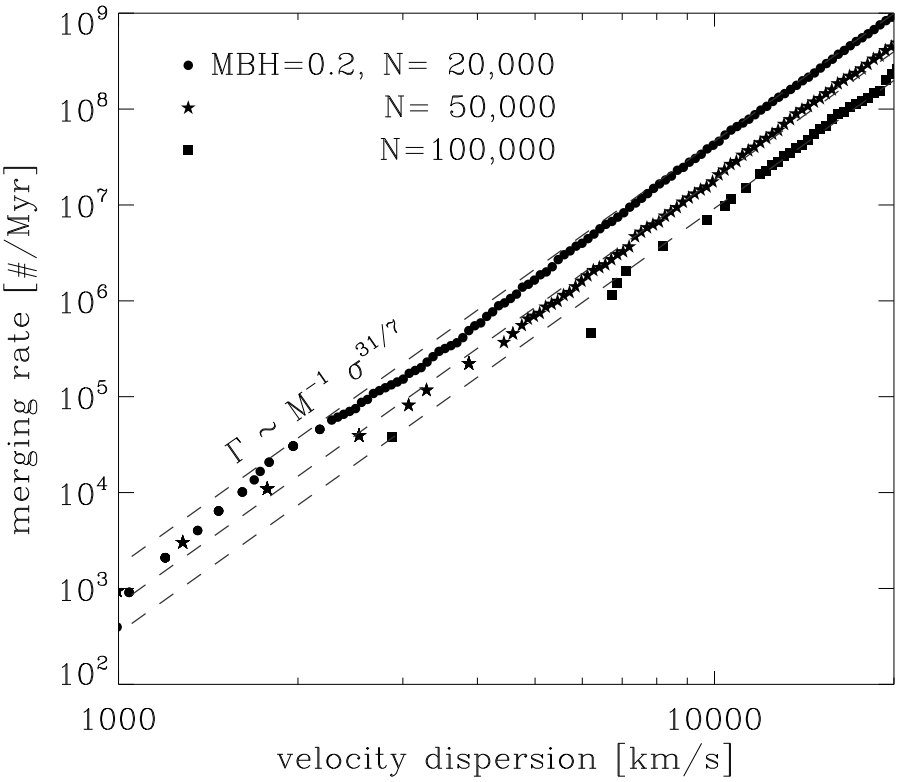

Figure 3.12 Merger rates as a function of velocity dispersion for models 2-4. The MBH mass is 20% of the total mass of the cluster. Filled symbols are from the number counts in simulations with different number of stars. Dashed lines show the equation (3.24) with the proportional constants obtained from the simulations. There are good correlations between merger rates and velocity dispersion.

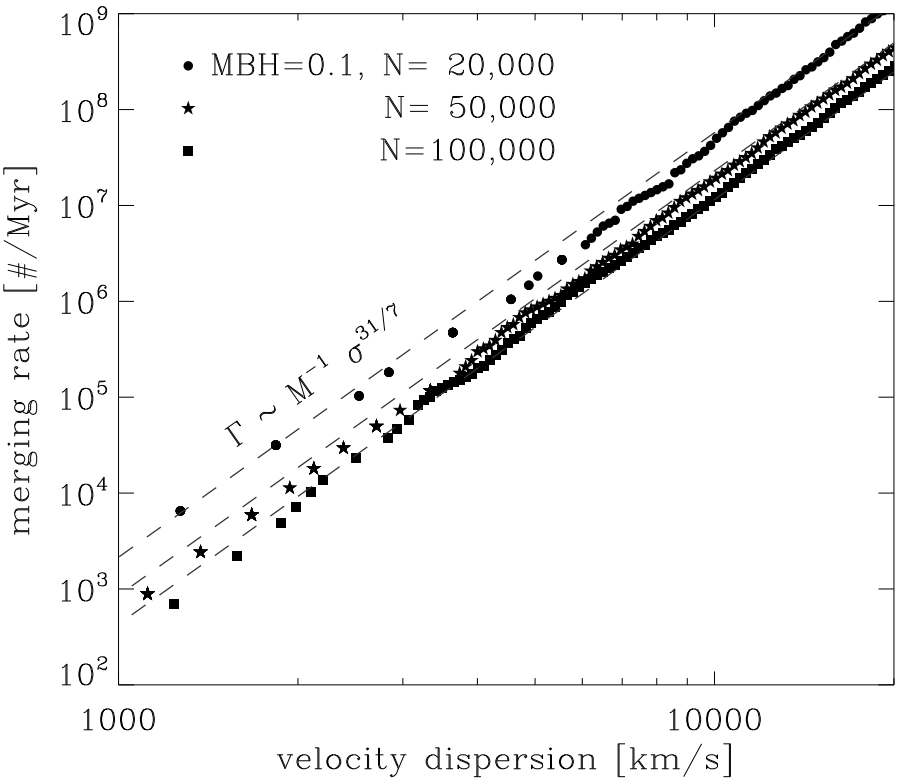

Figure 3.13 Merger rates as a function of velocity dispersion for models 5-7. The MBH mass is 10% of the total mass of the cluster.

$$\Gamma_{\rm mer} \approx 8.58\times10^{-5}{\rm Myr}^{-1}\left(\frac{M_{\rm MBH}}{3.5\times10^6 M_\odot}\right)^{-1}\left(\frac{\sigma_*}{75{\rm km/s}}\right)^{31/7}, \text{ for } M_{\rm MBH}=0.1M_{\rm tot}. \tag{3.27}$$

Thus, the merger rate is about $2.06\times10^{-10}{\rm yr}^{-1}$ for Milky-Way-like galaxies if we assume that the total mass of embedded star cluster is 5 times heavier than the MBH.

The time evolution of the merger rate for a Milky-Way-like galaxy is represented in Fig. 3.14, which is estimated from the Model 2 with $N = 20,000$ in order to see the long-term evolution. The time is scaled by the initial relaxation time at the radius of influence $\tau_{\rm ri,0}$ (Spitzer 1987) after growth of the MBH

$$\tau_{\rm ri,0} \equiv \frac{\langle v^2\rangle^{3/2}}{15.4G^2\bar{m}\bar{\rho}_{\rm inf}\ln\Lambda}, \tag{3.28}$$

where $\bar{m}$ and $\bar{\rho}_{\rm inf}$ are the mean mass (for equal-mass, $\bar{m} = M/N$) and the mean density inside the radius of influence, respectively. The noisy line is the merger rate from the numerical integration of the equation (3.22). For comparison, we plot the histogram showing the number of events counted in the simulation. They are selected with $\sigma_* = 10^4$ km/s for sufficient samples and rescaled to $\sigma_* = 75$ km/s range. The horizontal dashed line is the time-averaged merger rate in equation (3.26). Due to the expansion of the cluster, the merger rate decreases with time. These two estimates show good agreement, and therefore it is possible to surmise the merger rates from given density and velocity structures of stellar systems. The conversion of these merger rates to the detection rates for GW detectors will be presented in next section.

3.6 Discussion

3.6.1 GW detection rates

To determine the detection rate of GWs from BH-BH binary coalescences for GW detectors, it is necessary to calculate how many events occur per unit volume in the universe and horizon distance of GW detectors. In the previous section, we estimated the merger rates in NC as a function of the mass of MBH and the velocity dispersion.

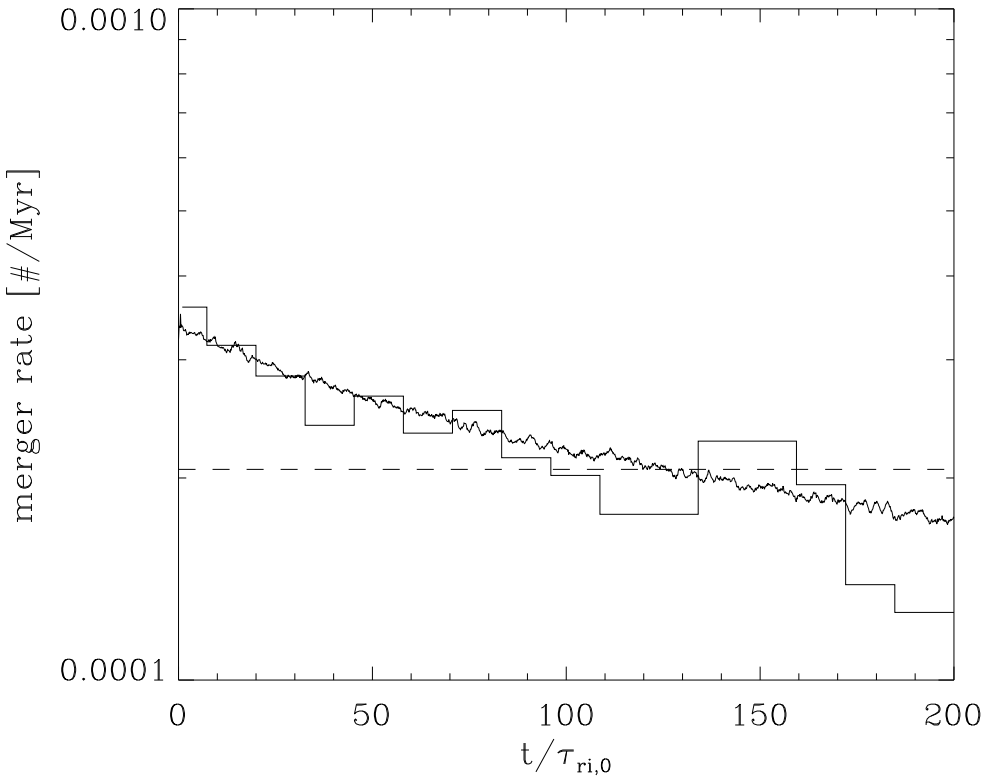

Figure 3.14 Time evolution of merger rate from Model 2 as a function of time at the radius of influence. The merger rate is scaled for a Milky-Way-like galaxy. Noisy line and histogram are from the integration of equation (3.22) and the number of events counted in the simulations, respectively. Due to the cluster expansion, the merger rate decreases with time. The dashed horizontal line represents the merger rate from equation (3.26).

It is well known that there is a good correlation between the mass of MBH and the velocity dispersion of surrounding stars (e.g., Tremaine et al. 2002)

$$M_{\rm MBH} \approx 1.3 \times 10^8 M_\odot (\sigma_*/200{\rm kms}^{-1})^4 \tag{3.29}$$

in a range of the mass of MBH $[10^6 M_\odot, 10^9 M_\odot]$. Later, Barth et al. (2005) confirmed that the relation is also valid for MBHs down to $10^5 M_\odot$. The merger rate for a NC, therefore, has a weak dependence on the mass of central MBH $\Gamma \sim M_{\rm MBH}^{3/28}$ (O'Leary et al. 2009), and the merger rates of (3.26) and (3.27) become

$$\Gamma_{\rm mer} \approx 3.33 \times 10^{-4} {\rm Myr}^{-1} \left(\frac{M_{\rm MBH}}{3.5 \times 10^6 M_\odot} \right)^{3/28}, \quad \text{for } M_{\rm MBH} = 0.2 M_{\rm tot}, \tag{3.30}$$

$$\Gamma_{\rm mer} \approx 1.39 \times 10^{-4} {\rm Myr}^{-1} \left(\frac{M_{\rm MBH}}{3.5 \times 10^6 M_\odot} \right)^{3/28}, \quad \text{for } M_{\rm MBH} = 0.1 M_{\rm tot}. \tag{3.31}$$

However, there are several factors that give rise to uncertainties in merger rates. From the equation (3.21), we can infer that the merger rate is proportional to the total mass of different mass components M_1 and M_2. As we mentioned before, however, we assumed that all stars are $10 M_\odot$ BHs. There exist other stellar objects such as MS stars, white dwarfs (WDs), NSs and BHs in real stellar systems. Hopman & Alexander (2006) have studied the effect of mass segregation of stars around a MBH and concluded that the number fraction of different stellar objects evolves from the initial state (i.e., $N_{\rm MS} : N_{\rm WD} : N_{\rm NS} : N_{\rm BH} = 1 : 0.1 : 0.01 : 10^{-3}$, for continuously star-forming populations; Alexander 2005) to $N_{\rm MS} : N_{\rm WD} : N_{\rm NS} : N_{\rm BH} = 1 : 0.09 : 0.012 : 0.06$ within 0.1 parsec for Milky-Way-like galaxies. If we set the mass of MS stars ($0.7 M_\odot$), WDs ($0.6 M_\odot$) and NSs ($1.4 M_\odot$), the mass fraction of BHs $\mathcal{M}_{\rm BH}$ is about 44 per cent of the total mass. When we simply assume that the merger rate of BHs in galactic nuclei can be expressed by the equations (3.26) and (3.27) with multiplication of $\mathcal{M}_{\rm BH}^2$, the merger rate in equation (3.26) is reduced to $3.95 \times 10^{-11} {\rm yr}^{-1}$, which is at least about 5 times smaller than the estimation of O'Leary et al. (2009). Of course, it is more complicated to correct for the mass function rather than our consideration because the mass fraction of BHs varies with the radius. Furthermore, the mass fraction in our consideration is adequate for innermost region although

the capture events happen most frequently around the half-mass radii as shown in Fig. 3.11. The mass fraction of BHs around the half-mass radius might be smaller than that from Hopman & Alexander (2006), and thus, our results could be an overestimation.

The dynamical evolution of NCs also affects the merger rates. The merger rate varies at most by a factor of 3 from $T = 0$ to $T = 200\tau_{\rm ri,0}$ as shown in Fig. 3.14. Merritt et al. (2007) have estimated the relaxation times $\tau_{\rm ri,0}$ for ACS Virgo samples of galaxies observed by Côté et al. (2004), and found the relation between the relaxation time and the central velocity dispersion. According to the relation, $\tau_{\rm ri,0}$ is less than a Hubble time with smaller velocity dispersion than 100 km/s, corresponding to $M_{\rm MBH} \sim 1.6 \times 10^7 M_\odot$. Therefore, the merger rates for NCs with smaller MBHs can be affected by the dynamical evolution. In addition, the relaxation time of galactic nuclei implies that most of NCs with larger MBHs do not contribute to the merger rates as much as those with smaller MBHs because the number fraction of BHs in relaxed nuclei is several tens of times lager than that of initial conditions due to the mass segregation (Hopman & Alexander 2006), and the merger rate weakly depends on the mass of central MBH (O'Leary et al. 2009). O'Leary et al. (2009) also noted that the variance of the number density of galactic nuclei can affect the merger rate. They have estimated the variance of the number density from the results of Merritt et al. (2007) and found that the merger rate is enlarged as much with the rescale factor $\xi \sim 10 - 100$.

In order to calculate the merger rate per unit cosmological volume, we convolve the merger rate per NC with the number density of MBHs in the universe (for more details, see §3.3.5 of O'Leary et al. 2009). Aller & Richstone (2002) determined the number density of MBHs from the luminosity function of galaxies as

$$\frac{dn_{\rm MBH}}{dM_{\rm MBH}} = c_\bullet \left(\frac{M_{\rm MBH}}{M_\bullet} \right)^{-\alpha} e^{-M_{\rm MBH}/M_\bullet} \tag{3.32}$$

with the best fitting parameters of $(c_\bullet, M_\bullet, \alpha) = (3.2 \times 10^{-11} M_\odot^{-1} {\rm Mpc}^{-3}, 1.3 \times 10^8 M_\odot, 1.25)$. The merger rate per volume, therefore, is obtained by integrating the rate over the SMBH mass distribution

$$\mathcal{R}_{\rm mer} = \int_{M_{\rm l}}^{M_{\rm u}} \Gamma_{\rm mer}(M_{\rm MBH}) \frac{dn_{\rm MBH}}{dM_{\rm MBH}} dM_{\rm MBH}, \tag{3.33}$$

where $M_{\rm u}$ and $M_{\rm l}$ are the upper and lower limits for integration, and $\Gamma_{\rm m,gal}$ is the merger rate per galaxy as a function of the mass of MBH. The upper limit can be fixed to $M_{\rm MBH} \sim 10^7 M_\odot$ by the time scale requirement as discussed above. However, we still do not have the exact lower limit of the MBH mass, which is currently about $10^5 M_\odot$ from the observation of Barth et al. (2005). With the uncertainty of the lower limit of the MBH mass from $10^3 M_\odot$ to $10^5 M_\odot$, the equation (3.33) gives us the merger rate density

$$\mathcal{R}_{\rm mer} \approx (2-5)\Gamma_{\rm mer,MW}\xi_{30}{\rm Mpc}^{-3}, \tag{3.34}$$

where $\Gamma_{\rm mer,MW}$ is the merger rate for a Milky-Way-like galaxy, and ξ_{30} is the rescale factor for the variance of the number density of stars normalized by 30 (i.e., $1/3 \lesssim \xi_{30} \lesssim 3$; O'Leary et al. 2009).

Now, we can estimate the detection rate of BH-BH binary coalescences by next generation GW detectors. By assuming that the merger events occur uniformly in the universe, the detection rate only depends on the size of cosmological volume which we can cover and can be expressed by (O'Leary et al. 2006; Belczynski et al. 2007; Downing et al. 2011; Bae et al. 2013)

$$\mathcal{R}_{\rm det} = \mathcal{R}_{\rm mer} \int \frac{4\pi r(z)^2}{1+z}\frac{dr}{dz}dz, \tag{3.35}$$

where z is the cosmological redshift, and the factor of $(1+z)^{-1}$ represents the cosmological time dilation. For existing GW detectors, the effect of redshift can be negligible because their coverage is not too far (i.e., the horizon distance $D_{\rm h}$ are 33 Mpc for NS-NS binaries and 161 Mpc for BH-BH binaries corresponding to $z \sim 0.01$ and 0.04 in standard ΛCDM cosmology, respectively; Abadie et al. 2010). However, for next generation GW detectors, the effect of redshift becomes important, especially for BH-BH binaries. The maximum horizon distance $D_{\rm h}$ can be obtained from signal-to-noise ratio (SNR) of GW signals (for more details, see §4.2 of O'Leary et al. 2009). Because the redshift affects both the mass of source and the frequency, SNR should be estimated from the waveforms carefully. Only few studies (Baker et al. 2007; O'Leary et al. 2009; Reisswig et al. 2009) have estimated $D_{\rm h}$ for BH-BH binaries for given SNR.

Table 3.2 Detection rates of BH-BH binaries for advanced LIGO.

Models	$M_{\rm MBH}/M_{\rm cl}$	$\Gamma_{\rm mer,MW}$ ($\rm Myr^{-1}$)	$\mathcal{M}^a_{\rm BH}$	$D_{\rm h}$ (Mpc)	$\mathcal{R}^b_{\rm det,l}$ ($\rm yr^{-1}$)	$\mathcal{R}^c_{\rm det,re}$ ($\rm yr^{-1}$)	$\mathcal{R}^d_{\rm det,h}$ ($\rm yr^{-1}$)
1-4	0.2	3.33×10^{-4}	0.44	986^e	0.06	0.44	2.99
				$\sim1100^f$	0.09	0.64	4.32
				$\sim1900^g$	0.27	2.00	13.5
5-7	0.1	1.39×10^{-4}	0.44	986^e	0.02	0.19	1.25
				$\sim1100^f$	0.04	0.27	1.80
				$\sim1900^g$	0.11	0.83	5.62

[a]Mean mass fraction of BHs from Hopman & Alexander (2006).

[b,c,d]Low, realistic and high detection rates depending on uncertainties discussed in text.

[e]$D_{\rm h}$ with SNR 8 form Abadie et al. (2010) divided by 2.26, the correction factor for sky location and orientation of sources. The effect of redshift is not included.

[f]$D_{\rm h}$ with SNR 10 form Fig. 16 in Baker et al. (2007).

[g]$D_{\rm h}$ with SNR 8 form Fig. 3 in Reisswig et al. (2009).

Table 3.2 shows the detection rates expected for advanced LIGO. Because we mainly considered the equal-mass models for only BHs, the detection rates are corrected by the factor of $\mathcal{M}_{\rm BH}^2$. We estimated detection rates by using $D_{\rm h}$ from different studies (Baker et al. 2007; Reisswig et al. 2009; Abadie et al. 2010). All $D_{\rm h}$s are corrected for the orientation of sources. Note that $D_{\rm h}$ from Abadie et al. (2010) does not include the cosmological effect of the redshift. $D_{\rm h}$ from Reisswig et al. (2009) is for spinning BHs but independent of the spin of BHs for $10M_\odot$ BHs. We list three detection rates $\mathcal{R}_{\rm det,l}$, $\mathcal{R}_{\rm det,re}$ and $\mathcal{R}_{\rm det,h}$ considering uncertainties discussed above. Reasonably, the detection rates are ranged from 0.2-2 yr^{-1} depending on the maximum horizon distance. These estimates are significantly lower than those of O'Leary et al. (2009) (5-2000 yr^{-1}).

Our estimations have some limitations; (1) We ignore the initial mass function. This mass function may affect not only the evolution of systems by the relaxation between mass components but also the merger rates for BHs with different masses. (2) We need to consider various range of $M_{\rm MBH}/M_{\rm cl}$ (e.g., Graham & Spitler 2009, suggested that there is a rough relation between the mass of MBH and NC.) (3) The exact calculation for SNR is necessary in order to obtain more reasonable detection rates. These limitations would be considered in future works.

3.6.2 Black hole binary coalescence and waveform

Solving Einstein field equation exactly is very difficult and has only been done numerically. Fortunately, during inspiral phase of compact binary coalescences, the Einstein equation can be simplified with the PN expansion. When a compact binary is formed, the orbit decays with time due to the GR. The orbit-averaged change of the semi-major axis and the eccentricity by GR is first derived by Peters (1964) as

$$\left\langle \frac{da}{dt} \right\rangle = -\frac{64}{5}\frac{G^3 m_1 m_2 (m_1+m_2)}{c^5 a^3 (1-e^2)^{7/2}}\left(1+\frac{73}{24}e^2+\frac{37}{96}e^4\right) \tag{3.36}$$

$$\left\langle \frac{de}{dt} \right\rangle = -\frac{304}{15}e\frac{G^3 m_1 m_2 (m_1+m_2)}{c^5 a^4 (1-e^2)^{5/2}}\left(1+\frac{121}{304}e^2\right), \tag{3.37}$$

in the 2.5 PN order ($\sim 1/c^5$, the first order GR term). However, the orbital evolution is also affected by other PN order terms such as 1PN (relativistic precession), 1.5

PN (spin-orbit coupling), 2PN (spin-spin coupling, high order relativistic precession) and higher orders. With full consideration of PN terms up to 2.5 order, Berentzen et al. (2009) noted that the decay of the binary orbit is much faster than that with 2.5PN only. Although the effect of the spin is quite important for the motions and waveforms of BH-BH binary coalescences, we only consider non-spinning BHs and take 1, 2 and 2.5PN order terms in this study.

The equation of motion with PN correction up to 2.5PN order can be simply written in the center of mass frame as (Blanchet & Iyer 2003; Mora & Will 2004)

$$\mathbf{a} = \mathbf{a_n} + \mathbf{a_{pn}} = -\frac{Gm}{r^3}\mathbf{r} + \frac{Gm}{r^2}(A\frac{\mathbf{r}}{r} + B\mathbf{v}) \tag{3.38}$$

where A, B are PN coefficients depending on their masses, the relative position r and relative velocity $\mathbf{v}$ (see Appendix A, for more details). Many authors have incorporated the PN corrected force in direct N-body simulations with different PN orders (Lee 1993; Aarseth 2007; Berentzen et al. 2009; Brem et al. 2013). Similarly, we implemented the PN equation of motion to the KS regularization process in NBODY6 code. In the KS regularization process, a two-body motion is sometimes perturbed by other neighboring stars, and these perturbation should be corrected. Thus, we can consider the PN force as a perturbing force in the code by adding the PN force and its time derivative. We designed that the binary will merge when the separation is smaller than four Schwarzschild radii $4R_{\rm Sch} \equiv 4 \cdot 2G(m_1 + m_2)/c^2$ because the PN approximation is not valid in this regime any more.

For instance, Fig. 3.15 shows the time evolution of semi-major axis and eccentricity for a $10M_\odot$ BH-BH binary with PN approximation. The initial semi major axis and eccentricity are 10^{-4} AU and 0.9, respectively. The solid line represents the time integration of Peters formula, equations (3.36) and (3.37). There is a good agreement between the results of simulation with only 2.5 PN term (open circle) and integration of Peters formula. On the other hand, the merging time of simulation with all PN terms (filled circle) is significantly smaller than that of Peters formula as reported in Berentzen et al. (2009). In case of this binary, it takes less then a half hour for merging (i.e., $r_{12} \leq 4R_{\rm Sch}$).

In our simulations, most of pairs of close encounters have not been perturbed by other nearby stars. Thus, it is possible to separate the two-body motion with PN

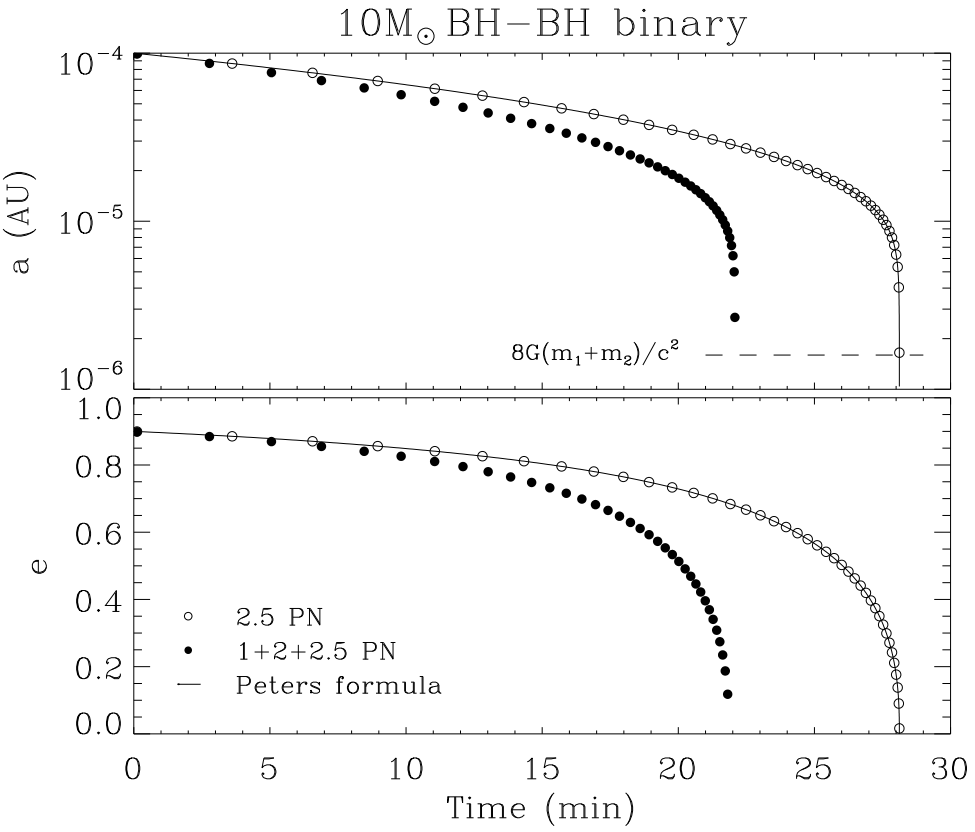

Figure 3.15 Time evolution of semi-major axis and eccentricity of a coalescing binary. Solid line is from the integration of Peters formula. Open and filled circles are the results of simulations with 2.5 PN correction only and full PN correction, respectively. The simulation with 2.5 PN correction only agrees well with Peters formula while that with full PN correction significantly festinates compared to Peters formula.

correction from the main loop of simulations. We, here, use a TOY[1] code only for a KS two-body motion written by S. J. Aarseth for convenience of exploration of the evolution of merging binaries. The PN implementation mentioned earlier is also adopted in the TOY code. For given semi-major axis and eccentricity, we simulate the orbital evolution of binaries. Fig. 3.16 shows the merging time of typical BH-BH binaries in equations (3.16) and (3.17) with different velocity dispersion of systems. The merging time is estimated by two-body simulations with all PN corrections. A star symbol is showing the result of a galactic nucleus in Milky-Way-like galaxy. In all cases, the merging times are less than a year. Binaries formed by GR capture, therefore, will merge immediately.

The GW waveforms of coalescing binaries have already been studied by many authors (e.g., Lincoln & Will 1990; Kidder 1995). As the perturbation of flat-space metric, h^{ij} in can be expressed by (for more details, see equations 3.21 and 3.22 in Kidder 1995)

$$h^{ij} = \frac{2\mu}{D}\left[Q^{ij} + P^{0.5}Q^{ij} + P(Q^{ij} + Q^{ij}_{\rm SO}) + P^{1.5}(Q^{ij} + Q^{ij}_{\rm SO}) + P^2 Q^{ij}_{\rm SS} + \cdots\right]_{\rm TT}, \quad (3.39)$$

where μ is the reduced mass, D is the distance from the source to the detector, Q^{ij} is the time derivative of quadrupole moment tensor, P^n is the PN corrections with order of n, and SO, SS and TT denote spin-orbit coupling, spin-spin coupling and transverse-traceless gauge, respectively. Here $G = c = 1$ is used. Since we are interested in the aspects of GW rather than the exact waveforms, we take the leading order of h^{ij}

$$h^{ij} \approx \frac{4\mu}{D}\left[v^i v^j - \frac{m}{r} n^i n^j\right], \quad (3.40)$$

with

$$Q^{ij} = 2\left[v^i v^j - \frac{m}{r} n^i n^j\right], \quad (3.41)$$

where v^i and n^i are the relative velocity and the normal vector of the relative position, respectively. It is well known that GWs have two polarization + and $\times$ and waveforms are the linear combination of these two polarizations. If we assume that

[1] http://www.ast.cam.ac.uk/∼sverre/web/pages/nbody.htm

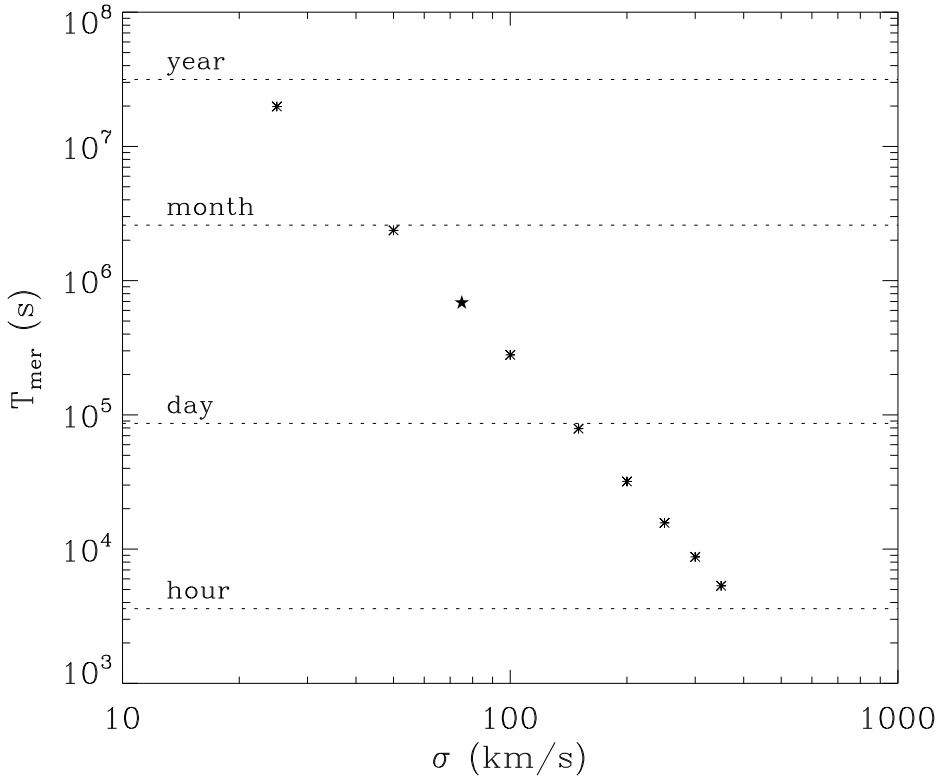

Figure 3.16 Merging time of typical $10M_{\odot}$ (see §3.5.1 for details) BH-BH binaries with different velocity dispersion of embedded star clusters. The merging times are obtained from two-body simulations with all PN corrections. The range of velocity dispersion is 50 to 400 km/s, which is correspond to the range of the mass of SMBH from $5 \times 10^5 M_{\odot}$ to $2 \times 10^9 M_{\odot}$ according to the $M_{\rm MBH} - \sigma_*$ relation from Tremaine et al. (2002). Star symbol represents the binary mering time in the Milky-Way-like galaxies. In all cases, the merging times are smaller than a year.

the orbital plane lies on the xy plane initially in the source coordinate, and the angle between the direction to the detector $\hat{\mathbf{N}}$ and the angular momentum $\hat{\mathbf{J}}$ is Θ, the polarizations h_+ and $h_\times$ are given by (Kidder 1995)

$$h_+ = \frac{1}{2}\Big(\cos^2\Theta h^{xx} - h^{yy} + \sin^2\Theta h^{zz} - \sin 2\Theta h^{xz} \Big), \tag{3.42}$$

$$h_\times = \cos\Theta h^{xy} - \sin\Theta h^{yz}. \tag{3.43}$$

Now we provide a waveform of a typical $10M_\odot$ BH-BH binary coalescence in a Milky-Way-like galaxy for an example. The semi-major axis and eccentricity after GR capture are 0.153 AU and 0.99989 from the equations (3.16) and (3.17), respectively. In Fig. 3.17, the relative motion of BHs on xy plane is shown. Due to the 1PN and 2PN terms, the position of perihelion is shifted counterclockwise. In addition, by emitting GWs, the orbit shrinks more and more with time. Fig. 3.18 shows the waveforms for this BH-BH binary coalescence. For simplicity, we assume that the axis of angular momentum is aligned with the direction to the detector (i.e., face-on view, $\Theta = 0$). In Fig. 3.18(a), the waveform of + polarization during whole evolution is presented. The merging time is about 8 days. Interestingly, the waveform is burst-like at the beginning, and it takes more than 2 days for the first burst after capture. The detailed waveforms h_+ and $h_\times$ at this moment are shown in 3.18(c) and (d). These waveforms are similar to those of eccentric orbits in Abramovici et al. (1992). Fig. 3.18(b), (e) and (f) show the waveform in the last minute, the detailed view of h_+ and $h_\times$ a half minute before merging, respectively. In this stage, the orbit is much circularized compared to the beginning, and the orbital frequency is about 10 Hz. At the moment of coalescence, the orbital frequency becomes few hundreds Hz which is the detectable frequency by ground-base GW detectors.

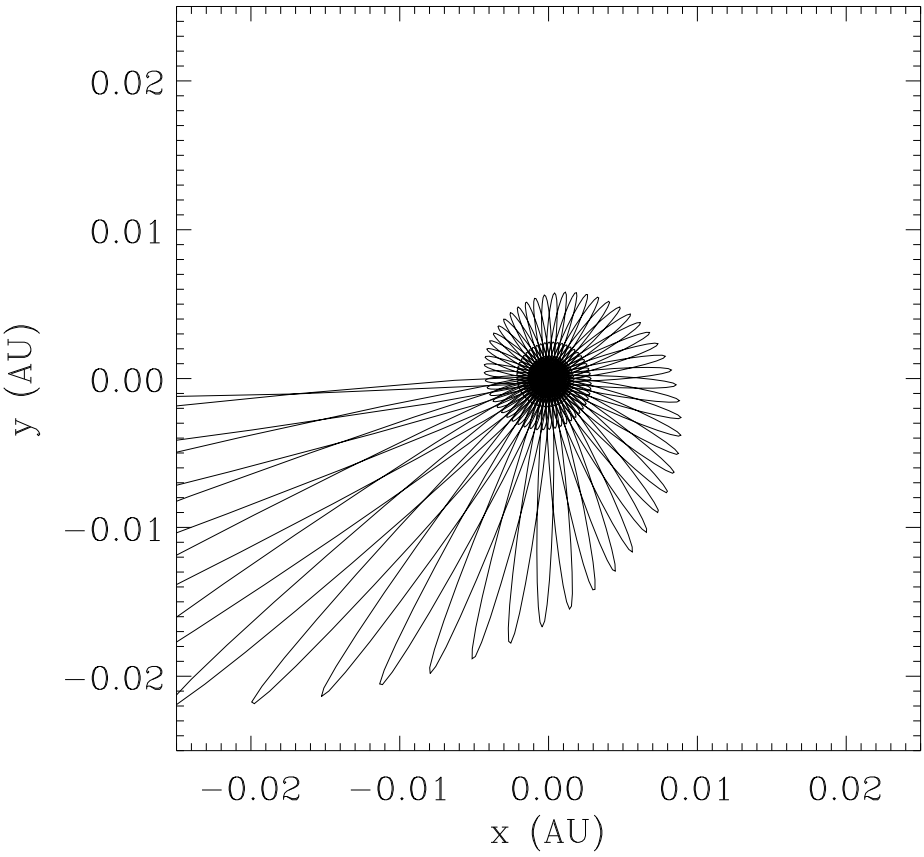

Figure 3.17 Relative orbital motion of a BH-BH binary with the initial semi-major axis 0.153 AU and eccentricity 0.99989, as a representative of typical BH-BH binaries in Milky-Way-like galaxies. The orbits are very eccentric at the beginning. The perihelion is shifted counterclockwise due to the 1PN and 2PN terms, and the orbit shrinks with time due to the GW emission.

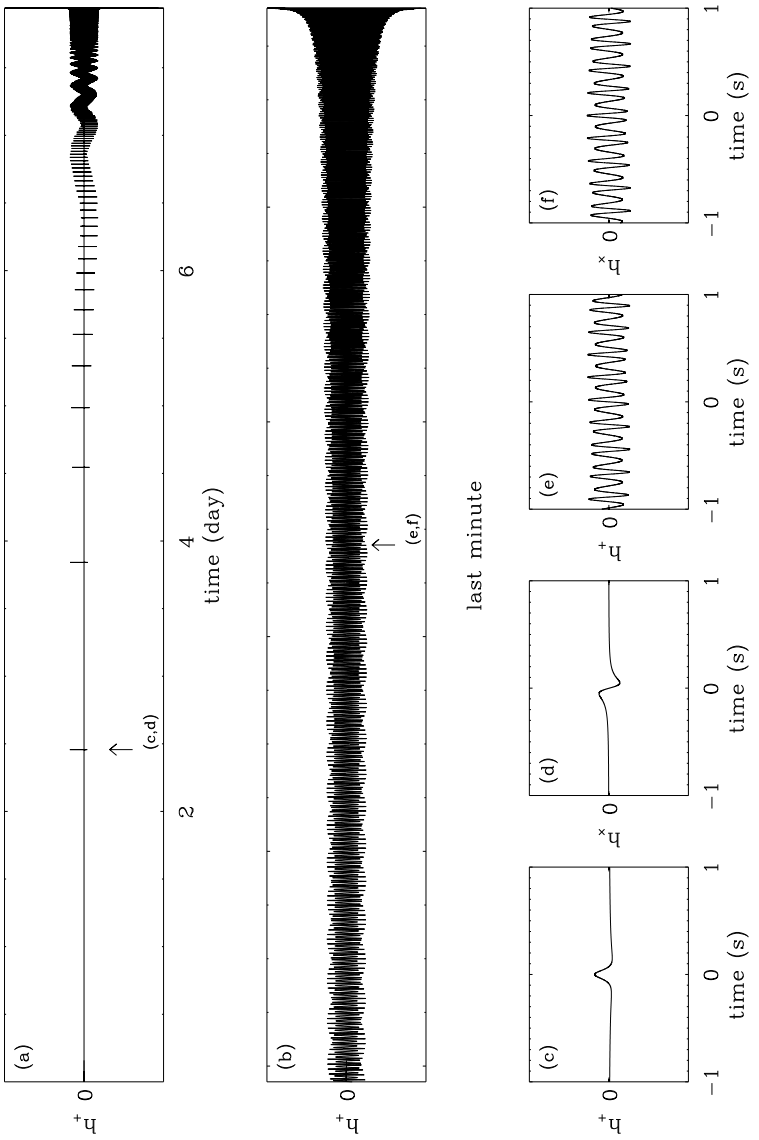

Figure 3.18 Waveform of BH-BH binary coalescence for the same binary in Fig 3.17. (a) h_+ for whole stage. The merging time is ∼8 days. The waveform is like a burst, initially. (b) h_+ for last minute. The waveform is much sinusoidal at this time. (c,d) h_+ and $h_\times$ for the first burst as marked in (a). They are similar to those of eccentric binaries in Abramovici et al. (1992). (e,f) h_+ and $h_\times$ at a half minute before coalescence as marked in (b). At this time, the frequency is $\sim$ 10 Hz.

Chapter 4

Summary and Conclusion

This thesis focuses on understanding of the dynamical evolution of the stellar systems under specific conditions and assumptions. I have investigated two different astrophysical applications by using Aarseth's type direct N-body simulations and with high performance hardwares such as GRAPE and GPU;

Dynamical evolution of rotating star clusters with two-component models

In Chapter 2, I have performed numerical simulations of rotating stellar system with two mass components using NBODY4 and mFOPAX codes. By considering various mass spectra, I confirmed that both the initial rotation and the mass spectrum accelerate the evolution of the stellar system, as presented previous studies (Einsel & Spurzem 1999; Kim et al. 2002, 2004, 2008). However, I found that the initial rotation does not affect the evolution before the core collapse when the individual mass ratio m_2/m_1 is large enough. The mass evaporation rate is closely related to the acceleration of the evolution and increases with m_2/m_1.

According to the instability criteria from Ostriker & Peebles (1973), I classified the models to slowly rotating models (i.e., $T_{\rm rot}/|W| < 0.14$) and rapidly rotating models (i.e., $T_{\rm rot}/|W| > 0.14$). By comparing the results of different approaches, N-body and FP simulations, I confirmed that two approaches agree well with small differences on the time scales for the slowly rotating models. On the other hand, for rapidly rotating models, there are significant discrepancies between N-body and FP

results. From the investigation of shape of systems, I revealed that the bar instability happens at the beginning for rapidly rotating models in N-body simulations. This bar instability induces unexpected phenomena like the rapid loss of mass, energy and angular momentum. In addition, the bar instability hinders the two-body relaxation process, so the dynamical evolution of rapidly rotating systems is delayed as compared with FP results. I therefore concluded that the 2 dimensional FP approach is not valid for rapidly rotating cases because 2 dimensional FP approaches are unable to treat non-axisymmetric models.

As the result of two-body interactions, low and high mass stars exchange their kinetic energies and happen to have similar kinetic energies. I confirmed that our models agree well with the equipartition instability criteria (Spitzer 1969; Watters et al. 2000) for slowly rotating models. When the mass ratio becomes larger, it is hard to reach the complete equipartition state. Moreover, the equipartiton process is more disturbed for rapidly rotating models which suffer the bar instability. I also observed the exchange of angular momentum between low and high mass stars by investigating escapers and defined the angular momentum exchange rate $\xi_{\rm exc}$. $\xi_{\rm exc}$ increases when the initial rotation increases. However, the amount of transferred angular momentum from high mass stars to low mass stars decrease because clusters with rapid initial rotation survive rather shortly compared to those with low initial rotation.

Black hole binaries in galactic nuclei and gravitational wave sources

In Chapter 3, I have generated N-body realizations for nuclear star clusters (NCs) located at the center of galactic bulges and hosting a massive black hole (MBH). In our simulations, the surrounding bulge is considered as the external potential well which makes the velocity dispersion of the embedded star cluster isothermal since a deep potential well behaves like a heat bath (Yoon et al. 2011). The MBH, in the same manner, is also modelled as a point-mass potential but growing with time to ensure the adiabatic adjustment of the stellar system. Consequently, our N-body realizations have a stellar density cusp ($\rho \sim r^{-1.75}$; Bahcall & Wolf 1976) and Keplerian velocity dispersion within the radius of influence. In addition, the

overall velocity structure is similar to observations of the star cluster at the center of Milky Way (e.g., Schödel et al. 2009). Strictly speaking, however, these star clusters are not in equilibrium but expand continuously since the MBH can generate kinetic energies by the interaction with stars in the cusp. Moreover, due to the wandering of the MBH, the slopes of density and velocity dispersion profiles are slightly shallower than those of theoretical expectations.

This environment of NCs is a good laboratory for gravitational wave (GW) sources. In order to investigate GW event rates in NCs, I have collected the orbital information of close encounters (i.e., semi-major axis and eccentricity) in our N-body simulations. While most of binaries are disrupted by the strong tidal field from MBH, there can be many hyperbolic encounters of stellar mass black holes (BHs) whose pericentric distances are sufficiently small to radiate GWs efficiently due to the high density and velocity dispersion at the vicinity of the MBH and the high number fraction of BHs due to the mass segregation (Hopman & Alexander 2006; O'Leary et al. 2009). When the energy loss by gravitational radiation (GR) is greater than the orbital energy, two BHs make a binary and merge quickly because of the small separation and large eccentricity after capture. Thus, the capture event rate corresponds to the merger rate. The capture happens most frequently near the half mass radius rather than within the radius of influence. Thus, our investigation of GR capture event rates is still valid although our models can not precisely realize the cluster inside of the radius of influence. By counting the number of GR capture events, I have built scaling relations of merger rates for a NC as a function of the mass of the MBH and the velocity dispersion of the star cluster. As the result, the merger rate for a Milky-Way-like galaxy is $\sim 10^{-10}\mathrm{yr}^{-1}$ proportional to the mass ratio of MBH to the star cluster.

From the $M_{\mathrm{MBH}} - \sigma_*$ relation (e.g., Tremaine et al. 2002), the merger rate becomes a function of the mass of MBH only. By using realistic mass function of MBHs (e.g., Aller & Richstone 2002), I have determined the merger rate density per unit volume. Then, the detection rates can be expressed with the merger rate density and the size of cosmological volume covered by GW detectors if I simply assume the uniformness of merger events over cosmic time and volume. I have obtained the

expected detection rates $0.2-2\mathrm{yr}^{-1}$ for advanced LIGO depending on the maximum horizon distances from different studies (Baker et al. 2007; O'Leary et al. 2009; Reisswig et al. 2009) and the mass ratio of MBH to the star cluster 0.1 and 0.2. This estimate is remarkably smaller than that of O'Leary et al. (2009) who suggested the detection rate of $\sim 10-1000\mathrm{yr}^{-1}$ of BH-BH binary coalescences in galactic nuclei for advanced LIGO. There are several factors giving uncertainties in our estimation: the dynamical evolution of the cluster (by a factor of $2\sim3$), the variance of number density of stars (by a factor of $\sim$10) and the mass range of MBH (by a factor of $2\sim3$). However, this study still have some limitations; (1) It is necessary to consider realistic mass function for BHs instead of assuming the mean mass fraction of BHs. (2) There is a relation between the mass of MBHs and the NCs (Graham & Spitler 2009). However, I fixed the mass ratio of MBH to the star cluster to 0.1 and 0.2. (3) In order to determine the maximum horizon distance for BH-BH binary mergers, the precise signal-to-noise ratio calculation is needed.

I have investigated the statistics of coalescing BH-BH binaries and found that the typical semi-major axis and eccentricity of these binaries are related to the velocity dispersion of the system. I also have implemented the post-Newtonian (PN) approximation on the two body motions up to 2.5 PN orders. With a given set of semi-major axis and eccentricity, I calculated the two-body motion under the PN approximation and the waveform of GW emission. The merging time is about a few hours for a typical BH-BH binaries in a Milky-Way-like galaxy. I also found that the orbital frequency becomes $\sim$100 Hz at the moment of coalescence, which is detectable by the ground-base GW detectors.

Bibliography

Aarseth, S. J. 1963, MNRAS, 126, 223

Aarseth, S. J. 1999, PASP, 111, 1333

Aarseth, S. J. 2007, MNRAS, 378, 285

Aarseth, S. J. 2010, Gravitational N-Body Simulations, by Sverre J. Aarseth, Cambridge, UK: Cambridge University Press, 2010,

Aarseth, S. J., Henon, M., & Wielen, R. 1974, A&A, 37, 183

Abadie, J., Abbott, B. P., Abbott, R., et al. 2010, Classical and Quantum Gravity, 27, 173001

Abramovici, A., Althouse, W. E., Drever, R. W. P., et al. 1992, Science, 256, 325

Ahmad, A., & Cohen, L. 1973, Journal of Computational Physics, 12, 389

Alexander, T. 2005, Phys. Rep., 419, 65

Alexander, T., & Hopman, C. 2009, ApJ, 697, 1861

Aller, M. C., & Richstone, D. 2002, AJ, 124, 3035

Ambartsumian, V. A. 1934, Mitteilungen der Nikolai-Hauptsternwarte zu Pulkowo, 13, 1

Ananda, K. N., Clarkson, C., & Wands, D. 2007, Phys. Rev. D, 75, 123518

Andersson, N., Ferrari, V., Jones, D. I., et al. 2011, General Relativity and Gravitation, 43, 409

Antonini, F., & Perets, H. B. 2012, ApJ, 757, 27

Ardi, E., Baumgardt, H., & Mineshige, S. 2008, ApJ, 682, 1195

Bae, Y., Lee, H. M., Kim, C. 2013, in preparation

Bahcall, J. N., & Wolf, R. A. 1976, ApJ, 209, 214

Baker, J. G., McWilliams, S. T., van Meter, J. R., et al. 2007, Phys. Rev. D, 75, 124024

Balcells, M., Graham, A. W., Domínguez-Palmero, L., & Peletier, R. F. 2003, ApJ, 582, L79

Barth, A. J., Greene, J. E., & Ho, L. C. 2005, ApJ, 619, L151

Baumgardt, H. 2001, MNRAS, 325, 1323

Baumgardt, H., Makino, J., & Ebisuzaki, T. 2004a, ApJ, 613, 1133

Baumgardt, H., Makino, J., & Ebisuzaki, T. 2004b, ApJ, 613, 1143

Belczynski, K., Taam, R. E., Kalogera, V., Rasio, F. A., & Bulik, T. 2007, ApJ, 662, 504

Berentzen, I., Preto, M., Berczik, P., Merritt, D., & Spurzem, R. 2009, ApJ, 695, 455

Binney, J., & Tremaine, S. 2008, Galactic Dynamics: Second Edition, by James Binney and Scott Tremaine. ISBN 978-0-691-13026-2 (HB). Published by Princeton University Press, Princeton, NJ USA, 2008.,

Blanchet, L., & Iyer, B. R. 2003, Classical and Quantum Gravity, 20, 755

Böker, T., Laine, S., van der Marel, R. P., et al. 2002, AJ, 123, 1389

Böker, T., Sarzi, M., McLaughlin, D. E., et al. 2004, AJ, 127, 105

Brem, P., Amaro-Seoane, P., & Spurzem, R. 2013, arXiv:1302.3135

Carollo, C. M., Stiavelli, M., de Zeeuw, P. T., & Mack, J. 1997, AJ, 114, 2366

Chen, C. W., & Chen, W. P. 2010, ApJ, 721, 1790

Cohn, H. 1979, ApJ, 234, 1036

Cohn, H. 1980, ApJ, 242, 765

Côté, P., Blakeslee, J. P., Ferrarese, L., et al. 2004, ApJS, 153, 223

Côté, P., Piatek, S., Ferrarese, L., et al. 2006, ApJS, 165, 57

Dehnen, W. 1993, MNRAS, 265, 250

Downing, J. M. B., Benacquista, M. J., Giersz, M., & Spurzem, R. 2011, MNRAS, 416, 133

Dubinski, J., & Carlberg, R. G. 1991, ApJ, 378, 496

Einsel, C., & Spurzem, R. 1999, MNRAS, 302, 81

Einstein, A. 1916, Sitzungsberichte der Königlich Preußischen Akademie der Wissenschaften (Berlin), Seite 1111-1116., 1111

Ernst, A., Glaschke, P., Fiestas, J., Just, A., & Spurzem, R. 2007, MNRAS, 377, 465

Ferrarese, L., & Ford, H. 2005, Space Sci. Rev., 116, 523

Finn, L. S., & Chernoff, D. F. 1993, Phys. Rev. D, 47, 2198

Fukushige, T., & Heggie, D. C. 2000, MNRAS, 318, 753

Fukushige, T., Makino, J., & Kawai, A. 2005, PASJ, 57, 1009

Giersz, M., & Heggie, D. C. 1994a, MNRAS, 270, 298

Giersz, M., & Heggie, D. C. 1994b, MNRAS, 268, 257

Giersz, M., & Heggie, D. C. 1996, MNRAS, 279, 1037

Giersz, M., & Spurzem, R. 1994, MNRAS, 269, 241

Goodman, J. J. 1983, Ph.D. Thesis, Princeton University, NJ

Goodman, J., & Binney, J. 1984, MNRAS, 207, 511

Graham, A. W., & Spitler, L. R. 2009, MNRAS, 397, 2148

Hachisu, I. 1979, PASJ, 31, 523

Hachisu, I. 1982, PASJ, 34, 313

Hansen, R. O. 1972, Phys. Rev. D, 5, 1021

Heggie, D. C. 1975, MNRAS, 173, 729

Heggie, D., & Hut, P. 2003, The Gravitational Million-Body Problem: A Multidisciplinary Approach to Star Cluster Dynamics, by Douglas Heggie and Piet Hut. Cambridge University Press, 2003, 372 pp.,

Hénon, M. 1961, Annales d'Astrophysique, 24, 369

Hernquist, L. 1990, ApJ, 356, 359

Holley-Bockelmann, K., Mihos, J. C., Sigurdsson, S., Hernquist, L., & Norman, C. 2002, ApJ, 567, 817

Hopman, C., & Alexander, T. 2006, ApJ, 645, L133

Hopman, C., Freitag, M., & Larson, S. L. 2007, MNRAS, 378, 129

Hulse, R. A., & Taylor, J. H. 1974, ApJ, 191, L59

Hut, P. 1983, ApJ, 268, 342

Hut, P., & Bahcall, J. N. 1983, ApJ, 268, 319

Kalogera, V., Kim, C., Lorimer, D. R., et al. 2004, ApJ, 601, L179

Kang, W.-R., Woo, J.-H., Schulze, A., et al. 2013, ApJ, 767, 26

Kent, S. M. 1992, ApJ, 387, 181

Khalisi, E., Amaro-Seoane, P., & Spurzem, R. 2007, MNRAS, 374, 703

Kidder, L. E. 1995, Phys. Rev. D, 52, 821

Kim, E. 2003, Ph.D. Thesis, Seoul National University, Korea

Kim, E., Einsel, C., Lee, H. M., Spurzem, R., & Lee, M. G. 2002, MNRAS, 334, 310

Kim, E., Lee, H. M., & Spurzem, R. 2004, MNRAS, 351, 220

Kim, E., Yoon, I., Lee, H. M., & Spurzem, R. 2008, MNRAS, 383, 2

Kim, S. S., Lee, H. M., & Goodman, J. 1998, ApJ, 495, 786

Kontizas, E., Kontizas, M., Sedmak, G., & Smareglia, R. 1989, AJ, 98, 590

Kormendy, J., & Richstone, D. 1995, ARA&A, 33, 581

Kozai, Y. 1962, AJ, 67, 591

Kustaanheimo, P., & Stiefel, E. 1965, J. Reine Angwq. Math., 218, 204

Lee, H. M. 1987, ApJ, 319, 772

Lee, H. M. 1995, MNRAS, 272, 605

Lee, H. M., & Goodman, J. 1995, ApJ, 443, 109

Lee, H. M., & Ostriker, J. P. 1986, ApJ, 310, 176

Lee, H. M., & Ostriker, J. P. 1987, ApJ, 322, 123

Lee, M. H. 1993, ApJ, 418, 147

Lightman, A. P., & Fall, S. M. 1978, ApJ, 221, 567

Lin, D. N. C., & Tremaine, S. 1980, ApJ, 242, 789

Lincoln, C. W., & Will, C. M. 1990, Phys. Rev. D, 42, 1123

Lupton, R. H., & Gunn, J. E. 1987, AJ, 93, 1106

Lynden-Bell, D., & Wood, R. 1968, MNRAS, 138, 495

Makino, J. 1991, ApJ, 369, 200

Makino, J. 1991, PASJ, 43, 859

Makino, J., Taiji, M., Ebisuzaki, T., & Sugimoto, D. 1997, ApJ, 480, 432

McConnell, N. J., & Ma, C.-P. 2013, ApJ, 764, 184

Merritt, D., Alexander, T., Mikkola, S., & Will, C. M. 2011, Phys. Rev. D, 84, 044024

Merritt, D., Mikkola, S., & Szell, A. 2007, ApJ, 671, 53

Meylan, G., & Heggie, D. C. 1997, A&A Rev., 8, 1

Meylan, G., & Mayor, M. 1986, A&A, 166, 122

Mikkola, S., & Aarseth, S. J. 1990, Celestial Mechanics and Dynamical Astronomy, 47, 375

Mikkola, S., & Merritt, D. 2006, MNRAS, 372, 219

Mora, T., & Will, C. M. 2004, Phys. Rev. D, 69, 104021

Mueller, E., & Janka, H.-T. 1997, A&A, 317, 140

Nitadori, K., & Aarseth, S. J. 2012, MNRAS, 424, 545

O'Leary, R. M., Kocsis, B., & Loeb, A. 2009, MNRAS, 395, 2127

O'Leary, R. M., O'Shaughnessy, R., & Rasio, F. A. 2007, Phys. Rev. D, 76, 061504

O'Leary, R. M., Rasio, F. A., Fregeau, J. M., Ivanova, N., & O'Shaughnessy, R. 2006, ApJ, 637, 937

O'Shaughnessy, R., Kim, C., Fragos, T., Kalogera, V., & Belczynski, K. 2005, ApJ, 633, 1076

Ostriker, J. P., & Peebles, P. J. E. 1973, ApJ, 186, 467

Peters, P. C. 1964, Physical Review, 136, 1224

Peters, P. C., & Mathews, J. 1963, Physical Review, 131, 435

Portegies Zwart, S. F., & McMillan, S. L. W. 2000, ApJ, 528, L17

Preto, M., & Amaro-Seoane, P. 2010, ApJ, 708, L42

Quinlan, G. D., & Shapiro, S. L. 1987, ApJ, 321, 199

Quinlan, G. D., & Shapiro, S. L. 1989, ApJ, 343, 725

Quinlan, G. D., Hernquist, L., & Sigurdsson, S. 1995, ApJ, 440, 554

Reisswig, C., Husa, S., Rezzolla, L., et al. 2009, Phys. Rev. D, 80, 124026

Schödel, R., Eckart, A., Alexander, T., et al. 2007, A&A, 469, 125

Schödel, R., Merritt, D., & Eckart, A. 2009, A&A, 502, 91

Sellwood, J. A. 1981, A&A, 99, 362

Shapiro, S. L. 1977, ApJ, 217, 281

Sigurdsson, S., Hernquist, L., & Quinlan, G. D. 1995, ApJ, 446, 75

Sippel, A. C., Hurley, J. R., Madrid, J. P., & Harris, W. E. 2012, MNRAS, 427, 167

Spitzer, L., Jr. 1940, MNRAS, 100, 396

Spitzer, L., Jr. 1969, ApJ, 158, L139

Spitzer, L. 1987, Princeton, NJ, Princeton University Press, 1987, 191 p.,

Spitzer, L., Jr., & Hart, M. H. 1971, ApJ, 164, 399

Spurzem, R., 1999, Journal of Computational and Applied Mathematics, 109, 407

Spurzem, R., & Takahashi, K. 1995, MNRAS, 272, 772

Takahashi, K., & Lee, H. M. 2000, MNRAS, 316, 671

Takahashi, K., Lee, H. M., & Inagaki, S. 1997, MNRAS, 292, 331

Takahashi, K., & Portegies Zwart, S. F. 1998, ApJ, 503, L49

Tremaine, S., Gebhardt, K., Bender, R., et al. 2002, ApJ, 574, 740

Walcher, C. J., van der Marel, R. P., McLaughlin, D., et al. 2005, ApJ, 618, 237

Watters, W. A., Joshi, K. J., & Rasio, F. A. 2000, ApJ, 539, 331

Weber, J. 1960, Physical Review, 117, 306

Weisberg, J. M., & Taylor, J. H. 2005, Binary Radio Pulsars, 328, 25

White, R. E., & Shawl, S. J. 1987, ApJ, 317, 246

Yakunin, K. N., Marronetti, P., Mezzacappa, A., et al. 2010, Classical and Quantum Gravity, 27, 194005

Yoon, I., Lee, H. M., & Hong, J. 2011, MNRAS, 414, 2728

Young, P. 1980, ApJ, 242, 1232

Appendix A

Post Newtonian Equation of Motion in Center of Mass Frame

Here, we present the post Newtonian (PN) equation of motion of binary system in the center of mass frame up to 2.5 PN order by following Mora & Will (2004). Because we assume non-spinning BHs, we do not consider spin terms in this paper. For the beginning, we borrow notations from Mora & Will (2004) as

$$\begin{aligned} m &= m_1 + m_2, \\ \mathbf{v} &= \mathbf{v}_2 - \mathbf{v}_1, \\ \mathbf{r} &= \mathbf{r}_2 - \mathbf{r}_1, \\ \mathbf{n} &= \mathbf{r}/r, \\ \eta &= (m_1 m_2)/(m_1 + m_2)^2, \end{aligned} \tag{A.1}$$

where m_1 and m_2 are the mass of stars, $\mathbf{r}_1, \mathbf{r}_2, \mathbf{v}_1$ and $\mathbf{v}_2$ are the 3-dimensional positions and velocities, and η is the symmetric mass ratio. As mentioned in the text, the PN acceleration can be considered as a perturbation and added to the gravitational acceleration as

$$\mathbf{a} = \mathbf{a_n} + \mathbf{a_{pn}} = -\frac{m}{r^2}\mathbf{n} + \frac{m}{r^2}(A\mathbf{n} + B\mathbf{v}) \tag{A.2}$$

where A and B are the PN coefficients related to the relative position and velocity, respectively, where

$$A_1 = 2(2+\eta)\frac{m}{r} - (1+3\eta)v^2 + \frac{3}{2}\eta\dot{r}^2 \tag{A.3}$$

$$A_2 = -\frac{3}{4}(12+29\eta)\frac{m^2}{r^2} - \eta(3-4\eta)v^4 - \frac{15}{8}\eta(1-3\eta)\dot{r}^4 + \frac{1}{2}\eta(13-4\eta)\frac{m}{r}v^2 + (2+25\eta+2\eta^2)\frac{m}{r}\dot{r}^2 + \frac{3}{2}\eta(3-4\eta)v^2\dot{r}^2 \tag{A.4}$$

$$A_{5/2} = \frac{8}{5}\eta\frac{m}{r}\dot{r}\left(\frac{17}{3}\frac{m}{r} + 3v^2\right), \tag{A.5}$$

and

$$B_1 = 2(2-\eta)\dot{r} \tag{A.6}$$

$$B_2 = -\frac{1}{2}(4+41\eta+8\eta^2)\frac{m}{r}\dot{r} + \frac{1}{2}\eta(15+4\eta)v^2\dot{r} - \frac{3}{2}\eta(3+2\eta)\dot{r}^3 \tag{A.7}$$

$$B_{5/2} = -\frac{8}{5}\eta\frac{m}{r}\left(3\frac{m}{r} + v^2\right), \tag{A.8}$$

where $\dot{r}$ is the first time derivative of radial distance defined as $\dot{r} = \mathbf{r}\cdot\mathbf{v}/r$. Then the coefficients A and B are given by the summations of coefficients for different PN order divided by the speed of light c, A_i/c^{2i}. Note that the sign of B is opposite of that in Blanchet & Iyer (2003).

Since the NBODY code uses 4th-order Hermite integrator, we have to have the first time derivatives of accelerations as similar to the accelerations

$$\dot{\mathbf{a}} = \dot{\mathbf{a}}_\mathbf{n} + \dot{\mathbf{a}}_\mathbf{pn}. \tag{A.9}$$

The derivative of PN acceleration $\dot{\mathbf{a}}_\mathbf{pn}$ can be expressed as

$$\dot{\mathbf{a}}_\mathbf{pn} = -2\frac{m}{r^3}\dot{r}(A\mathbf{n} + B\mathbf{v}) + \frac{m}{r^2}(\dot{A}\mathbf{n} + \dot{B}\mathbf{v} + A(\mathbf{v}/r - \mathbf{n}\dot{r}/r) + B\mathbf{a}), \tag{A.10}$$

where $\dot{A}$ and $\dot{B}$ are the time derivatives of the coefficients A and B, which are the summations of

$$\dot{A}_1 = -2(2+\eta)\frac{m}{r^2}\dot{r} - 2(1+3\eta)\mathbf{v}\cdot\mathbf{a} + 3\eta\dot{r}\ddot{r} \tag{A.11}$$

$$\begin{aligned}\dot{A}_2 = {} & \frac{3}{2}(12+29\eta)\frac{m^2}{r^3}\dot{r} - 4\eta(3-4\eta)v^2\mathbf{v}\cdot\mathbf{a} - \frac{15}{2}\eta(1-3\eta)\dot{r}^3\ddot{r} \\ & + \frac{1}{2}\eta(13-4\eta)\frac{m}{r}\left(2\mathbf{v}\cdot\mathbf{a} - \frac{v^2\dot{r}}{r}\right) + (2+25\eta+2\eta^2)\frac{m}{r}\left(2\dot{r}\ddot{r} - \frac{\dot{r}^3}{r}\right) \\ & + 3\eta(3-4\eta)(\mathbf{v}\cdot\mathbf{a}\dot{r}^2 + v^2\dot{r}\ddot{r})\end{aligned} \tag{A.12}$$

$$\dot{A}_{5/2} = \frac{8}{5}\eta\frac{m}{r}\left(\ddot{r} - \frac{\dot{r}^2}{r}\right)\left(\frac{17}{3}\frac{m}{r} + 3v^2\right) + \frac{8}{5}\eta\frac{m}{r}\dot{r}\left(-\frac{17}{3}\frac{m}{r^2}\dot{r} + 6\mathbf{v}\cdot\mathbf{a}\right) \tag{A.13}$$

and

$$\dot{B}_1 = 2(2-\eta)\ddot{r} \tag{A.14}$$

$$\begin{aligned}\dot{B}_2 = {} & -\frac{1}{2}(4+41\eta+8\eta^2)\frac{m}{r}\left(\ddot{r} - \frac{\dot{r}^2}{r}\right) \\ & + \frac{1}{2}\eta(15+4\eta)(2\mathbf{v}\cdot\mathbf{a}\dot{r} + v^2\ddot{r}) - \frac{9}{2}\eta(3+2\eta)\dot{r}^2\ddot{r}\end{aligned} \tag{A.15}$$

$$\dot{B}_{5/2} = \frac{8}{5}\eta\frac{m}{r^2}\dot{r}\left(3\frac{m}{r} + v^2\right) - \frac{8}{5}\eta\frac{m}{r}\left(-3\frac{m}{r^2}\dot{r} + 2\mathbf{v}\cdot\mathbf{a}\right) \tag{A.16}$$

where $\ddot{r}$ is the second time derivative of the radial distance given by

$$\ddot{r} = (v^2 + \mathbf{r}\cdot\mathbf{a} - \dot{r}^2)/r. \tag{A.17}$$

요 약

이 연구는 항성계의 역학적인 진화를 살펴보기 위해 수행되었으며, 현재 계산 과학 분야에서 각광 받는 GRAPE와 GPU 등 특수한 하드웨어를 이용한 N-체 수치 실험 결과들을 보여준다. 본 논문은 두 개의 특수한 천체 물리학적 상황과 관련된 현상에 대해 다루고 있는데, 회전하는 구상 성단과 은하 중심부에서의 중력파 원천으로서의 블랙홀 쌍성이다.

모은하에 대해 조석적으로 제한되어 있고 초기 질량 함수를 갖는 성단의 회전에 따른 역학적 진화를 연구하기 위해 각기 다른 초기 회전을 갖는 성단에 대한 N-체 수치 실험을 수행하고 이를 2차원 포커-플랑크 (Fokker-Planck) 계산 결과와 비교하였다. 그 결과, 초기 질량 함수뿐만 아니라 초기 회전도 성단의 진화에 영향을 미침을 확인할 수 있었다. 무차원의 초기 회전 변수인 ω_0가 0.6보다 작게 정의된 느리게 회전하는 모형의 경우에는 N-체 수치 실험에서의 질량, 에너지 그리고 각운동량의 시간 변화 등이 포커-플랑크 계산 결과와 잘 일치함을 볼 수 있었다. 반면, 빠르게 회전하는 모형의 경우, 두 계산 방식의 초기 진화 양상이 확연한 차이를 보이는데 이것은 빠르게 회전하는 모형의 경우 N-체 수치 실험에서 바 (bar) 불안정 현상이 생겨나기 때문이다. 이때 N-체 수치실험에서의 성단의 모양은 2차원 포커-플랑크 계산에서 다룰 수가 없는 삼축 구조를 갖기 때문에 두 계산 방식 간 차이가 발생하는 것이다. 성단의 질량, 에너지 그리고 각운동량 등의 물리량들은 바 불안정 상태 동안 빠르게 감소하며 바 불안정 상태가 해소된 이후에는 성단이 다시 축대칭을 이루게 되고 그 이후의 진화는 포커-플랑크 계산에서 예상하는 것과 비슷한 형태로 진행하게 된다. 기본적으로 두 개의 질량 성분을 갖고 있는 모형을 사용하였기 때문에, 두 개의 질량 성분 사이에서 발생하는 이완 작용에 대해서도 조사할 수 있었다. 에너지 등분배 현상이 특정 조건 하에서 완전히 이루어지지 않는, 이른바 등분배 불안정 (Spitzer 1969) 현상과 각운동량이 무거운 별들에서 가벼운 별들로 전이 되는 각운동량 교환 현상 등을 확인할 수 있었다.

중력파의 직접적인 검출은 근 시일 내에 향상된 LIGO/Virgo에서 이루어질 것이라고 예측되어지고 있으며 블랙홀 쌍성의 충돌은 중성자 별 쌍성과 더불어 가장 검출 가능성이 있는 중력파 원천 중의 하나로 알려져 있다. 이러한 블랙홀 쌍성이 은하 중심의 밀집한 항성계에서 생성되고 진화하는 과정에 대해 연구하기 위해 N-체 수치 실험이 수행되었다. 핵 성단 (nuclear star clusters)은 은하 중심에 위치한

매우 밀집된 별들의 집단으로 거대 질량 블랙홀을 포함하고 있다고 알려져 있으며 벌지 (bulge)와 같은 은하 구성 요소들에 중력적으로 묶여 있다. 핵 성단에서는 질량 분리로 인해 블랙홀의 개수 밀도가 높고 별들의 속도 분산이 크기 때문에 중력파 포획에 의해 블랙홀 쌍성이 형성될 수 있다. 우리 은하와 비슷한 은하들의 전반적인 블랙홀 쌍성 생성률은 약 $10^{-10}\mathrm{yr}^{-1}$ 정도이며 이 생성률은 거대 질량 블랙홀의 질량에 따라 약하게 변화한다. 중력파에 의한 포획으로 생성된 쌍성들은 상대적으로 매우 작은 충돌 시간을 갖기 때문에 쌍성의 생성률은 곧 충돌 확률이 된다. 이렇게 얻어진 은하 당 충돌 확률을 거대 질량 블랙홀의 질량 함수와 같이 적분하게 되면 단위 부피 당 충돌 확률을 알 수 있고, 이를 다시 중력파 검출기가 검출할 수 있는 최대 검출 범위까지 적분하면 중력파 검출기의 검출 확률을 구할 수 있다. N-체 수치 실험으로부터 예상되어지는 중력파 검출 빈도는 1년에 0.2-2개이지만, 성단의 시간 진화, 별의 밀도의 차이, 거대 질량 블랙홀의 질량 범위 등 여러 요소들이 불확실성을 최대 100까지 증가 시킬 수 있다. 이와는 별개로, post-Newtonian 근사를 사용하여 충돌하는 블랙홀 쌍성의 궤적과 이에 따라 발생하는 중력파의 파형을 조사해 보았다. 일반적으로 우리 은하 환경에서 중력파 포획으로 생성되는 블랙홀 쌍성의 경우 충돌에 수 일이 소요되며 충돌 시 궤도 주파수는 약 100Hz가 된다. 그리고 이러한 중력파의 파형은 일반적인 원 궤도 쌍성의 파형과 상당한 차이를 보이는데 이는 중력파 포획에 의해 생성되는 쌍성은 충돌 직전까지 큰 궤도 이심률을 유지하기 때문이다.

주요어: 수치 계산, 항성 역학, 성단, 회전, 중력파

학 번: 2006-20484